UNIVERSITY OF LIVERPOOL

Search for a Standard Model Higgs Boson in the $ZH \to \nu\nu bb$ channel with the ATLAS detector

Thesis submitted in accordance with the requirements of
the University of Liverpool for the degree of Doctor in Philosophy
by

Matthew Jackson

August 2015

Abstract

Since its discovery a large effort has been made to improve analyses and make precision measurments of the properties of the Higgs Boson. At a mass of 125 GeV Higgs to $b\bar{b}$ is the dominant decay mode. However, large QCD backgrounds mean that the gluon-gluon fusion production mode is not directly accessible at the LHC. Instead an analysis of Higgs to $b\bar{b}$ can considered where the Higgs is produced in association with a Vector Boson (W/Z). This document outlines such an analysis perfomed on the ATLAS Run I 8 TeV data with focus on one particular channel where the Higgs is produces in association with a Z Boson which subsequently decays to a pair of neutrinos.

Acknowledgements

First I would like to thank all of the staff from the HEP department at the University of Liverpool, for their continued support and guidance over the last eight years whilst I have been a student there. In particular I would like to thank Barry King and Steve Maxfield who supervised my masters project and have continued to offer their support throughout my PhD. I would also like to thank my PhD supervisors Andrew Mehta and Joost Vossebeld. A special thank you is saved for Carl Gwilliam for his advice, guidance and patience over the years as well as providing me with his, sometimes brutally, honest opinions on my work; this thesis has certainly benifited from them.

I would also like to mention all of the students at the University of Liverpool who I have shared this experience with. Special thanks have to go to Allan and Adrian who spent time on LTA in Geneva with me, your friendship got me through a difficult year and gave me some fantastic memories.

Finally I would like to thank my wife Jessica who has continued to encorage and support me regardless of where in the world I was. You have given me the motivation and confidence to finish this thesis.

Contents

List of Figures

List of Tables

Chapter 1

Introduction

The Large Hadron Collider (LHC) was built to study fundamental particle physics at extremely high energies. The experiments built around the LHC have been, at the time of writing, collecting data for several years. This thesis presents two analyses undertaken with such data.

The first analysis presented in chapter 5 is a technical study looking at the efficiency of reconstructing b-jets within simulated data produced for the ATLAS detector, one of the experiments on the LHC. The analysis aims to help reduce the systematic uncertainties associated with the reconstruction of jets, particularly jets with high transverse momentum.

Chapter 6 then presents a search for the Standard Model Higgs boson; a fundamental boson which is the consequence of electroweak symmetry breaking introduced in the Standard Model to give masses to the other fundamental particles. The analysis probes one particular decay channel where the Higgs boson, which decays to a pair of b-quarks, is produced in association with another massive vector boson, identified through a leptonic decay.

Prior to presentation of the analyses details of the underlying theoretical motivation and experimental apparatus are given. Chapter 2 introduces the Standard Model of particle physics with a particular emphasis on the Higgs boson. Previous searches for the Higgs boson are also discussed here. Next, chapter 3 introduces the LHC and the ATLAS detector. Finally, chapter 4 details the reconstruction of the particles measured by the ATLAS detector.

Chapter 2

The Standard Model

The Standard Model (SM) of particle physics is a quantum field theory describing interactions between fundamental particles through the electromagnetic (EM), strong and weak forces. The theoretical framework of the SM does not describe gravity. Gravity is much weaker than the other forces; acting upon objects at the particle scale it is 10^{39} times weaker [1] than the next weakest force. Therefore even with the exclusion of gravity the SM has been extremely successful at predicting many physical results with high accuracy.

This chapter will discuss the framework of the SM and introduce the fundamental particles and forces which it predicts. Emphasis is placed on the Higgs boson, the focus of this thesis. A more complete description of the SM can be found in [2].

2.1 Forces and Particles of the Standard Model

Within the mathematical framework of the SM two different types of particles are allowed; fermions and bosons. Fermions are particles with half integer spin and form the constituents of matter. Bosons are particles with integer or zero spin and mediate forces between fermions. This section will introduce fermions and bosons and discuss the theory of the interactions between these fields. For reference a summary of SM particles can be seen in table 2.1.

2.1.1 Fermions

Fermions are further subdivided into two categories; leptons and quarks. Leptons interact only with the EM and weak forces, while quarks also interact with the strong

		I	II	III	Bosons
Fermions	Quarks	u	c	t	γ
		d	s	b	g
	Leptons	e	μ	τ	Z, $W^{\pm}$
		ν_e	ν_μ	ν_τ	H

TABLE 2.1: A summary of the particles of the Standard Model.

force. There are three generations (labeled in table 2.1 as I, II and III) of fermions in the SM. Each generation contains a pair of quarks, a lepton and its corresponding lepton neutrino.

2.1.1.1 Leptons

There are six observed leptons in the SM. Three charged leptons: the electron, e; muon, μ; and tau, τ; and their respective neutrally charged neutrinos: ν_e, ν_μ and ν_τ. By convention the charged leptons are said to be negatively charged. Oscillations between the different flavours of neutrino have been observed [3] proving that neutrinos have a non-zero mass. Table 2.2 outlines some properties of the leptons.

Flavour	Electric Charge	Mass (GeV)	Generation
e	-1	0.511×10^{-3}	I
ν_e	0	$<225 \times 10^{-9}$	
μ	-1	105.7×10^{-3}	II
ν_μ	0	$<0.19 \times 10^{-3}$	
τ	-1	1.777	III
ν_τ	0	$<18.2 \times 10^{-3}$	

TABLE 2.2: A summary of lepton properties. Neutrino masses have yet to be precisely measured, experimental results however have set an upper limit [4].

2.1.1.2 Quarks

There are six flavours of quarks. Each generation of fermions has one up type quark; u, c, or t and one down type quark; d, s or b. Quarks carry fractional charge with up type quarks carrying a charge of +2/3 and down type quarks carrying a charge of -1/3. A summary of their properties can be seen in table 2.3.

Quarks also carry colour charge. Colour charge is a property which plays the same role within the strong interaction as electric charge in electromagnetism. Every quark is characterised by one colour; red, green or blue. Individual quarks have not been observed, only bound "colourless" states consisting of either three quarks of different

Generation	Flavour	Electric Charge	Mass (GeV)
I	u	+2/3	$(1.5 - 3.3) \times 10^{-}3$
	d	-1/3	$(3.5 - 6.0) \times 10^{-}3$
II	c	+2/3	$1.27^{+0.07}_{-0.11}$
	s	-1/3	$104^{+26}_{-34} \times 10^{-}3$
III	t	+2/3	171.2 ± 2.1
	b	-1/3	$4.2^{+0.17}_{-0.07}$

TABLE 2.3: A summary of quark properties [4].

colour (baryons), such as the proton (uud), or a quark and anti-quark of the same colour (mesons), such as the π^+ ($u\bar{d}$), have been observed in nature.

2.1.2 Bosons

Each force has one or more boson associated to it. The massless photon, γ, mediates the EM force; the Z^0 and $W^{\pm}$ bosons mediate the weak force and eight massless gluons, g, mediate the strong force. Each of these bosons have a spin of 1 and are known as vector bosons. A summary of force mediating boson properties can be seen in table 2.4. As well as the vector bosons, the SM contains one spin 0 scalar boson known as the Higgs boson. The Higgs boson plays an important part in the SM and is the result of the Higgs Mechanism which provides massive vector bosons with mass. This thesis focuses on one analysis which contributed to its discovery.

	Interaction	Electric Charge	Mass (GeV)
g	Strong	0	0
γ	EM	0	0
Z^0	Weak	0	91.1876 ± 0.0021
$W^{\pm}$	Weak	± 1	80.398 ± 0.025
H	-	0	125.09 ± 0.24

TABLE 2.4: A summary of vector boson properties [4, 5].

2.1.3 Standard Model Particle Summary

In total there are 30 distinct elementary particles. There are 24 fermions; 6 quarks and 6 leptons, each fermion has a corresponding anti-particle which is identical aside from having opposite charge. There are 6 bosons; the massless gluon, the massless photon, the Higgs boson and three massive bosons, $W^{\pm}$ and Z^0. All of the particles have now been experimentally observed.

2.2 Quantum Field Theories

The SM uses a relativistic quantum field theory (QFT) to describe the interactions and dynamics of fundamental particles. In QFTs particle fields which permeate over all space are quantised. Excitations in these fields represent particles. The Lagrangian formulation is used to describe the dynamics of these particles and their interactions with each other. Dynamics of a system are governed by the symmetries respected by the chosen Lagrangian. The SM is invariant under local transformations of the $SU(3)_C \times SU(2)_L \times U(1)_Y$ gauge group resulting in the three fundamental forces; strong, weak and EM. Here C represents colour charge, L, left-handed weak isospin and Y hypercharge. Each of these forces are described within the SM by a gauge theory. Quantum chromodynamics (QCD) describes strong interactions between quarks and gluons. Quantum electrodynamics (QED) describes EM interactions and is described together with the weak interaction within the context of electroweak unification.

2.2.1 Electroweak Unification and the Higgs Mechanism

Unification of the EM and weak forces was first suggested by Glashow [6] and independently by Salam and Ward [7]. Electroweak interactions are mediated by photons, $W^{\pm}$ and Z bosons and are governed by $SU(2)_L \times U(1)_Y$ gauge symmetries. Such local gauge theories predict massless vector bosons; however, this prediction can not be correct as massive $W^{\pm}$ and Z bosons have been observed [8].

The masses of the $W^{\pm}$ and Z bosons are introduced into the SM via spontaneous symmetry breaking with the introduction of the Higgs Field. The Goldstone Theorem [9] can be applied to the spontaneous symmetry breaking of the SM. It tells us that in a generic continuous symmetry which is simultaneously broken (such as the SM) there must exist one massless scalar boson for each broken symmetry generator. These bosons are known as Goldstone bosons. In the case of the SM and the spontaneous symmetry breaking of the $SU(2)_L \times U(1)_Y$ gauge group four massless Goldstone Bosons are produced. Brout and Englert [10], Higgs [11, 12], and Kibble, Guralnik and Hagen [13] developed a theory, now known as the Higgs Mechanism, which showed how the massless Goldstone bosons can be absorbed by the longitudinal polarisation of the $W^{\pm}$ and Z bosons causing them to have mass.

The Higgs Field, ϕ, is a complex $SU(2)_L$ doublet constructed from two complex scalar fields, ϕ^+ and ϕ^0,

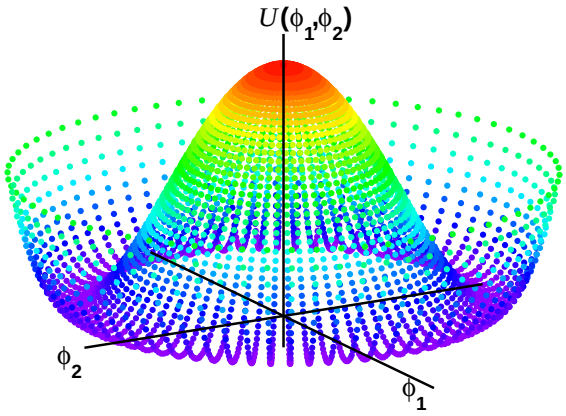

FIGURE 2.1: The 'Mexican hat' potential given in 2.3 where $\mu^2 < 0$ and $\lambda > 0$ [14]

$$\phi = \begin{pmatrix} \phi^+ \\ \phi^0 \end{pmatrix} = \frac{1}{\sqrt{2}} \begin{pmatrix} \phi_1 + i\phi_2 \\ \phi_3 + i\phi_4 \end{pmatrix}. \tag{2.1}$$

The Lagrangian describing the dynamics of the Higgs field is defined as

$$\mathcal{L}_{\mathrm{H}} = (D_\mu \phi)^\dagger (D^\mu \phi) - V(\phi) \tag{2.2}$$

containing a kinetic term and a symmetric potential, $V(\phi)$ with the form

$$V = \mu^2 \phi^\dagger \phi - \lambda (\phi^\dagger \phi)^2 \tag{2.3}$$

where μ and λ are both free parameters. In the case where $\mu^2 < 0$ and $\lambda > 0$ a 'Mexican hat' potential is produced with a non-zero minimum, see figure 2.1, allowing spontaneous symmetry breaking to occur. $\mathcal{L}_H$ is invariant under gauge transformations.

In order to leave the photon massless the vacuum expectation value (vev), ϕ_0, must be invariant under $U(1)_Q$ gauge transformations. The EM gauge symmetry is unbroken. The resulting vev has the form

$$\phi_0 = \sqrt{\frac{1}{2}} \begin{pmatrix} 0 \\ v \end{pmatrix} \text{ where } v = \sqrt{-\frac{\mu^2}{\lambda}}. \tag{2.4}$$

As $\mathcal{L}_H$ is invariant under local gauge transformations it can be transformed into a different gauge. Such a transformation can be made into a special gauge which minimised the number of scalar degrees of freedom. This is known as the unitary gauge in which the Higgs Field can be written as

$$\phi = \frac{1}{\sqrt{2}} \begin{pmatrix} 0 \\ H + v \end{pmatrix} \tag{2.5}$$

where H is the neutral Higgs scalar field. Expanding $\mathcal{L}_H$ around ϕ_0 results in mass terms for $W^{\pm}$ and Z bosons. For a more complete derivation see [15].

Fermions acquire mass through an additional $SU(2)_L \times U(1)_Y$ invariant Yukawa term added to the Lagrangian. An example of this can be shown for the electron where the Yukawa term is given as

$$\mathcal{L}_Y(e) = -G_e[\bar{\chi}_{\mathrm{L}}\phi e_{\mathrm{R}} + \bar{e}_{\mathrm{R}}\phi^{\dagger}\chi_{\mathrm{L}}] \tag{2.6}$$

where χ_{L} is a left handed doublet, e_{R} is a singlet and G_e is the Yukawa coupling. In the unitary gauge we have the Higgs Field given in equation 2.5, substituting this into $\mathcal{L}_Y(e)$ the electron mass and Higgs boson coupling can be identified. The couplings between the Higgs Boson and fermions is proportional to mass hence why $H \rightarrow b\bar{b}$ is an important signature for Higgs boson searches.

2.3 Searches for the Higgs Boson

Searches for the Higgs boson have followed its prediction. Although the Higgs mass is not predicted by the SM a limit of ∼1 TeV is set by theory [16]. Beyond this mass unitarity of certain scattering processes would be broken. Very early searches were able to put constraints on the mass of the Higgs boson [17, 18]. However they were unable to explore a wide mass range until the development of high energy particle colliders.

2.3.1 Higgs Searches Prior to the LHC

Searches for the Higgs boson using high powered particle colliders began at CERN with the Large Electron-Positron (LEP) Collider. LEP ran from 1989 to 2000, accelerating and colliding electrons and positrons at a centre of mass energy up to $\sqrt{s} = 209$ GeV. LEP measured observables of particles with which the Higgs interacts. Through these

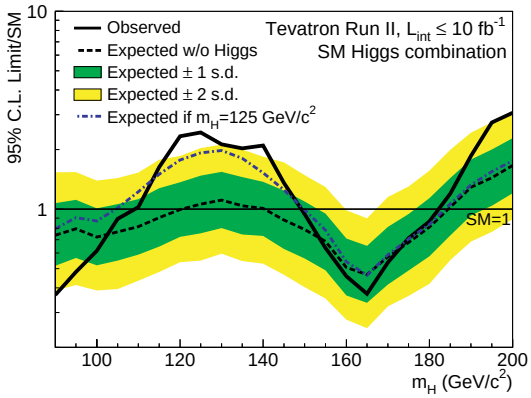

(a)

FIGURE 2.2: Exclusion limits from the Tevatron combination [21]. A global excess at 2.5σ is observed at $m_H \sim 120$ GeV.

precision electroweak measurements, combined with direct exclusion limits LEP was able to place a lower bound on the Higgs mass at a 95% confidence level of $m_H = 114.4$ GeV [19].

Following LEP, the Tevatron, a proton anti-proton collider at the Fermi National Accelerator Laboratory, was able to place further constraints on the Higgs mass. At the end of running in 2011, combined data from two experiments (CDF and D0) were able to exclude the SM Higgs boson in the mass ranges $100 \leq m_H \leq 108$ GeV and $147 \leq m_H \leq 180$ GeV at a 95% confidence level [20]. Furthermore a global excess at 2.5σ was observed at $m_H \sim 120$ GeV [21]. Figure 2.2 shows the exclusion limit for the Tevatron combination, the excess can be seen around $m_H \sim 120$. This result is of particular interest as the dominant decay channels analysed at the Tevatron are those used in the presented analysis.

2.3.2 Higgs at the LHC

Current Higgs searches at the LHC are based upon the full Run 1 dataset collected in 2011 and 2012 at $\sqrt{s} = 7$ TeV and $\sqrt{s} = 8$ TeV respectively, with a total integrated luminosity of approximately 25 fb^{-1}.

2.3.2.1 Higgs Production and Decay at the LHC

During collisions in the LHC the Higgs boson can be produced in several ways. Feynman diagrams for the four most probable Higgs production mechanisms can be seen in figure 2.3. The rate of each process depends on the centre of mass energy and the mass of

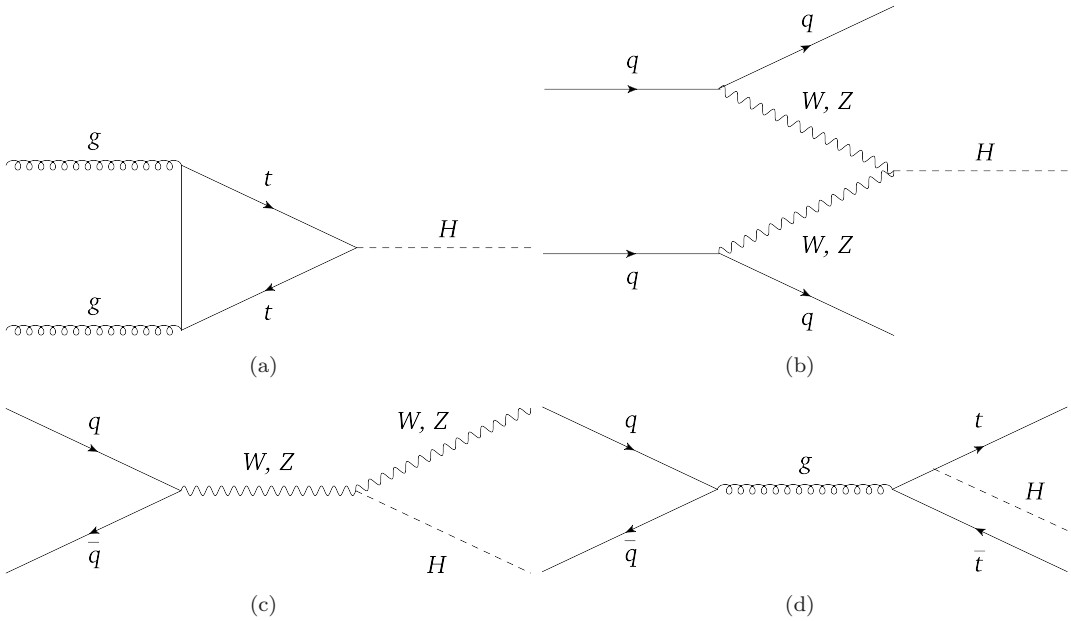

FIGURE 2.3: Feynman diagrams of the most common Higgs production mechanisms at the LHC (a) gluon-gluon fusion (ggF), (b) vector boson fusion (VBF), (c) and (d) associated vector boson and $t\bar{t}$ production

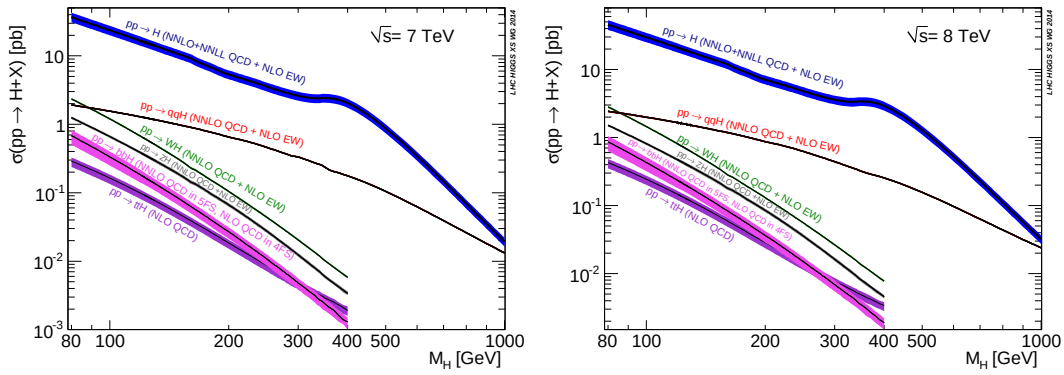

FIGURE 2.4: SM Higgs production cross section as a function of mass [22].

the Higgs. Figure 2.4 shows Higgs production cross sections as a function of mass for $\sqrt{s} = 7$ and $\sqrt{(s)} = 8$ TeV data [22]. The most common Higgs production mechanism is gluon gluon fusion (ggF), figure 2.3 (a), followed by vector boson fusion (VBF), figure 2.3 (b). Associated production mechanisms, figure 2.3 (c) and (d) are less common.

The Higgs boson can decay into a variety of different particles, the rate of each decay mode again depends on its mass. Figure 2.5 shows the main decay channels as a function of Higgs mass [22].

Figure 2.6 shows SM Higgs production cross section times branching ratio at (a) low

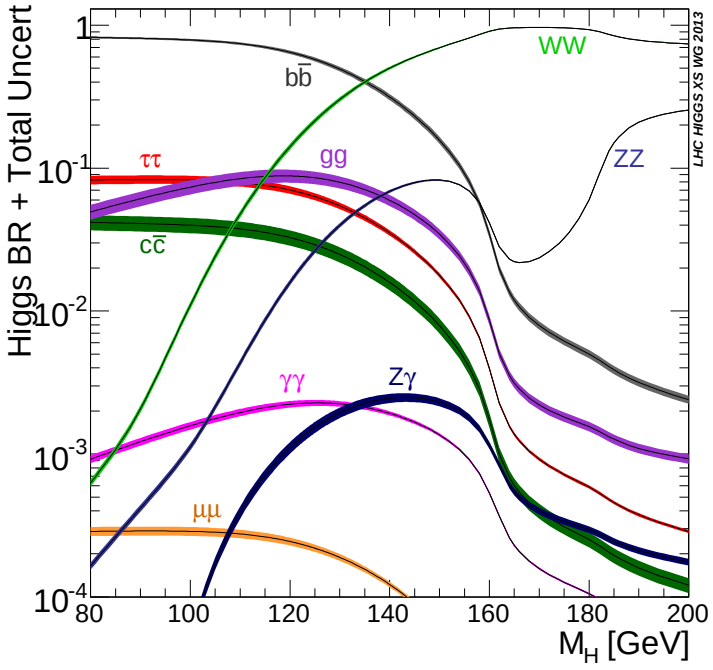

FIGURE 2.5: Branching ratio of SM Higgs boson decay production as a function of mass for the low mass range [22]

mass, and (b) across the entire mass range. At low masses ($m_H \lesssim 130$ GeV) $b\bar{b}$ is dominant, however, a search for $H \to b\bar{b}$ where the Higgs boson is produced via ggF or VBF is made difficult by the high QCD backgrounds produced in a hadron collider. It is possible to utilise associated production with a vector boson, see figure 2.3 (c), where the vector boson decays leptonically. This decay into charged leptons or neutrinos helps separate the $H \to b\bar{b}$ decay from the multijet background and makes it possible to observe this decay at the LHC; the subject of this thesis.

$H \to c\bar{c}$ and $H \to g\bar{g}$ processes can not be studied in the same way. Analysis of $H \to c\bar{c}$ events is difficult due to a lower branching fraction. c-jets are also identified with a much lower efficiency. $H \to g\bar{g}$ has a lower branching fraction and suffers from large backgrounds.

Two other channels, $H \to \gamma\gamma$ and $H \to \tau\tau$ can be studied in this low mass region. Although they have much lower branching ratios than $H \to b\bar{b}$ the signal to background ratio is much higher.

At masses $m_H \gtrsim 130$ GeV it is no longer useful to study the three low mass channels. Here the WW and ZZ decays switch on and become useful before being completely dominant at even higher masses. Initially the $H \to ZZ \to 4l$ channel is the most important as the completely leptonic decay is extremely clean and as the decay contains

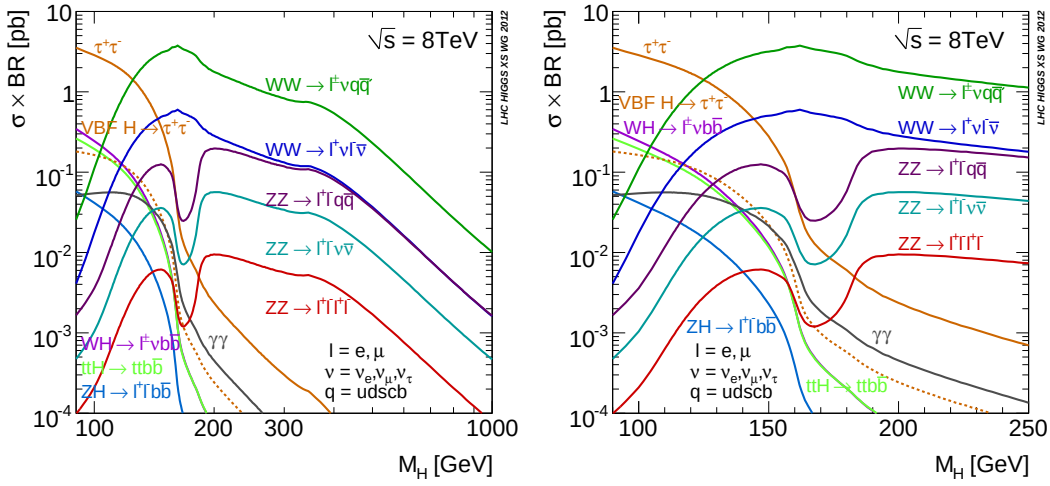

(a) (b)

FIGURE 2.6: Cross section times branching ratio of Higgs boson decay production as a function of mass for (a) the total mass range and (b) low mass range [22]

no neutrinos it offers excellent mass resolution. Due to this even at 125 GeV $H \rightarrow ZZ \rightarrow 4l$ is a major search channel. Approaching $m_H \gtrsim 800$ GeV the $H \rightarrow ZZ$ and $H \rightarrow WW$ decay rate drops. $H \rightarrow ZZ \rightarrow 4l$ starts to play a smaller role due to a reduced overall cross section times branching ratio compared to the other high mass channels.

2.3.2.2 Higgs Searches at the LHC

On the 4th July 2011 two experiments, ATLAS and CMS (Compact Muon Solenoid), showed results which provided evidence for a new fundamental particle which was consistent with the SM Higgs boson [23, 24]. The results combined several decay channels using data collected at $\sqrt{(s)} = 7$ and $\sqrt{(s)} = 8$ TeV.

ATLAS results showed an excess with a maximum located at 126.5 GeV with a local significance exceeding 5σ. Likewise CMS saw an excess with a local significance of 4.9 σ, the maximum was consistent with the ATLAS result. The ATLAS and CMS results can be seen in figure 2.7 (a) and (b) respectively. Combined the ATLAS and CMS results were also able to exclude a Higgs boson at a 95% confidence level over much of the remaining mass range around 126.5 GeV.

Figure 2.8 shows the local significance of the five individual channels input into the ATLAS combined Higgs search. The excess is mainly due to contributions from the $H \rightarrow 4l$ and $H \rightarrow \gamma\gamma$ channels. More analysis was required to confirm the discovery of the SM Higgs boson as predicted by Brout, Englert, Higgs, Kibble, Guralnik and Hagen. For example did the new particle couple to fermions?

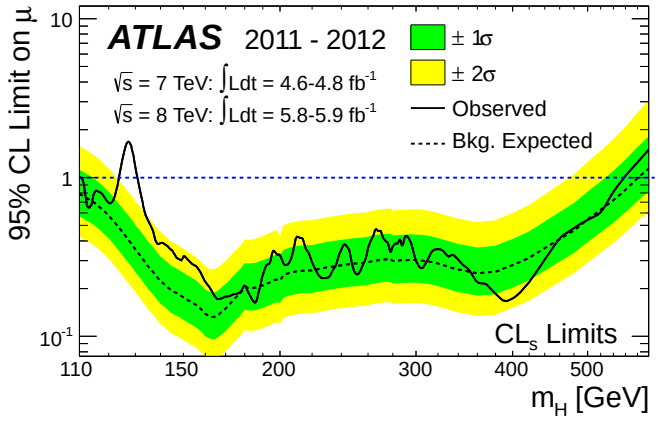

(a)

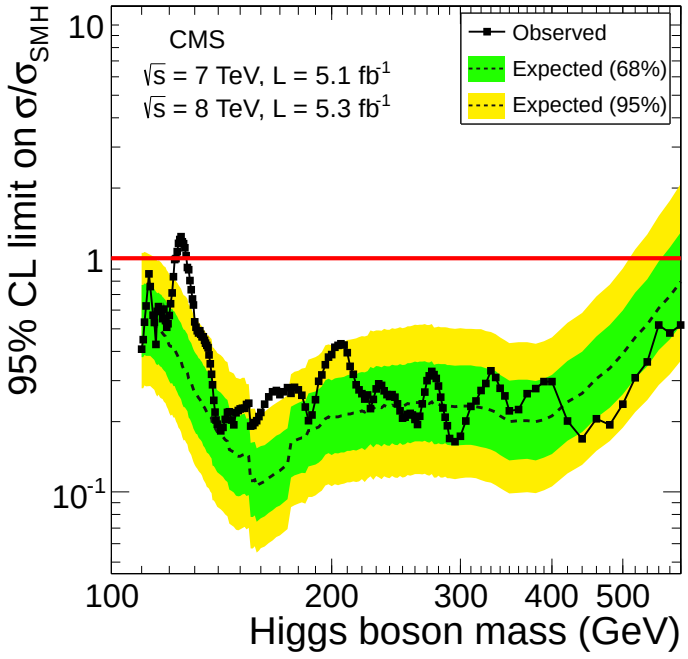

(b)

FIGURE 2.7: Combined search results for (a) ATLAS [23] and (b) CMS [24]. The observed 95% CL upper limit on the signal strength (solid line) is shown with the expected results for a background only hypothesis (dashed line). The green and yellow bands represent the $\pm$ 1 and 2 σ uncertainties on the background only expectation.

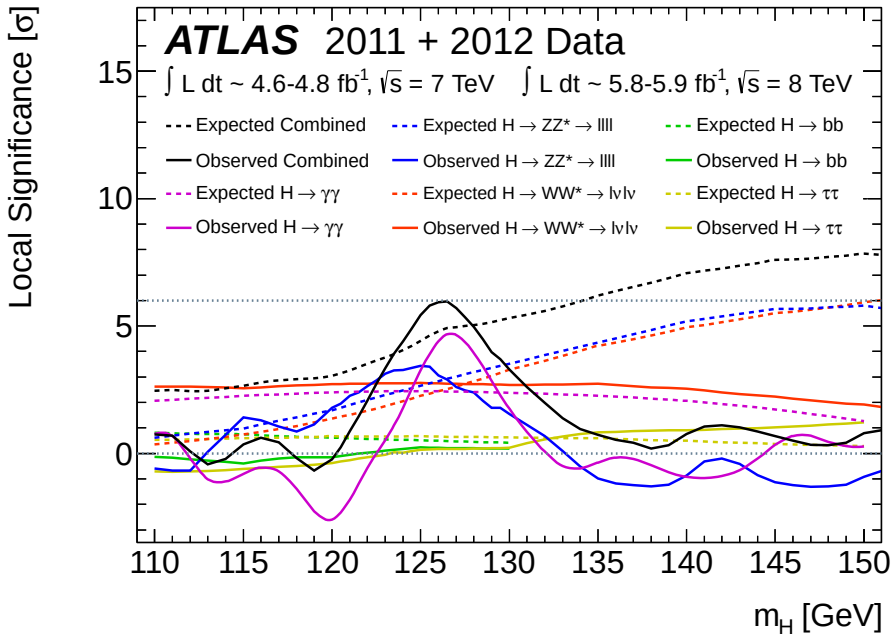

FIGURE 2.8: The local significance shown for individual channels in the ATLAS combination [23].

The ATLAS results on July 4th were based on 4.8 fb^{-1} of $\sqrt{s} = 7$ TeV data and 5.9 fb^{-1} of $\sqrt{s} = 8$ TeV data. The result presented in this thesis is an improved version of the $H \to b\bar{b}$ analysis using the full Run 1 dataset. It is the culmination of several years work which started with the 7 TeV analysis contributing to the July 4th result. The other main channels have also been improved and updated [25–27].

l

Chapter 3

The Large Hadron Collider and ATLAS Experiment

This chapter will first discuss the design of the LHC, highlighting its broad physics program and the key design features of each of its four main detectors. Section 3.2 will then focus in more detail on the ATLAS (A Toroidal LHC ApparatuS) Detector, its components and their performance.

3.1 The Large Hadron Collider

The Large Hadron Collider (LHC) is a hadron-hadron synchrotron collider commissioned and built by the European Organisation for Nuclear Research (CERN).

Located beneath the French-Swiss border near to Geneva, Switzerland, the LHC is designed to run at high energies and luminosities in order to produce rare physical processes in sufficient quantities to study at each of the four interaction points around the 26.7 km ring.

In order achieve such high energy collisions, two counter rotating beams are injected into the LHC after passing through a series of smaller accelerators which are described in more detail in the following section. For the majority of its running time the LHC accelerates and collides bunches of protons and the remainder of this section will focus on this scenario. It should be noted that the LHC is also used to collide heavy ions [28].

Protons in the LHC begin life as hydrogen atoms which are stripped of their electrons in an electric field. The protons are initially injected into a linear accelerator (Linac 2) and are accelerated to an energy of 50 MeV. Following Linac 2, protons pass through three

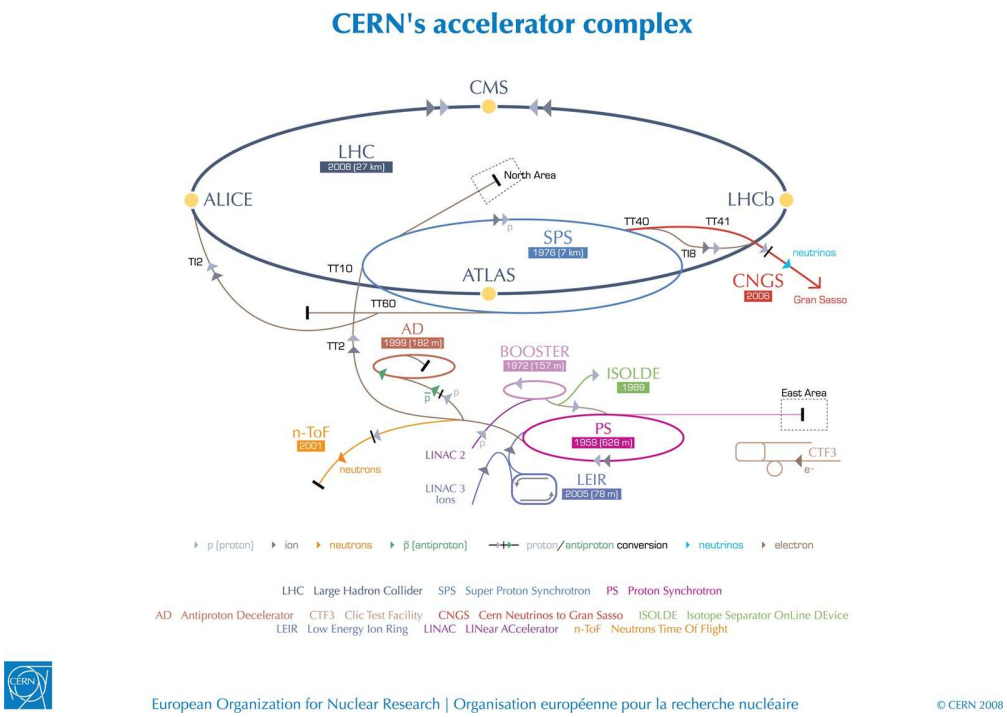

FIGURE 3.1: The LHC accelerator complex [29]

synchrotron accelerators in which the energy of the protons is progressively increased. The Proton Synchrotron Booster (PSB) accelerates the protons to 1.4 GeV, the Proton Synchrotron (PS) to 25 GeV and the Super Proton Synchrotron (SPS) to 450 GeV. From here the beam is split in two and accelerated in opposite directions around the LHC. Details of this can be seen in figure 3.1.

Situated around the LHC beam pipe are four detectors. The locations of these experiments can be seen in Figure 3.2. Of the four detectors two, ATLAS and CMS, are general purpose detectors designed to search for new physics over a broad phase space. Having two general purpose detectors not only increases the amount of data collected, roughly doubling the rate of rare events, but as ATLAS and CMS are able to utilise different technologies and techniques to search for the same signals. Therefore any new physics discoveries in one experiment can be independently cross-checked by the other.

The remaining two detectors, LHCb (Large Hadron Collider Beauty) and ALICE (A Large Ion CollidEr) are more specialised detectors designed with a more defined goal in mind: LHCb is dedicated to b-physics and ALICE is designed to study the physics of strongly interacting matter at extreme energy densities, in particular quark-gluon plasma.

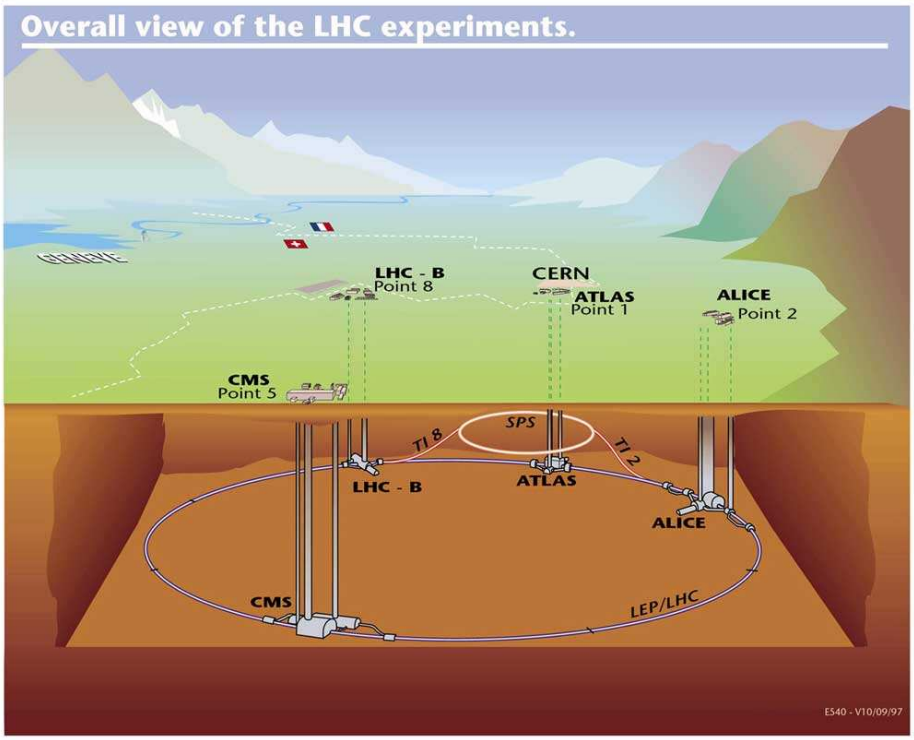

FIGURE 3.2: The location of the four detectors situated on the LHC ring [30]

3.1.1 Luminosity

In any collider experiment, including the LHC, it is important to be able to calculate the number of expected events, N, which will be produced for a given process. This number can be calculated by multiplying the production cross section, σ for the given process by the total integrated luminosity with respect to time, L.

$$N = \sigma L = \sigma \int \mathcal{L} dt \tag{3.1}$$

Cross sections for a number of Standard Model processes can be seen in figure 3.3. The instantaneous luminosity, $\mathcal{L}$, of a pp collider is given by

$$\mathcal{L} = \frac{N_b^2 n_b f_{rev} \gamma_r}{4\pi \epsilon_n \beta^*} F \tag{3.2}$$

where N_b is the number of particles per bunch, n_b is the number of bunches per beam, f_{rev} is the frequency of revolution around the beam pipe, γ_r is the relativistic gamma factor, ϵ_n is the normalised transverse beam emittance, β^* is the beta function at the collision point and F is the geometric luminosity reduction factor due to the crossing

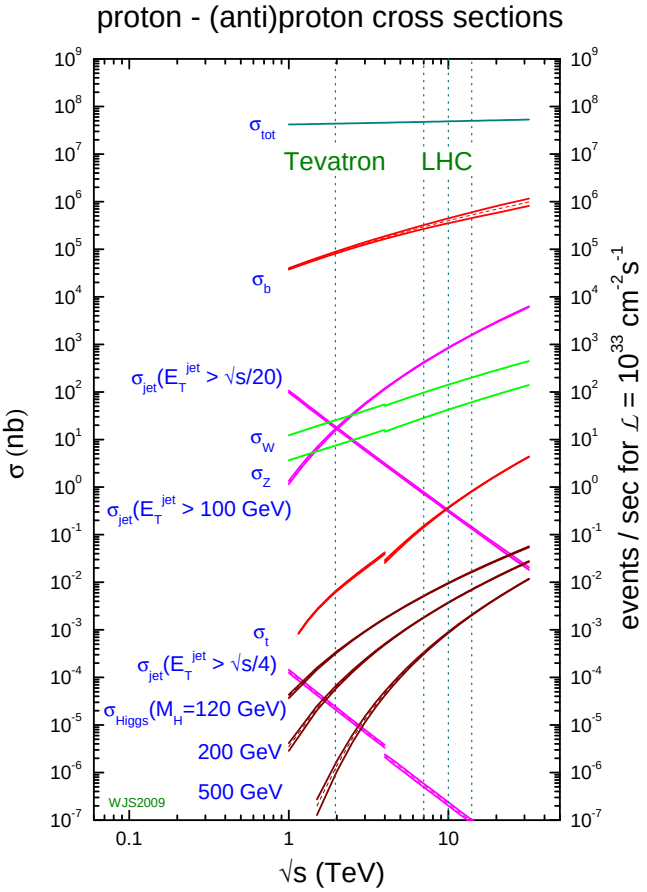

FIGURE 3.3: MSTW 2008 NLO Standard Model process cross sections as a function of collider energy.[31]

angle at the iteraction point. The product of ϵ_n and β^* allows the transverse area of the luminous interaction region at the iteraction point [32] to be calculated. The LHC is designed to provide an instantaneous luminosity of $10^{34}\text{cm}^{-2}\text{s}^{-1}$, which corresponds to approximately one billion proton proton collisions per second.

3.2 The ATLAS Detector

The ATLAS detector [33] is one of two general purpose detectors located on the LHC ring. ATLAS is designed to provide near-hermetic 4π coverage in order to achieve a broad physics program, from searching for new physics to performing precision measurements.

The sub-detectors which make up the ATLAS detector are arranged in symmetric cylindrical barrel layers each with additional end-cap detectors to ensure maximum detector coverage. Figure 3.4 provides a cutaway view of the ATLAS detector and illustrates the layout of the various components described within this chapter. A precision tracking

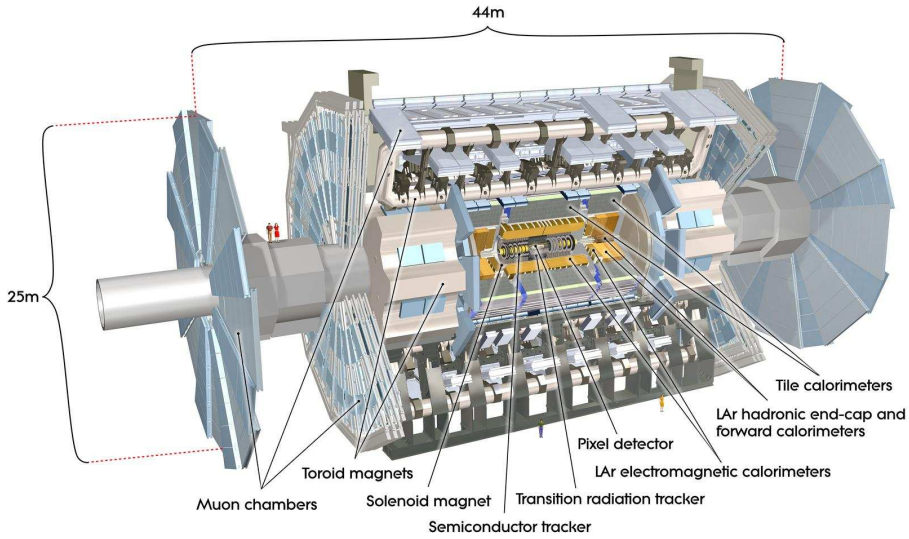

FIGURE 3.4: A cutaway view of the ATLAS detector highlighting the various components [33]

system composed of a silicon pixel detector; a silicon strip detector, the semiconductor tracker (SCT); and a straw tube tracking detector, the transition radiation tracker (TRT), surrounds the beam pipe. The tracking system is submerged in a 2 T solenoid field. Electromagnetic and Hadronic calorimeters are located outside of the magnetic field. Finally the muon tracking system consists of three large superconducting toroids surrounded by an array of muon detectors. The following sections will discuss each of these components in more detail.

3.2.1 Co-ordinate System and Units

Before discussing the various components in more detail it is useful to understand the co-ordinate system used to describe the detector geometry. The ATLAS detector uses a right handed coordinate system where the origin is defined as the nominal interaction point in the centre of the detector. The beam direction defines the z-axis, with the $x-y$ plane transverse to the beam. Positive x points from the interaction point to the centre of the LHC ring, positive y points vertically. The azimuthal angle, ϕ, and the polar angle, θ, are defined with respect to these axes where ϕ is measured around the beam line and θ is measured from the positive z direction. R is defined as the radial distance perpendicular to the beam line.

It is useful to also define rapidity, y. Rapidity describes the angle of a particle relative to the beam axis,

$$y = -\ln\sqrt{\frac{E+p_z}{E-p_z}}. \tag{3.3}$$

Rapidity is hard to measure for highly relativistic particles. Psuedorapidity, η, is used instead where changes in y are invariant under longitudinal Lorentz boosts, η is defined as

$$\eta = -\ln\tan(\theta/2). \tag{3.4}$$

The angular separation (ΔR) between two objects is also invariant under longitudinal Lorentz boosts and is defined as

$$\Delta R = \sqrt{(\Delta\phi)^2 + (\Delta\eta)^2}. \tag{3.5}$$

where ϕ and η are the opening angles between two particles.

It is often useful to measure a variable transverse to the direction of the beam as the partons involved in the collision carry an unknown fraction of the proton's momentum resulting in a boost in the z-direction. Transverse energy, E_T, can for example be defined as $E_T = E\sin\theta$, where E is the particle's energy, and transverse momentum, p_T, can be defined as $p_T = p\sin\theta$, where p is its momentum.

3.2.2 Magnet System

A strong magnetic field is required in order to make precision measurements of the momentum of charged particles. ATLAS utilises a system of four superconducting magnets; a central superconducting solenoid and three outer superconducting toroids. In total the magnet system has a diameter of 22 m and length of 26 m providing a magnetic field over a volume of 12,000 m^3 [33]. Figure 3.5 provides an illustration of the ATLAS magnet system.

The inner solenoid magnet is aligned with the beam pipe and provides a 2 T field for the inner detector. It has a length of 5.8 m and outer diameter of 2.56 m. As part of the design requirements of the magnet system it was crucial that the solenoid magnet would provide a strong magnetic field whilst minimising its radiative thickness. The stong magnetic field was required to provide excellent momentum resolution, whilst the radiative thikness must be as low as possible to avoide particle interactions with the detector.

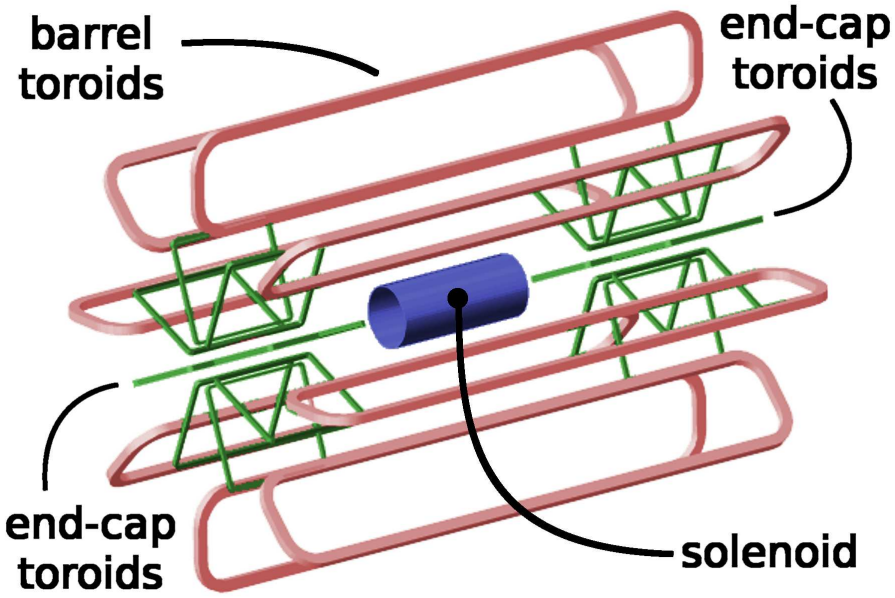

FIGURE 3.5: Geometry of the ATLAS magnet system [34]

The toroidal magnets are divided into three regions. The toroidal barrel, constructed from eight coils which supply a magnetic field to the central muon detectors and two toroidal end-caps for the muon detectors situated in the end-cap regions. In total the toroidal magnets supply a field of 0.5 T and 1 T for the barrel and end-cap respectively.

3.2.3 Inner Detector

The inner detector (ID) lies within a cylindrical envelope of length ± 3.512 m and radius 1.150 m immersed in the 2 T magnetic field produced by the surrounding solenoid.

The inner detector consists of three independent but complimentary sub-detectors: the Pixel Detector, SCT and TRT. It is designed to provide momentum measurements of charged particles, primary and secondary vertex reconstruction within $|\eta| < 2.5$ and moderate charged particle identification. The layout of the various sub-detectors which make up the ID can be seen in figure 3.6.

As well as providing precision measurements, the design of the inner detector takes into account the harsh high-radiation environment within the LHC. The detector components are designed, unless otherwise stated, to last for ten years without being replaced. The design of the ID also considers the amount of material particles must traverse as several interaction effects can effect the accuracy of track measurements. Figure 3.7 shows the cumulative amount of material in terms of radiation length as a function of $|\eta|$.

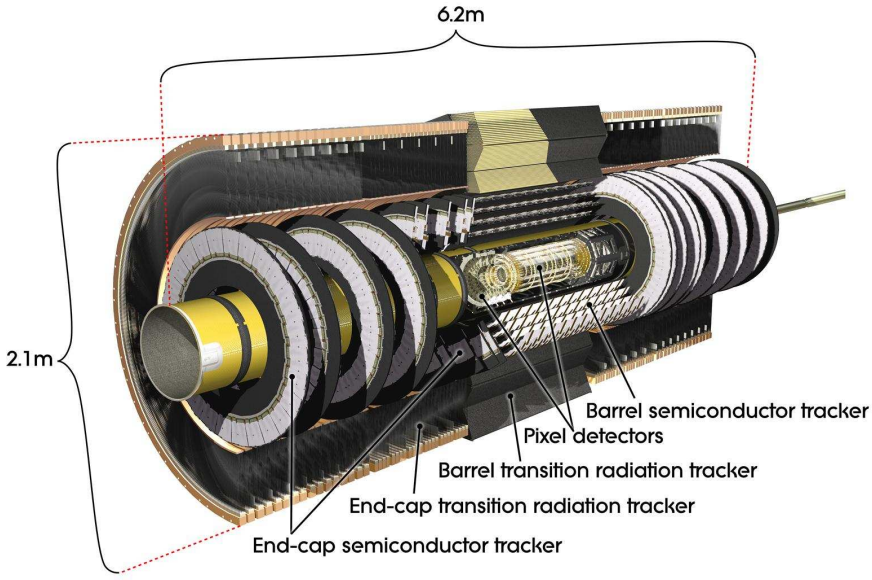

FIGURE 3.6: Schematic diagram of the ID [33]

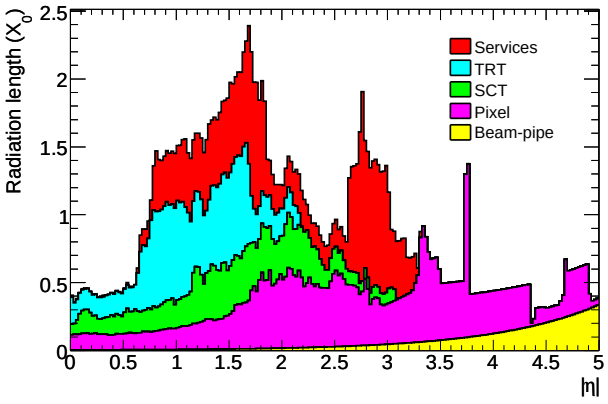

FIGURE 3.7: Total amount of material in terms of radiative length vs η for the various components of the Inner Detector [35].

The key properties of the main components of the ID are given in table 3.1, each component is described in more detail in the following sections.

3.2.3.1 Pixel Detector

The Pixel Detector is the nearest component of the ID to the beam pipe, it also offers the best resolution. A total of 1744 identical silicon pixel sensors make up the Pixel Detector and are arranged as three barrel layers; concentric cylinders around the beam pipe in the barrel region, and two sets of three end-caps located perpendicular to the

Component	Position	Resolution (μm)	η Coverage
Pixel Detector	Inner barrel layer	$R\phi = 10$, z = 155	$\pm$ 2.5
	2 outer barrel layers	$R\phi = 10$, z = 155	$\pm$ 1.7
	End-caps	$R\phi = 10$, R = 155	1.7 - 2.5
Silicon Tracker	Barrel layer	$R\phi = 17$, z = 580	$\pm$ 1.4
	End-caps	$R\phi = 17$, R = 580	1.4 - 2.5
Transition Radiation Tracker	Barrel straws	170 (per straw)	$\pm$ 0.7
	End-cap straws	170 (per straw)	0.7 - 3.5

TABLE 3.1: Key properties of the ID components

beam. Each sensor consists of 47232 50 x 400 μm pixels resulting in a total of around 140 million silicon pixels.

In a typical event three of the pixel layers will be crossed by a charged particle; the interaction produces a series of electron-hole pairs which are separated by an electric field and read out by electronics giving a 'hit' on the pixel. The intrinsic measurement accuracies for each of the barrel layers are 10 μm in the $R-\phi$ plane and 155 μm along the z-axis [33]; the end-caps also have an intrinsic accuracy of 10 μm in the $R-\phi$ plane and 155 μm in R [33]. This accuracy combined with a close proximity to the beam pipe results in the Pixel Detector's high resolution as outlined in table 3.1 and excellent vertexing capability.

3.2.3.2 Silicon Tracker (SCT)

The SCT utilises 4088 silicon strip modules in a similar configuration to the Pixel Detector to provide additional tracking measurements. The barrel region is located at $255 < R < 549$ mm and consists of four concentric cylindrical layers, comprising of 2112 of the 4088 modules. The remaining modules are combined to produce the two end-cap detectors, each consisting of nine disks.

Although the layout of the modules differs in the barrel and end-cap regions their structure is similar. Each module consists of four wafers each containing 768 silicon strips, two on the top and two on the bottom, offset by a stereo angle of 40 mrad. The offset of the modules reduces noise in the detector and allows for 2D track reconstruction. The intrinsic measurement accuracies for the barrel layers are 17μm in the $R-\phi$ plane and 580 μm along the z-axis; the end-caps also have an intrinsic accuracy of 17 μm in the $R-\phi$ plane and 580 μm in R [33].

3.2.3.3 Transition Radiation Tracker (TRT)

The TRT is the outermost component of the ID and utilises gas filled straws to provide further tracking of charged particles through to the calorimeters. The different technology also allows stand-alone electron identification. The TRT consists of 73 layers of straws laying parallel to the beam pipe at $554 < R < 1082$ mm and covers the region up to $|\eta| < 1$. 224 end-cap layers split evenly between the two sides cover the remaining range of $1 < |\eta| < 2$. In total there are 372,000 straws of 4 mm thickness [36]. The straws contained in the barrel region are 144 cm in length, the end-cap straws are 37 cm in length.

As a charged particle passes through the TRT it leaves a trail of ionisation electrons. Each straw contains an anode wire running from one end to the other, the ionisation electrons will drift to the anode. This drift time is used to give a hit location of the charged particle. Furthermore, as ultra-relativistic charged particles pass through boundaries to different media transition radiation photons are produced, these characteristic photons can be used to distinguish between pions and electrons.

3.2.4 Calorimeters

ATLAS calorimetry systems are situated outside of the 2 T solenoid field surrounding the ID. There are two types of calorimeter in the ATLAS detector. The electromagnetic (EM) calorimeter measures the energy of electromagnetically interacting particles and the hadronic calorimeter (HCAL) measures the energy of strongly interacting particles.

Each of the calorimeters consist of a barrel region and two end-caps, one on each side, resulting in a complete ϕ coverage and measurements up to $|\eta| < 4.9$ [33]. The calorimeter layout can be seen in figure 3.8. An important consideration in the design is the depth of the calorimeters in order to maximise containment of electromagnetic and hadronic jets while minimising punch through of jets into the surrounding muon chambers. The total thickness of the ATLAS calorimeter system was chosen to ensure a good E_T^{miss} measurement whilst keeping the total size and hence the cost of the detector to a minimum. An accurate reconstruction of missing energy is extremely important for the physics analysis described within this document.

3.2.4.1 Electromagnetic Calorimeter

Of the two calorimeters the EM calorimeter is situated closest to the ID. It uses lead absorber plates and liquid argon as an active detector medium to measure the incident

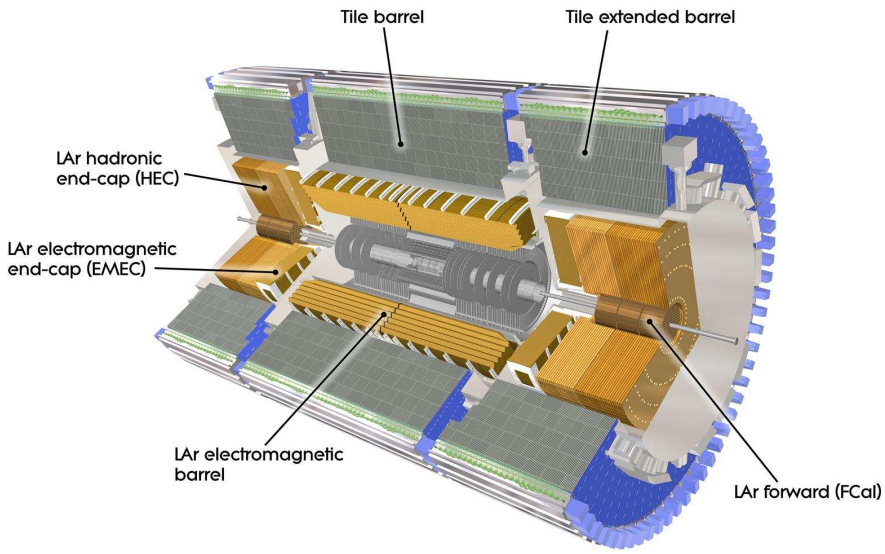

FIGURE 3.8: Schematic diagram of ATLAS calorimetry [33]

energy of electromagnetic showers produced by electrons and photons. It also helps distinguish between different particle types by accurately measuring shower shapes.

The EM calorimeter is divided in to a barrel part ($|\eta| < 1.475$) and two end-caps ($1.375 < |\eta| < 3.2$). The barrel section is constructed of two identical half barrels with a 4 mm gap at $z = 0$, each end-cap is divided into two coaxial wheels: An outer wheel ($1.375 < |\eta| < 2.5$) and an inner wheel ($2.5 < |\eta| < 3.2$). Each section of the EM calorimeter is designed with an accordion geometry, as shown for a barrel module in figure 3.9. This geometry gives complete ϕ symmetry and helps to avoid any azimuthal gaps.

3.2.4.2 Hadronic Calorimeter

The hadronic calorimeter consists of barrel and end-cap regions which utilise different technologies to measure the energy of incident hadronic jets. The barrel region of the hadronic calorimeter consists of a sampling calorimeter using steel as an absorber and scintillating tiles as the active material; it surrounds the EM calorimeter barrel and is sensitive up to $|\eta| = 1.0$. Two further barrels extend the η coverage of the hadronic calorimeter barrel region to $0.8 < |\eta| < 1.7$. The scintillating light is read out by fibres connected to photomultiplier tubes. The hadronic calorimeter end-caps (HEC) are located behind the EM calorimeter end-caps providing coverage in the range $1.5 < |\eta| < 3.2$. Like the EM calorimeter the HEC utilises liquid argon as the active material, however, due to the high radiation conditions a copper absorber is used instead of lead.

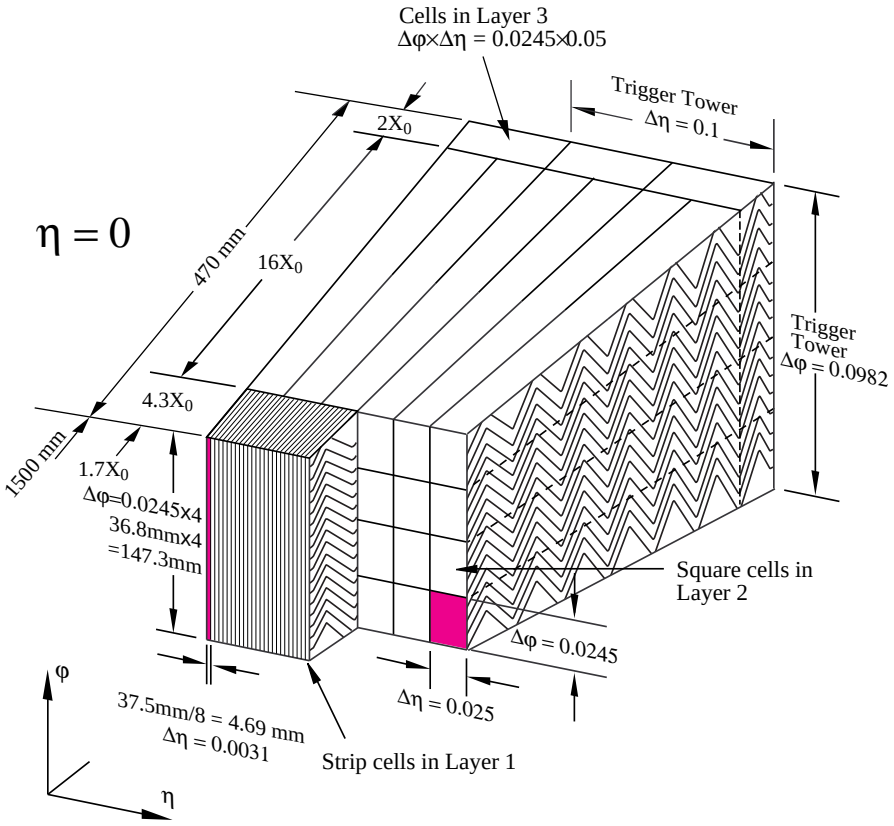

FIGURE 3.9: A schematic diagram of a section of the EM Calorimeter barrel section [33].

3.2.4.3 Forward Calorimeter

The forward calorimeter (FCal) provides extra EM and hadronic calorimetry in the forward regions of the detector, $3.1 < |\eta| < 4.9$. Each end-cap is split into three longitudinal sections that again use liquid argon as an active material. The first section uses copper as an absorber and is optimised to measure EM interactions. The remaining two sections use tungsten and are optimised for hadronic measurements.

3.2.5 Muon Spectrometer

The Muon Spectrometer (MS) is the outermost component of the ATLAS detector. It offers precise momentum measurements of the particles escaping the calorimetry system as their trajectories are bent by the toroidal magnets. As neutrinos will not interact with the detector at all the only particles measured are muons. Barrel and end-cap regions consist of several precision tracking and triggering chambers offering sensitivity in the region $|\eta| < 2.7$ and triggering to $|\eta| < 2.4$. A schematic diagram of the MS can be seen in figure 3.10.

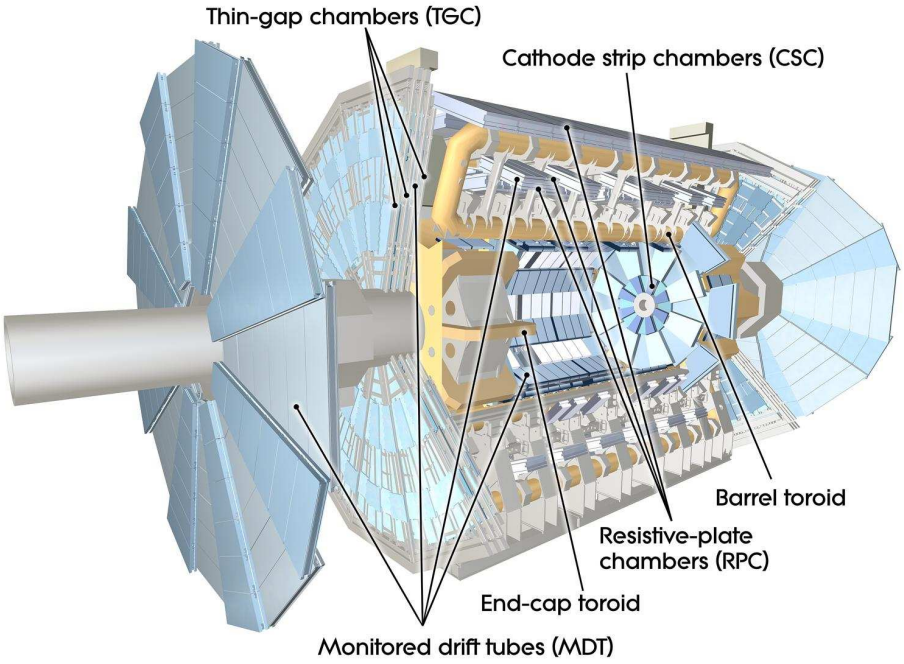

FIGURE 3.10: A schematic diagram of the Muon Spectrometer [33].

The precision tracking chambers in the barrel region use mainly Monitored Drift Tubes apart from the innermost layer in the region $2.0 < |\eta| < 2.7$ where Cathode Strip Chambers are used. For triggering purposes Resistive Plate Chambers are used in the barrel and Thin Gap Chambers used in the end-caps.

3.2.6 Triggers

Running at its design luminosity of 10^{34} cm^{-2}s^{-1} the proton-proton interaction rate within the ATLAS is approximately 1 GHz, far beyond the maximum 200 Hz recording rate constrained by technological limitations. A fast on-line trigger system is required to reduce the initial data to a manageable level [37].

The ATLAS trigger system is split into three levels. A hardware based trigger, L1, and two software based triggers, L2 and the Event Filter (EF) [33]. Combined, the L2 and EF are known as the High-Level Trigger (HLT). This system is outlined in figure 3.11. The criteria required to pass each level of the triggering system can be changed using a trigger menu depending on the running conditions of the LHC.

The L1 trigger uses information from the calorimeter and muon chambers to make an on-line trigger decision: It is designed to reduce the data rate to around 75 kHz. Interesting events which contain high E_T objects such as photons and electrons, jets

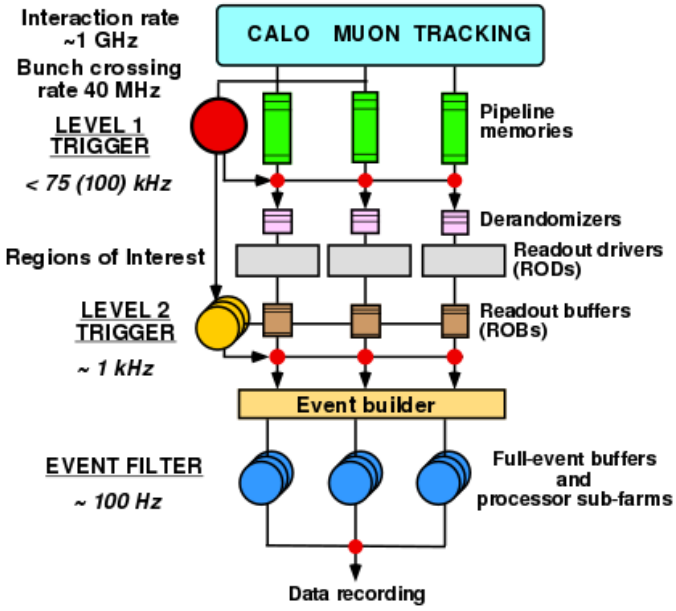

FIGURE 3.11: A block diagram of the ATLAS Trigger System [37].

and harmonically decaying τ leptons as well as events containing high missing transverse energy are identified in the detector and passed on to the HLT for further processing.

The HLT consists of two software based triggers. First the L2 trigger uses more refined event selection using information from the whole detector; the L2 trigger reduces the data rate to 2 kHz. The EF uses reconstruction algorithms similar to those used in the full ATLAS reconstruction, here the data rate is reduced to the required 200 Hz. The complex algorithms used in the EF cause around 4 seconds of read out latency compared to 40 ms at L2 and 2.5 μs at L1. Following the HLT data is separated into different streams and recorded for offline analysis.

3.2.7 Monte Carlo and Detector Simulation

Most physics analyses on ATLAS rely on simulated data in order to compare measured data to predictions when a data-driven estimate of the background is not possible. Furthermore, simulation of predicted signals is required to test new hypotheses and achieve a model dependant understanding of results. Raw Monte Carlo (MC) data is generated using one of many generator packages, [38] provides an overview.

The raw MC data must then pass through ATLAS detector simulation [38] in order to provide an accurate representation of real data being measured by the detector. Stable particles with a lifetime, $c\tau$, greater than 10 mm and the decay products of other unstable

particles are passed through either *full* GEANT [39] or *fast* [40] detector simulation. In *fast* simulation interactions with the ATLAS calorimeter system are parametrised in order to reduce the amount of CPU time taken to produce MC whilst maintaining an accurate simulation of the detector.

Chapter 4

Event and Object Reconstruction

In order to provide meaningful physics it is essential to identify and reconstruct individual physics objects. This chapter describes the reconstruction of the physics objects used by the analyses discussed in this thesis. Details given are relevant to both the 8 TeV b-tagging and Higgs analyses described in chapters 5 and 6 respectively. As would be expected over time prescriptions change with better understanding of the detector and any discrepancies between the definition of physics objects in the two analyses will be made apparent.

4.1 Primary Vertex

When reconstructing events it is important to have a clear definition of the primary vertex. Here the primary vertex is defined as the vertex which, from all reconstructed vertices, has the largest sum of associated track transverse momentum squared, $\sum p_T^2$. It is also required to have at least three associated tracks with $p_T > 400$ MeV.

4.2 Leptons

The accurate reconstruction of electrons and muons is important to the analysis described in chapter 6 in order to reject events which contain either. Electrons are identified by energy deposits in the electromagnetic calorimeter matched with tracks recorded by the ID. Muons generally do not deposit much energy in the calorimeters and can be reconstructed using track segments from the muon chambers and ID.

Leptons can be selected based on a choice of selection criteria; loose, medium or tight. The criteria for each is increasingly stringent increasing the purity of the samples at the

cost of efficiency. In the analyses described in this thesis loose leptons are used. The loose lepton requirements are outlined below as they offer the best efficiency.

Loose leptons are required to have a transverse momentum, $p_T > 7$ GeV. Furthermore in order to ensure the lepton is isolated to reject leptons from semi-leptonic b-decays further selection criteria must be met; the scalar sum of the p_T of all tracks, other than the candidate lepton track, within a cone of radius 0.2 centred on said lepton must be <10% of the p_T of the lepton.

Electrons must have $|\eta| < 2.47$ as well as passing the 'very loose likelihood' requirement described in [41]. Electron energies are calibrated in the data using reference processes such as $Z \rightarrow ee$ and scale factors are applied to ensure that simulations match the recorded data. More information on this procedure can be found in [41].

Loose muons are identified and categorised based upon selection criteria designed to maximise acceptance [42]. Combined or segment-tagged muon are reconstructed in both the muon spectrometer and the ID within $|\eta| < 2.7$. Calorimeter muons are identified if an inner detector track within $|\eta| < 0.1$ can be associated to an energy deposit in the calorimeter. Calorimeter muons recover acceptance in areas of the detector where there is limited muon chamber coverage. Standalone muons are reconstructed only in the muon spectrometer in the range $2.5 < |\eta| < 2.7$ they are used to increase acceptance in η where there is limited ID track coverage.

Muons with an ID track must pass further selection cuts in order to remove muons which are not associated to the primary interaction. In order to reject interactions caused by cosmic muons, muon track selection cuts are made on track impact parameters. Tracks are required to have $d_0 < 0.1$ mm and $z_0 < 10$ mm where d_0 is the transverse impact parameter and is defined as the distance between the point of closest approach of a track to the primary vertex in the transverse, R-ϕ, plane; z_0 is the longitudinal impact parameter, it is the corresponding z position at this point, figure 5.3 illustrates this.

Although they are not used in the analyses discussed in this thesis two further categories of leptons exist, medium and tight. It is useful to introduce them here as they are discussed at several points throughout this document.

Medium leptons must pass the loose selection as well as a series of other more stringent criteria. They are required to have $E_T > 25$ GeV. Medium muons must be reconstructed in both the muon spectrometer and ID within $|\eta| < 2.5$. Calorimeter and stand-alone muons are rejected.

Finally, tight leptons offer the most pure selection; electrons must pass the 'very tight likelihood' criteria [41]. The lepton energy must be 4% or more of the sum of the energy

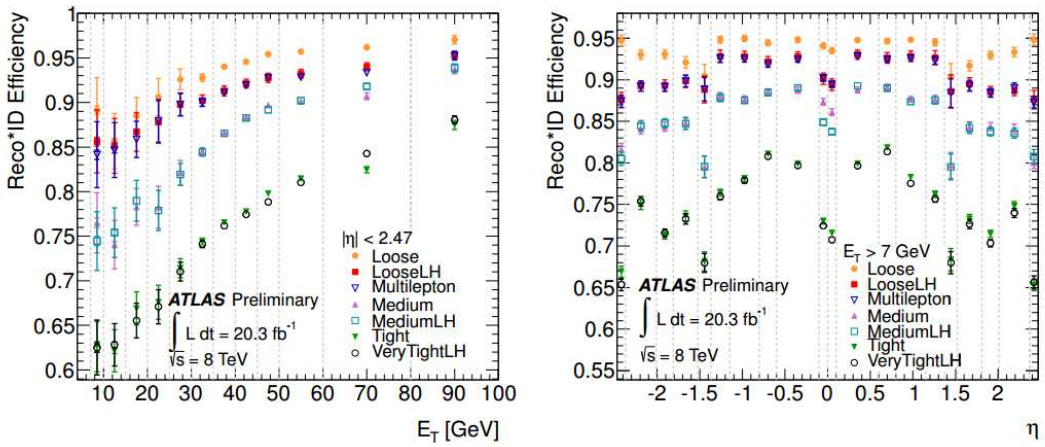

FIGURE 4.1: Electron reconstruction efficiency as a function of η and E_T^{miss} [41].

from calorimeter deposits contained within a cone of radius 0.3 centred around the candidate lepton, not including the lepton. Track isolation requirements are tightened; the scalar sum of the p_T of all tracks, other than the candidate lepton track, within a cone of radius 0.2 centred on said lepton must be <4% of the p_T of the lepton. Lepton reconstruction efficiency varies as a function of η and E_T^{miss}, figure 4.1 shows this for the different selection criteria.

4.3 Jets

Proton-proton collisions at the LHC will produce quarks and gluons. Due to the short range of the strong force and colour confinement, partons, are not directly observable; instead, a shower of particles known as a jet is observed in the detector.

Jets are identified by energy deposits in calorimeter cells. These deposits are clustered together using clustering algorithms and jets are then identified by a jet-finding algorithm, of which there are several available. Any definition of a jet must have both infra-red and collinear safety [43]. Infra-red safety ensures that particles within a jet which don't originate from the fragmentation of the hard scattered parton do not change the number of jets counted. Collinear safety ensures jet reconstruction is not affected by additional collinear radiation, for example if the transverse energy is split into two parts. Figure 4.2 (a) and (b) illustrates possible problems caused by algorithms which do not have infra-red or collinear safety.

In the analyses described in chapters 5 and 6, jets are reconstructed from topological energy clusters in the calorimeters [44]. A clustering algorithm identifies seed cells which

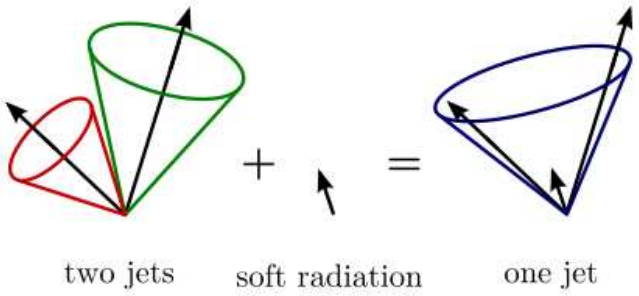

(a)

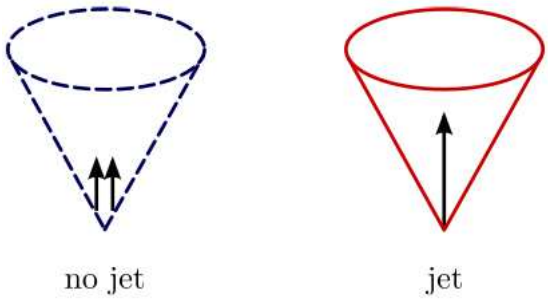

(b)

FIGURE 4.2: Illustration of problems caused by jet algorithms with (a) no infra-red and (b) no collinear safety [43].

have significant energy compared to expected background noise. Neighbouring cells are added to the cluster if they pass a reduced signal to noise threshold. Jets then are reconstructed using an anti-k_t algorithm [45] with a distance parameter, R = 0.4.

In MC, jets are calibrated so that jet energy, on average, corresponds to the energy of the associated stable particles. Jets are corrected using p_T and η dependant scale factors [46, 47]. The calibration takes into account corrections for pileup, vertex location and the energy and direction of the jets. Prior to the EM+JES calibrations jet energies are corrected for the contribution of pileup interactions using a jet area based technique. Further details of this can be found in [48].

Further corrections are applied using a multi-variate approach utilising the jets internal properties; global sequential calibration (GSC) [46] improves the jet resolution without changing the average calibration. The GSC uses variables which are correlated to the calorimeter response to the jet. It sequentially applies corrections to improve the jet energy resolution and to make the jet response, R, less dependant whether the jet is more quark- or gluon-like. R is defined as

$$R =< p_T^{reco}/p_T^{truth} >, \tag{4.1}$$

where p_T^{reco} and p_T^{truth} are the reconstructed and truth jet missing transverse momentum.

Applying a selection cut on the fraction of tracks associated with a jet originating from the primary vertex, the jet vertex fraction, helps to suppress jets originating from pileup events. Associated tracks are identified within $\Delta R < 0.4$ around the jet axis. As pileup jets tend to have a softer spectrum jets with $p_T < 50$ GeV falling within the inner tracker acceptance, $|\eta| < 2.4$, are required to have a jet vertex fraction (JVF) greater than 0.5. The JVF is a discriminent which measures the probability that a jet originated from a particular vertex.

Reconstructed jets are used in the analyses if they meet certain selection criteria. Jets must have $p_T > 20$ GeV and $|\eta| < 4.5$. Jets which are used in any dijet calculations must have $|\eta| < 2.5$, as b-jet tagging algorithms can be only applied in this range. For this reason, jets used in the b-tagging analysis outlined in Chapter 5 must also have $|\eta| < 2.5$, here the jets must have $p_T > 15$ GeV.

Jets which are reconstructed from MC are categorised into four flavours; b-, c-, τ- or light-jets. By assessing the hadron/lepton content of a cone of radius 0.4, centred on the jet axis the jet flavour can be defined. If the jet contains a corresponding hadron or lepton, with $p_T > 5$ GeV, flavour is assigned to the jet in a hierarchical fashion following the order listed above. If is not classified as a b-, c- or τ-flavour jet then it is considered to be a light (u,d,s or gluon) jet.

4.3.1 b-Tagging

Jets originating from the decay of a b-quark are identified using $b-$tagging algorithms which utilise certain features of b-jets, in particular their long lifetimes. Chapter 5.2 describes various b-tagging algorithms in detail.

The b-tagging efficiency is defined as the fraction of b-jets produced by collisions that are correctly identified by the b-tagging algorithms. This efficiency is measured in data and the MC is corrected by applying a p_T dependant data/MC efficiency scale factor to the MC efficiencies [49–52].

4.4 Missing Transverse Energy

In any given event recorded the majority of particles produced in a collision are expected to leave some signature in the detector. As neutrinos do not interact with the detector, their presence may be inferred by reconstructing the missing transverse momentum, E_T^{miss}.

Case	Order	Keep μ	Keep e	Keep jet
ΔR(jet,e)<0.4	1	-	Yes	No
ΔR(jet,μ)<0.4	2	$N_{trk} \leq 3$	-	$N_{trk} \geq 4$
ΔR(μ,e)<0.2	3	if not Calo μ	if Calo μ	-

TABLE 4.1: Prescription for overlap removal showing the order in which ambiguities are considered and the outcome of overlap removal given certain criteria.

E_T^{miss} [53] is defined as the negative vector sum of the transverse momenta associated with all calibrated physics objects (jets, electrons, muons, tau leptons and photons), as well as the energy clusters which are not associated with physics objects.

A track based calculation of the missing transverse energy can also be useful. The missing transverse momentum, $\text{p}_\text{T}^{\text{Miss}}$, is defined as the negative vector sum of the transverse momenta of tracks associated to the primary vertex with $p_T > 500$ MeV and $|\eta| < 2.4$. This variable is used in the analysis described in chapter 6 to reject non-collision backgrounds measured in the calorimet. Non collision backgrounds generally consist of beam induced backgrounds, cosmic particles and detector noise. Fake missing transverse energy can be identified if the missing transverse momentum measured does not point in the same direction. Missing transverse momentum is also used to define the multi-jet background template used in the analysis, a more detailed explanation of its use can be found in section 6.

4.5 Removal of Overlapping Objects

During event reconstruction it is important not to double count energy deposits in the calorimeter. The removal of overlapping objects is carried out following the procedure outlined in table 4.1 where the assessment order is outlined as well as the overlap criteria at each stage. N_{trk} refers to the number of tracks matched to the jet with $p_T > 0.5$ GeV. The requirement on this variable was motivated to maximise the signal acceptance in the VH analysis, described in chapter 6, whilst avoiding counting muons from semi-leptonic b- and c- decays as signal muons.

Chapter 5

Estimating b-Tagging Efficiency Uncertainties in Monte Carlo

As discussed in section 4 many physics analyses undertaken using ATLAS data require that jets originating from the decay of b-quarks are correctly identified. Due to the energy restrictions of the LHC current data driven methods of estimating the b-tagging efficiency are statistically limited to low jet p_T; these data driven calibrations are described in [49–52]. Previously for jets with p_T >140 GeV the derived scale factor from the highest p_T bin was applied and the systematic uncertainty doubled. In this chapter a Monte Carlo (MC) based study is discussed where b-tagging efficiencies are calculated for a range of p_T and η bins. A detailed study of the effect of systematic uncertainties on the measurements provides an important cross check of the data driven results and furthermore the superior statistical power of the Monte Carlo allows the study to extend the p_T range of the calibration.

This chapter will outline details of the analysis with a focus on the most up to date results using tagging algorithms and MC recommended for 2012 analyses. It should be noted that results are also available for tagging algorithms and MC recommended for use in 2011 physics analyses; throughout the chapter any differences in approach will be documented as well as overall comments on results; however, a full breakdown of the 2011 analysis is not shown.

5.1 Samples and Event Selection

The simulated data used in this analysis comprises of $t\bar{t}$ samples generated by POWHEG interfaced to PYTHIA [54]. The parton showering and hadronisation is generated

according to the Perugia2011C tune [55, 56] which uses the CTEQL1 PDF. In total the $t\bar{t}$ sample comprises of ∼10 million events. In order to improve statistics at high jet p_T a complimentary set of simulated multi-jet data is used. The multi-jet MC is generated using PYTHIA 8 and split into eight different samples based on their leading jet p_T. In total this analysis uses ∼21 million events taken from the five leading p_T samples. Similarly, the 2011 analysis used simulated top data generated by POWHEG interfaced to PYTHIA. However the analysis was not extended to higher p_T with any supplementary multijet samples.

Selection cuts are applied to the simulated data in order to ensure the quality of the jets and tracks. For the MC analysis tracks are required to have $p_T^{Track} > 4$ GeV and be within $|\eta|$ of 2.5. Each track is required to leave at least 7 silicon hits, comprising of at least two pixel and at least four SCT hits. There are further requirements placed on the p_T and η of jets; $p_T^{Jet} > 15$ GeV within $|\eta|$ of 2.5.

5.2 *b*-Tagging Algorithms

There are several *b*-tagging algorithms which are available for use by analysis groups. Each algorithm produces an tag weight, ω, which allows for a discrimination between *b*-, *c*- and light-flavour jets to be made, ω is defined as

$$\omega = \log\left(\frac{P_b}{P_c}\right), \tag{5.1}$$

for discrimination between *b*- and *c*-jets and

$$\omega = \log\left(\frac{P_b}{P_l}\right), \tag{5.2}$$

for discrimination between *b*- and *light*-jets, where P_b, P_c and P_l are the probability of the identified jet being a *b*, *c* or *light* flavoured jet as output by the tagging algorithm. The purity of *b*-jets in the sample increases with ω, however, after making a selection based on ω the *b*-jet selection efficiency decreases.

This analysis provides calibration for a selection of *b*-tagging algorithms, further detail on these algorithms is provided below. Table 5.1 outlines the algorithms used and for each the working points which are calibrated in this analysis. Working points are defined by placing a cut on ω, each working point corresponds to a particular integrated *b*-tagging efficiency. The different algorithms are described in the following sections.

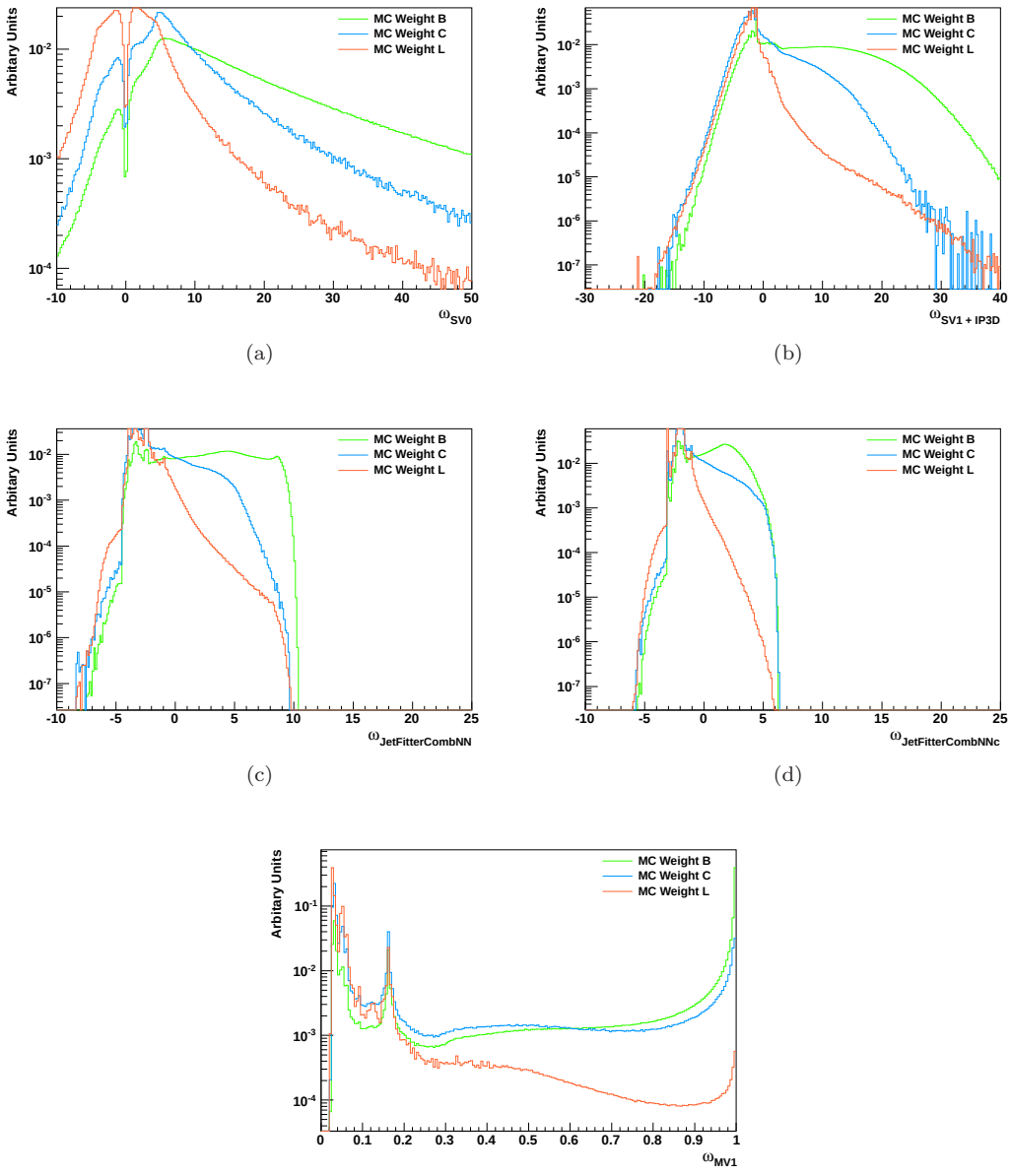

FIGURE 5.1: Normalised tag weight distributions for b-jets produced using the various b-tagging algorithms with MC for the 2011 analysis

Algorithm	Working Points (%)	2011	2012
SV0	50	✓	-
IP3D + SV1	50, 60, 70	✓	-
JetFitterCombNN	57, 60, 70, 80	✓	-
JetFitterCombNNc	50, 55	✓	-
MV1	60, 70, 75, 80	✓	✓
MV1c	50, 57, 60, 70, 85	-	✓
JetFitterCharm	loose, medium	-	✓

TABLE 5.1: An overview of the *b*-tagging algorithms and their working points which are used in this analysis

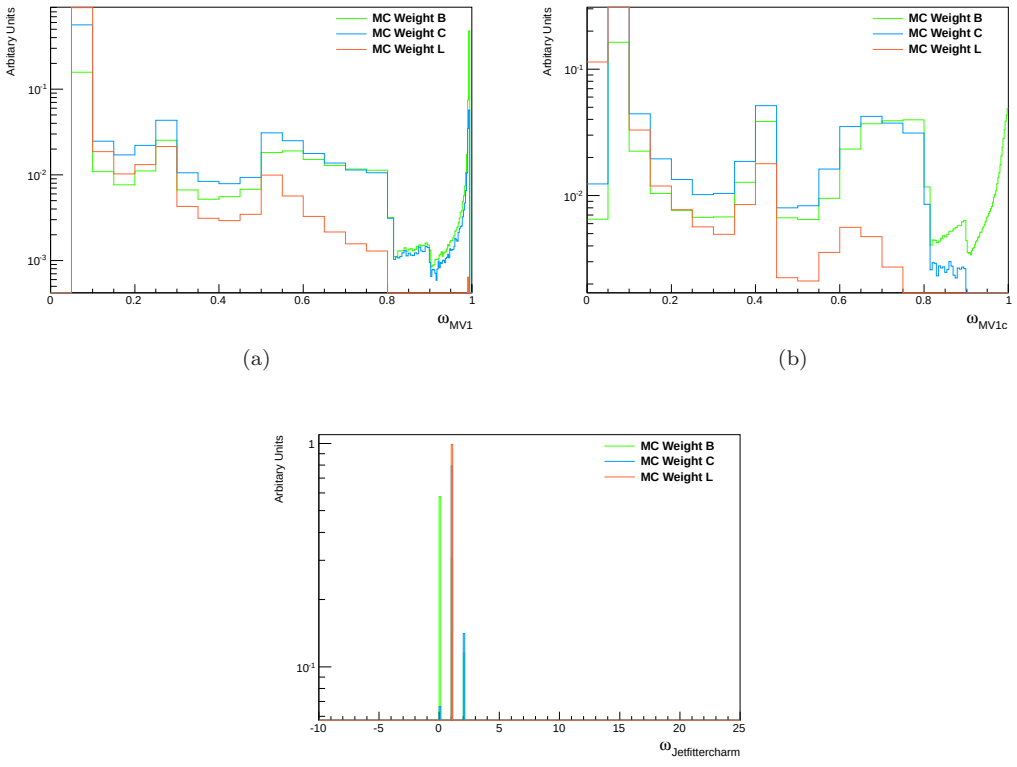

(a) (b)

(c)

FIGURE 5.2: Normalised tag weight distributions for *b*-jets produced using the various *b*-tagging algorithms with MC for the 2012 analysis

5.2.1 SV0

SV0 is a lifetime based b-tagging algorithm, which explicitly reconstructs a displaced vertex using the tracks produced in the decay of a long lived b-hadron. As an input the SV0 algorithm uses a selection of tracks from the decay which pass quality selection criteria. Tracks are then assigned to a secondary vertex through ΔR matching.

The algorithm produces several two track vertices which are displaced from the primary vertex. The two track vertices must pass selection quality criteria before being used to reconstruct a secondary vertex; firstly they must be fit with a $\mathcal{X}^2$ ¡ 4.5, secondly, to ensure that the vertex is incompatible with the primary vertex the measured distance between the primary and secondary vertex measured in three dimensions must have a $\mathcal{X}^2$¿ 6.25. Figure 5.1(a) shows the tag weight distribution for the SV0 tagging algorithm as used in this analysis. More information on the SV0 tagging algorithm can be found in [57].

5.2.2 IP3D + SV1

The SV1 tagging algorithm reconstructs secondary vertices based on a similar principal to the SV0 algorithm, however, a likelihood ratio technique is able to take advantage of three vertex properties to increase discriminating power: the invariant mass of all tracks associated to the vertex; the ratio of the sum of the energies tracks in the vertex to the sum of the energies of all tracks in the jet; and the number of two-track vertices.

The IP3D algorithm takes advantage of the 3D impact parameters of tracks to identify b-jets. The transverse, d_0, is defined as the distance between the point of closest approach of a track to the primary vertex in the transverse, $R - \phi$, place; the longitudinal impact parameter, z_0, is the z position at this point, figure 5.3 illustrates this. Impact parameters (IP) are important quantities to consider when selecting b-jets since B hadrons and mesons are long-lived particles resulting in a non-zero lifetime signed IP, figure 5.4 shows the behaviour of the d_0 distribution for different flavour jets. The IP3D uses these differences and other IP information in a likelihood ratio technique to identify b-jets.

Due to the similar likelihood methods used by SV0 and IP3D they are able to be easily combined by summing the weights produced by the individual tagging algorithms; figure 5.1(b) shows the combined tag weight distribution. More information on both the SV1 and IP3D algorithms can be found in [58].

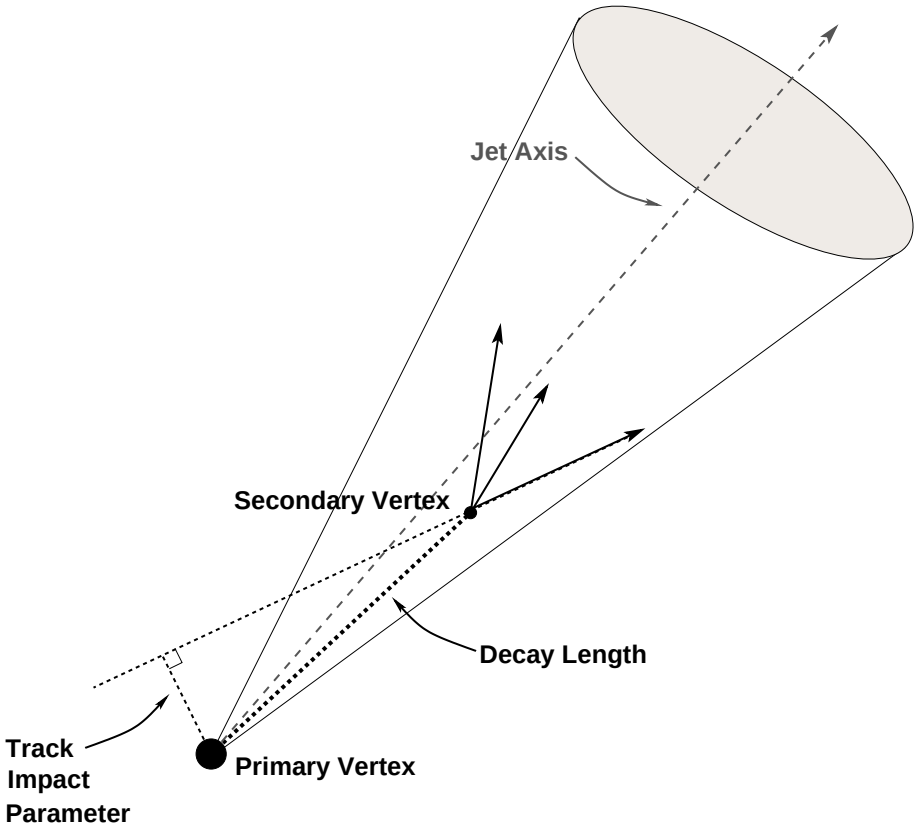

FIGURE 5.3: An illustration of the impact parameter measurement of a track from a secondary vertex [57].

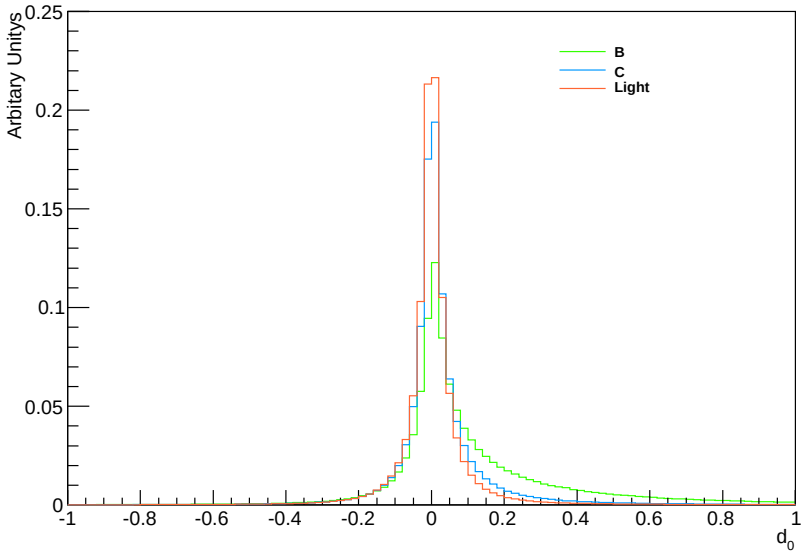

FIGURE 5.4: Measurements of d_0 for different flavour jets.

5.2.3 JetFitterCombNN

JetFitterCombNN is a neural network based algorithm which takes inputs from the IP3D and JetFitter[59] algorithms [58]. JetFitter approximates a flight path for the b- and c-hadrons by exploiting the topology of decays within the jet. Jets are then selected using a likelihood method taking similar inputs to the SV1 algorithm. JetFitterCombNNc works in a similar way, however, the inputs are tuned differently in order to discriminate better for c-jets. The tag weight distribution for both JetFitterCombNN and JetFitterCombNNc can be seen in figure 5.1(c) and 5.1(d) respectively. JetFitterCharm is used in the 2012 analysis and is an improved version of the JetFitterCombNN algorithm, which is trained to reject charm. Unlike the other algorithms JetFitterCharm assigns jets into three categories; loose, medium or fail, as can be seen in figure 5.2(c).

5.2.4 MV1 and MV1c

The MV1 tagging algorithm is a neural-network based algorithm which uses the tag weights of other b-tagging algorithms; IP3D, SV1 and JetFitterCombNN as inputs. The tag weight distribution can be seen in figure 5.1(e) and 5.2(a) for 2011 and 2012 respectively. The MV1c algorithm is calibrated for the 2012 analysis and uses a similar approach to MV1, however the neural-network is trained to reject both charm and light, the tag weight distribution can be seen in figure 5.2(b).

5.3 Uncertainty in Measurements of b-Tagging Efficiencies from Monte Carlo

The b-tagging efficiency, ϵ_b, is defined as the fraction of jets originating from the decay of a b-quark that are identified ('tagged') by the tagging algorithm. When calculating efficiencies from MC simulation it is important to understand the associated uncertainty. A range of systematic effects therefore need to be investigated; each effect is discussed in detail in the following section. Uncertainties are applied to both the 2011 and 2012 analyses unless it is stated otherwise.

In order to calculate the total uncertainty in a given p_T or η bin the effect of each individual uncertainty is measured in a given bin and then added in quadrature. For each bin, using the tag weight distribution, a nominal efficiency, $\epsilon_{nominal}$, can be calculated by calculating the fraction of events which lie below the given tag weight, an associated statistical error is also calculated. This nominal efficiency can be normalised to 1 in order to compare to the data driven b-tagging scale factors. Systematic effects are considered

and applied one by one; for each p_T or η bin a new efficiency is calculated using the same method. Taking the difference between the nominal and shifted efficiency gives an estimate on the effect of each systematic uncertainty in each bin. The total uncertainty is then symmetrised around the nominal efficiency.

5.3.1 Impact Parameter Resolution

In Monte Carlo the detector is simulated with perfect alignment, however the real detector is not perfectly aligned; furthermore its alignment can only be known to finite accuracy. This results in the IP distributions for Monte Carlo being narrower than those seen in data; an effect which must be accounted for when calculating efficiencies. The Monte Carlo d_0 and z_0 are smeared with respect to the primary vertex so that the IP distributions match the data. To calculate these smearing factors the IP distributions are measured in data; a selected track which was used in the primary vertex determination is removed and the primary vertex is then refitted to produce a new vertex, the IPs are then measured relative to this new primary vertex [60]. The effect is propagated through to the efficiency measurement by re-running the b-tagging algorithm and recalculating the efficiencies. The IP distributions with their respective smearing can be seen in figures 5.5(a) and 5.5(b).

5.3.2 Tracks With Shared Hits

Within the ATLAS detector protons collide at extremely high energies resulting in large track multiplicity and high track densities. This occasionally results in more than one charged particle depositing energy in a single detector channel. In such an event the two associated tracks will have a shared hit in the detector. In this analysis a track is flagged as having shared hits if there are one or more shared hits in the pixel detector or at least two shared hits in the strips of the SCT. Unlike the pixel detector, the silicon strips in the SCT provide a precision measurement in the $R - \phi$ direction and only a loose constraint orthogonal to this, this means shared hits are more common in the SCT, as can be seen in figure 5.6; in comparison approximately 98% of tracks in the pixel detector have no shared hits. In order to ascertain the impact of shared hits in the detector, 50% of tracks which have been identified as having shared hits are randomly selected and removed from each event. The b-tagging algorithm is then re-run and the efficiencies are re-calculated.

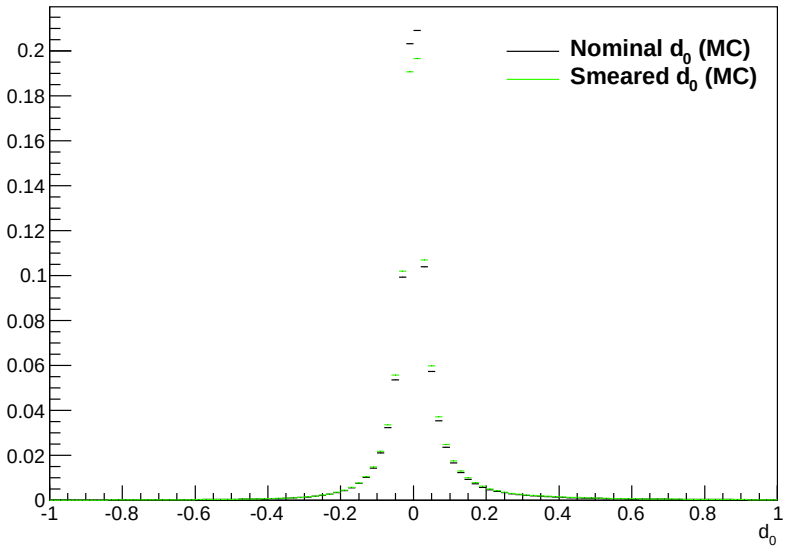

(a) d_0

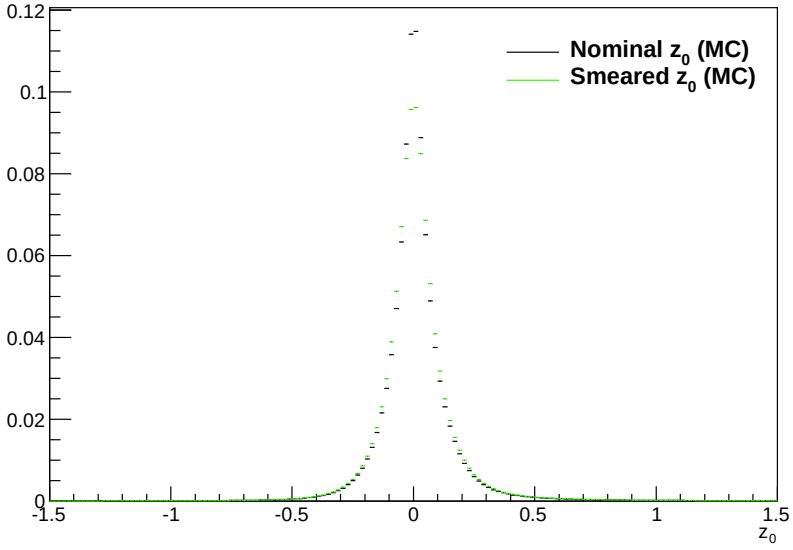

(b) z_0

FIGURE 5.5: The longitudinal, d_0, and transverse, z_0, impact parameter distributions for both the nominal and smeared MC.

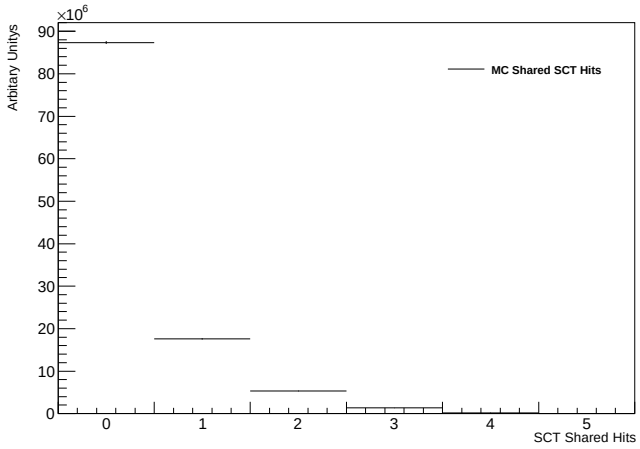

FIGURE 5.6: Distribution of the number of tracks with shared hits as seen in MC by the SCT.

5.3.3 Fake Tracks

Due to pile up, high track multiplicity and high density of hits in the silicon detectors, fake tracks are sometimes reconstructed in the tracker. The number of fake tracks is uncertain as several different sources can contribute to the total number of fake tracks seen in the detector. For example, material interactions or dead sensors can produce incomplete track information leading to fake tracks. The uncertainty on the number of fake tracks must be taken into account when calculating the b-tagging efficiencies.

In this analysis a track is identified as fake in the simulation if the probability that it is a true track is below a certain value. This track probability is taken from the MC and is calculated using a likelihood track matching method described in [61]. An uncertainty is estimated by throwing away a random 50% of tracks which are identified as fake before re-running the b-tagging and obtaining new efficiencies.

5.3.4 Track Multiplicity

The number of tracks measured in a b-jet carries uncertainty from two sources; the difference between the number of charged particles produced from the B hadron decay in simulation compared to data and the efficiency of reconstructing a track in the ATLAS detector. It is possible to take in to account both sources of uncertainty by comparing data to MC in a $t\bar{t}$ dominated sample. The top dominated region gives a good estimate of the associated uncertainties in the track multiplicity distribution because it is pure in b-jets. The distribution can be seen in figure 5.7. A scale factor is determined by taking the ratio of data to MC.

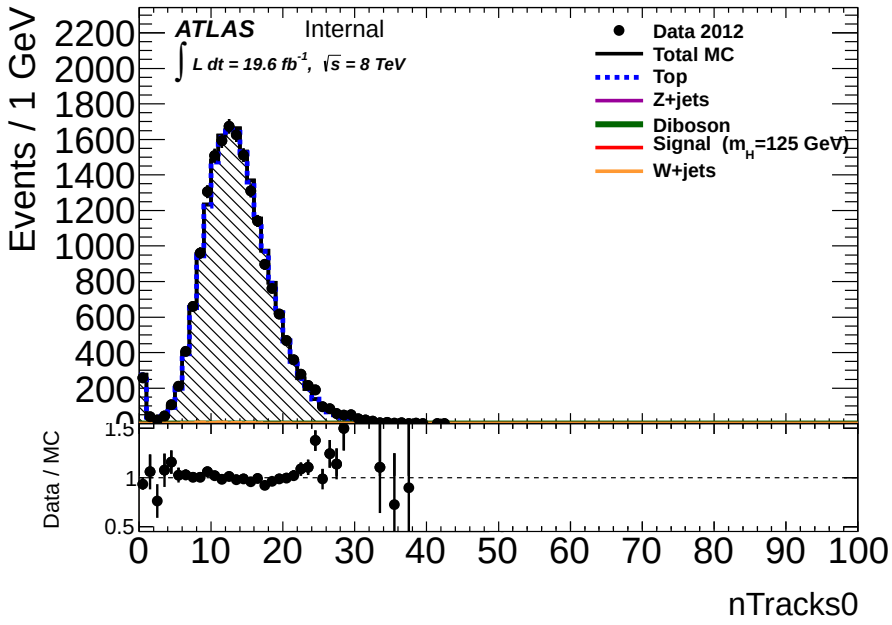

FIGURE 5.7: Distribution of the track multiplicity in a top dominated region before any re-weight. The plot shows various different MC backgrounds, it is clear that top is completely dominating in this region.

To calculate the uncertainty on the measurement of b-tagging efficiency events are re-weighted based on the calculated scale factor. Efficiencies are then re-calculated and compared to the nominal efficiencies.

5.3.5 Jet Axis Resolution

The decay of B hadrons results in a jet of particles which leave tracks in the inner detector and deposit energy in the calorimeter. The jet axis is defined by energy measurements in the calorimeter. Due to the nature of the detector the two measurements may vary with respect to one an other. The jet axis measurement is important to b-tagging as the signed IP which are used in many b-tagging algorithms are measured with respect to the jet axis.

The resolution of the measurement of the jet axis resolution is underestimated in Monte Carlo simulation, therefore it must be smeared in order to match data. To estimate the systematic effect of the jet axis resolution on the efficiency measurement in Monte Carlo the jet ϕ and η distributions are smeared by a Gaussian with width of 0.004 and 0.008 respectively [60]; b-tagging is then re-run and efficiencies are calculated. The effect of this smearing is shown in figure 5.8.

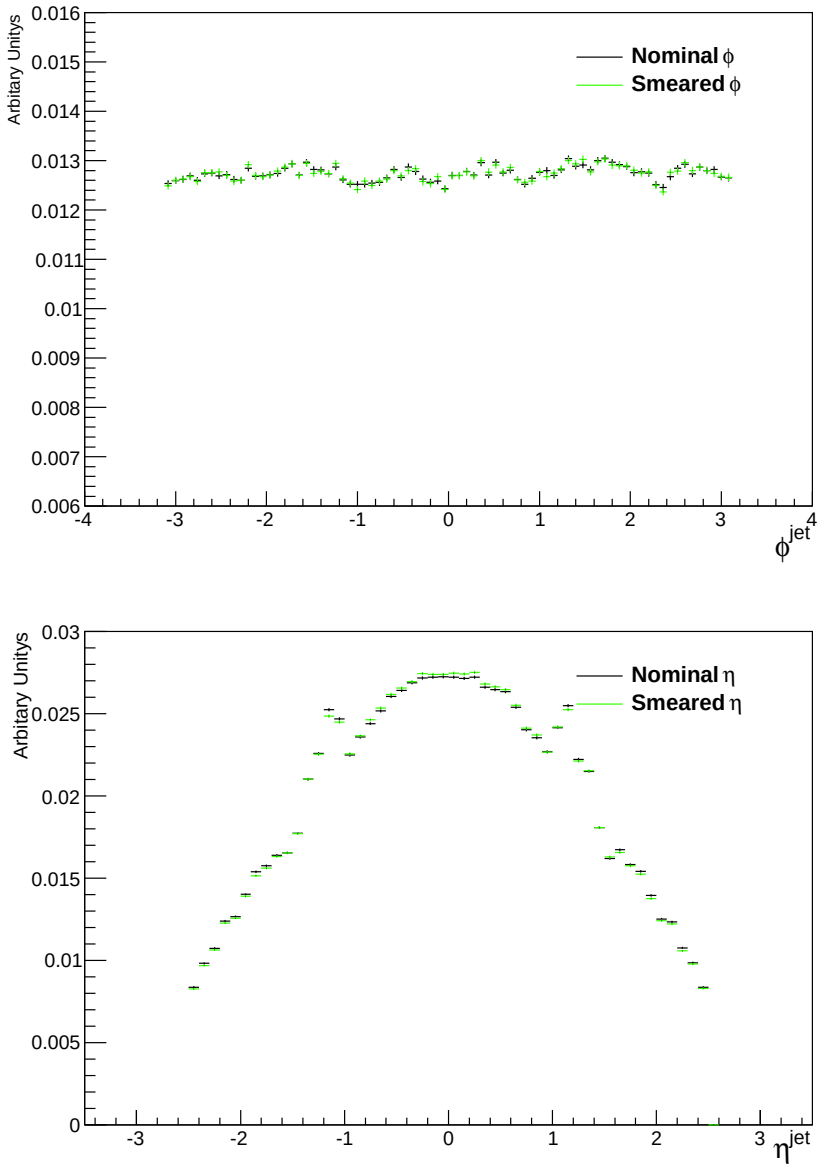

FIGURE 5.8: Distributions of jet ϕ and η shown for the nominal and smeared case. Distributions are smeared by a Gaussian width 0.004 and 0.008 respectively.

5.3.6 Jet Energy Scale and Resolution Uncertainty

Measurement of jet energy carries many different sources of uncertainty. If the jet energy is different in MC and data then the jet p_T spectrum may be biased and cause changes in the binned efficiency measurements. It is therefore important to understand the effect that jet energy uncertainties have on b-tagging efficiencies.

Several sources of uncertainty are considered, a detailed discussion of the JES and associated uncertainties is found in [62]. In general uncertainties are split into four broad categories; detector description, physics modelling, statistics and modelling, and mixed detector and modelling uncertainties. In each case the jet energy is shifted up and down by the given uncertainty, b-tagging is then re-run, efficiencies are calculated and compared to the nominal efficiency.

5.3.7 b-Fragmentation

The transition of a b-quark into stable particles, b-fragmentation, is a complex process and can not be fully described pertubativley, instead it relies on phenomenological models. In order to estimate the effect of the mismodeling of b-fragmentation on the efficiency measurements information is taken from the MC to produce a fragmentation function to be compared to data. In this analysis the fragmentation function, denoted as x, is defined as the ratio of B hadron energy in the rest frame of the fragmentation string to the maximum possible energy it could have recoiling against the b-quark at the other end of the string.

The value of the fragmentation function is not stored on the MC. Instead it must be estimated from information which is stored. Using 2011 MC the resultant fragmentation function can be seen in figure 5.9 compared to experimental results from OPAL [63]. The ratio of the derived fragmentation function to the experimental fragmentation function is calculated and used to re-weight events on a jet by jet basis. The effect of this re-weighting can be seen in figure 5.10. Following the re-weight efficiencies are calculated and compared to their nominal values to give an estimate on the uncertainty. For 2012 the b-fragmentation uncertainty is assessed in separate MC-to-MC scale factors which deal with theoretical uncertainties.

5.4 Results

Efficiencies are calculated as a function of p_T or η, efficiencies can also be seen normalised to 1 in order to compare with the scale factors calculated using data driven methods. The

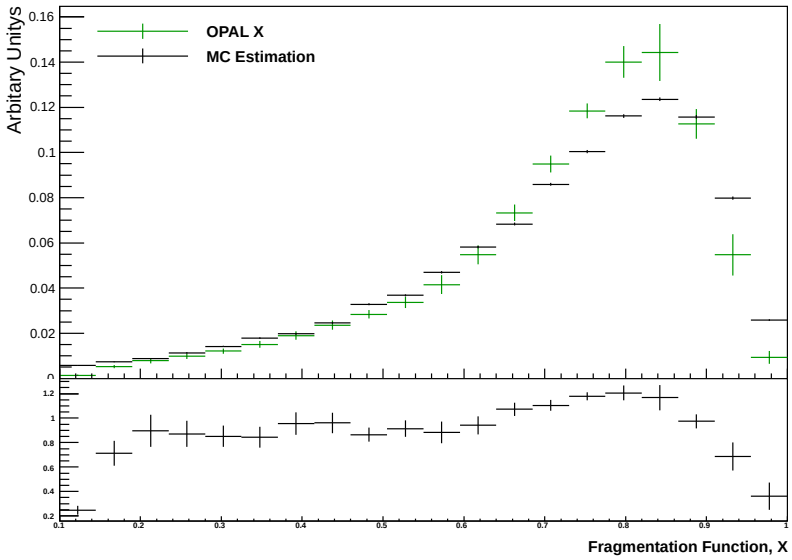

FIGURE 5.9: The estimated fragmentation function compared to results from the OPAL experiment [63]. The bottom plot shows the ratio between the estimated and measured fragmenntation functions.

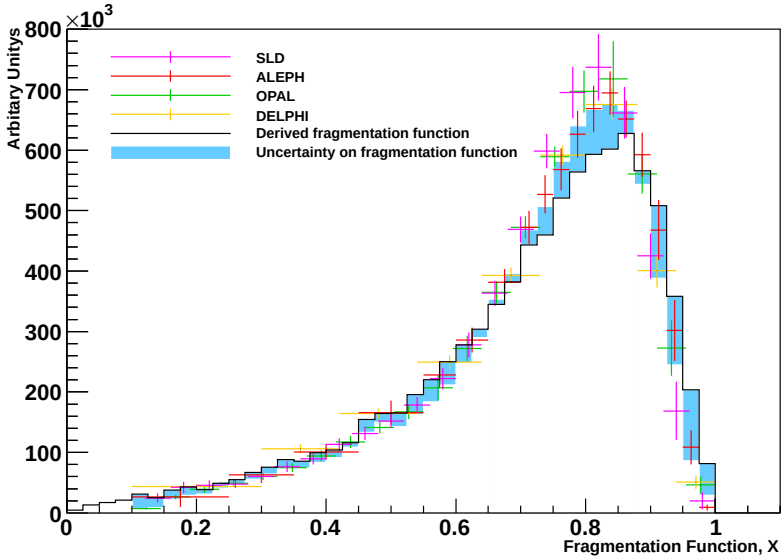

FIGURE 5.10: The blue band shows the effect of the jet by jet re-weighting. Comparable experimental measurements from SLD [64], ALEPH [65], OPAL [63] and DELPHI [66] can also be seen.

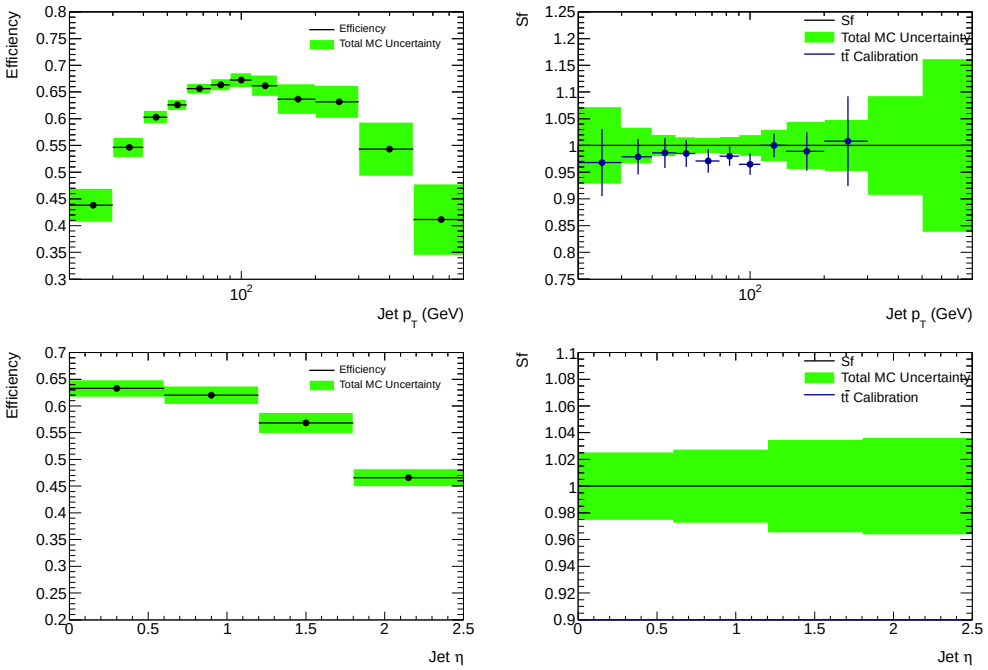

FIGURE 5.11: *b*-Tagging efficiency (left) and scale factor (right) vs p_T (top) and vs η (bottom) for the MV1 tagger at a working point giving 70% efficiency. The coloured bands show the total, symmetrised, systematic uncertainty on each point. The *b*-tagging scale factors are also shown, as a function of p_T and η. Scale factors show the efficiency normalised to one.

contribution from each systematic uncertainty is added in quadrature and symmetrised. Results are shown for the MV1 tagger at a working point with 70% efficiency using the uncertainties described above for the 2012 analysis, details of the further working points for the MV1c algorithm and the other *b*-tagging algorithms as outlined in table 5.1 can be found in appendix A.

5.4.1 *b*-Tagging Efficiency

b-tagging efficiency measures the efficiency with which a jet originating from a true *b*-quark is is tagged by a *b*-tagging algorithm. Figure 5.11 shows efficiency and scale factor vs p_T and η. Scale factors and their associated uncertainties as derived from a data driven analysis [67] are also shown as a function of p_T, the scale factors are consistent with the results from the MC analysis. A more detailed breakdown of the contribution of each uncertainty in each bin can be seen in table 5.2.

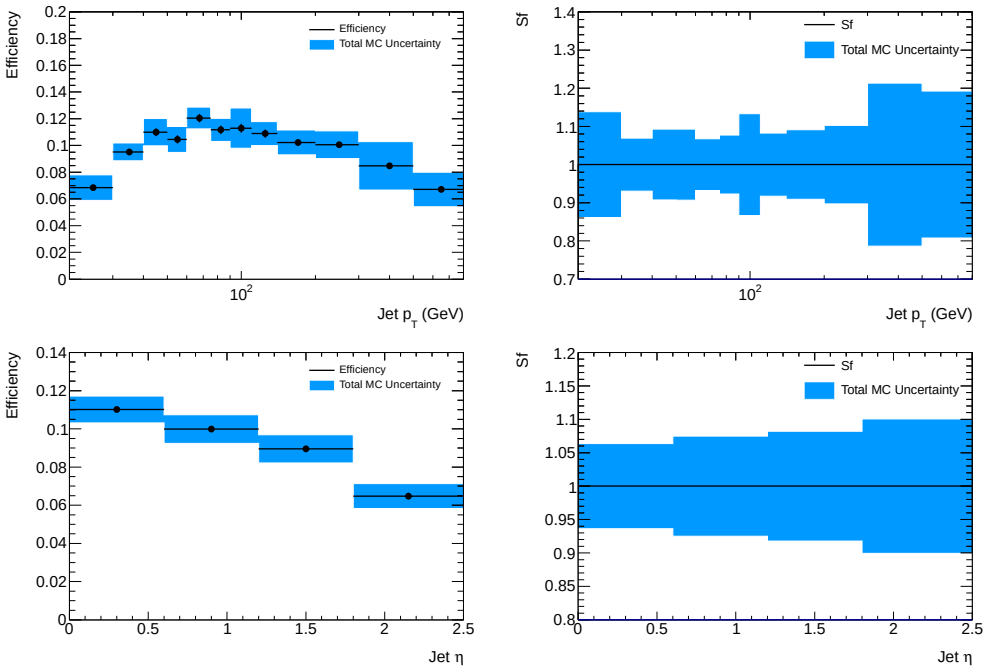

FIGURE 5.12: c-tagging efficiency (left) and scale factor (right) vs p_T (top) and vs η (bottom) for the MV1 tagger at a working point giving 70% efficiency. The coloured bands show the total, symmetrised, systematic uncertainty on each point.

5.4.2 c-Tagging Efficiency

The tagging algorithms can also be used to identify a c-jet, the c-tag efficiency is calculated in the same way but for the probability of identifying a true c-jet, results can be seen in table 5.12. A breakdown on the various uncertainties can be seen in tables 5.3.

5.4.3 Mistag Efficiency

The mistag efficiency is defined as the fraction of jets originating from light-flavour decays which are mistagged as b-jets by the b-tagging algorithm. The mistag efficiency as a function of p_T and η can be seen in figure 5.13 A breakdown on the various uncertainties can be seen in table 5.4.

5.4.4 τ-Tagging Efficiency

Finally the tagging algorithms are able to identify τ-flavour jets, figure 5.14 shows τ-tagging efficiency as a function of p_T and η. A breakdown on the various uncertainties can be seen in table 5.5.

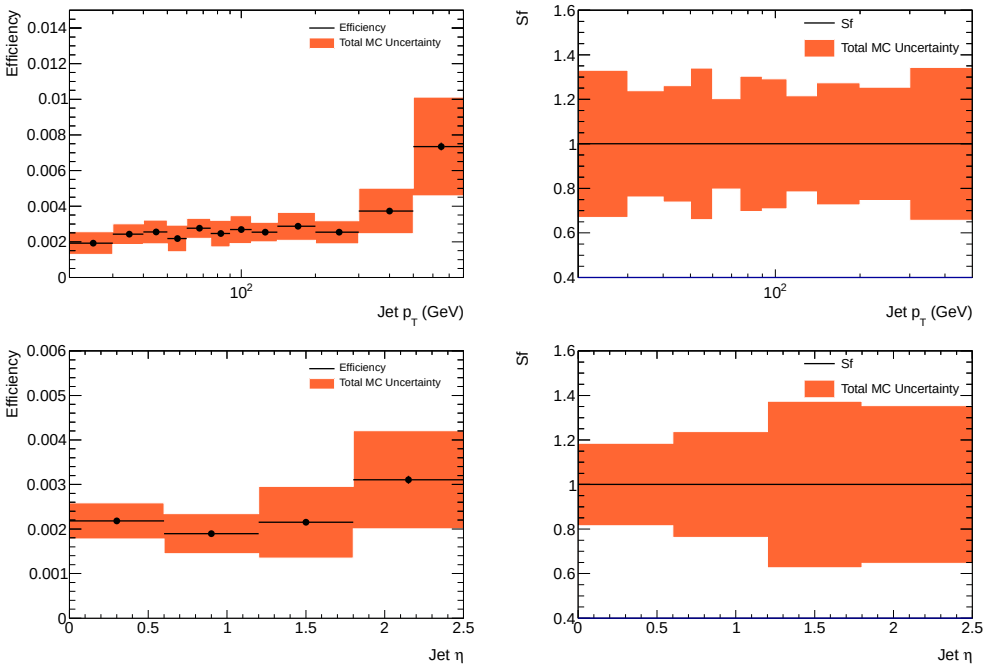

FIGURE 5.13: Mistag efficiency (left) and scale factor (right) vs p_T (top) and vs η (bottom) for the MV1 tagger at a working point giving 70% efficiency. The coloured bands show the total, symmetrised, systematic uncertainty on each point.

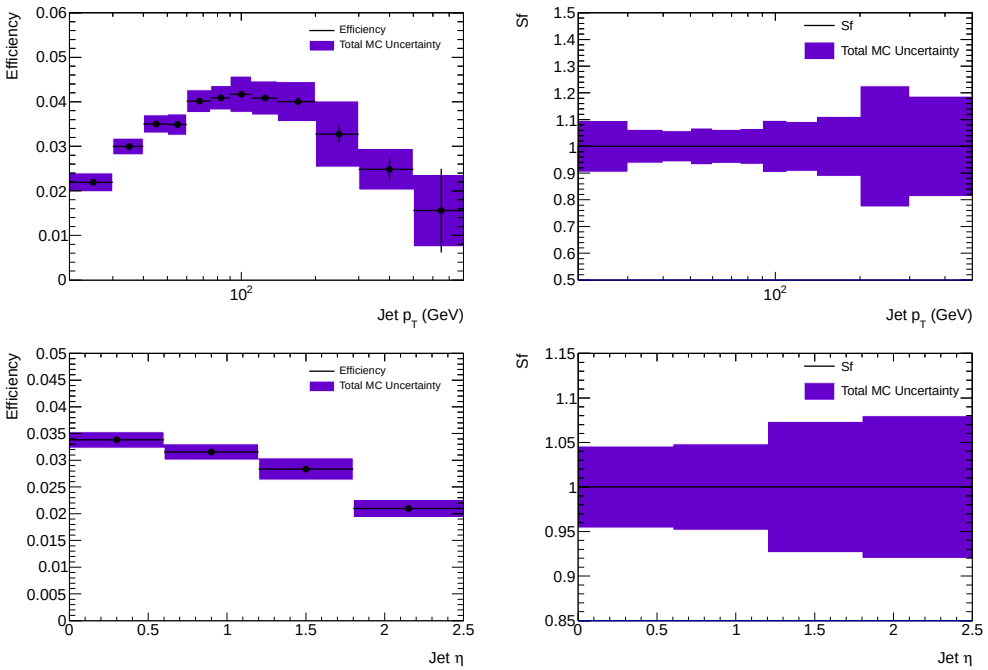

FIGURE 5.14: τ-tagging efficiency (left) and scale factor (right) vs p_T (top) and vs η (bottom) for the MV1 tagger at a working point giving 70% efficiency. The coloured bands show the total, symmetrised, systematic uncertainty on each point.

5.4.5 Conclusion

MC studies on the flavour tagging efficiency of various tagging algorithms are performed using 2011 and 2012 MC as a function of p_T and η have been carried out. A wide range of systematic uncertainties are studied providing an estimate of the uncertainty. The MC studies provide a cross-check of data driven results and due to the superior statistical power provide a better estimate of the total systematic uncertainty at high p_T.

The total uncertainty on measuring b-tagging efficiency in 2012 MC ranges from 1.3% to 20.6% in the p_T range 20-1200 GeV. Jet axis-resolution uncertainties in η and ϕ are dominant in the lowest p_T bins, where as the uncertainty due to shared hits in the detector dominate at $p_T > 200$ GeV, the total uncertainty in the intermediate bins takes contributions from a wide range of systematic effects. Results for c-jets show a similar pattern with the total uncertainty ranging from 6.2% to 39.0%.

Uncertainties in mistag rate are generally larger ranging from 19.1% to 59.1% with fake tracks within the detector and IP effects contributing as the dominant systematic uncertainties. Due to there being fewer statistics in the MC analysis when tagging τ-jets it is only possible to estimate systematic effects up to 800; here the total uncertainties range from 4.7% to 43.1% with large contributions from shared hits and fake tracks within the detector.

MC extrapolation is currently provided for 2012 ATLAS physics analyses for jets up to 1.2 TeV for b-, c- and l-jets, and to 800 GeV for τ flavoured jets; above this range statistical uncertainties become dominant. Without MC extrapolation many analyses which require high p_T jets would not be possible, one such analysis searches for higgs pair production where the higgs decay to four b-jets [68]. Figure 5.15 shows the individual relative impact on the expected limit from each of the systematic sources considered in the analysis; b-tagging is dominant across the whole range; however, it is much larger at high p_T. Without the MC extrapolation this would be the case across much more of the range. In the future the MC analysis could be combined with the data-driven analyses to reduce the systematic uncertainty on the measured b-tagging scale factors.

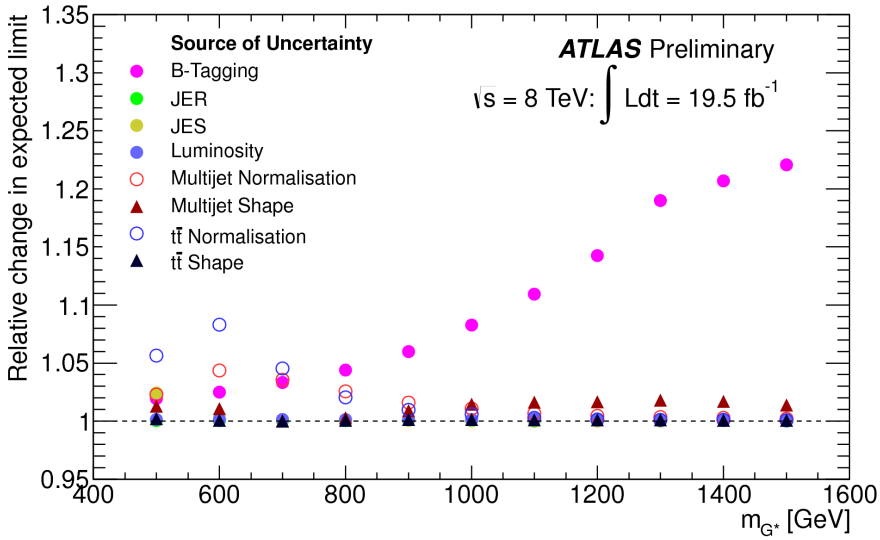

FIGURE 5.15: Impact of systematic uncertainties on the expected limit [68], b-tagging is the dominant uncertainty particulary at high p_T where the MC extrapolation is not applied.

	p_T GeV													
	20-30	30-40	40-50	50-60	60-75	75-90	90-110	110-140	140-200	200-300	300-500	500-800	800-1200	1200-2000
Jet Systs	0.9	0.2	0.6	0.1	0.2	0.2	0.1	0.2	0.5	0.5	0.5	0.6	4.7	14.4
Plie Up	-0.1	0.2	0.2	0.1	0.2	0.1	0.1	0.1	0.3	0.1	0.1	-0.3	0.9	3.8
Track Multiplicity	0.5	0.4	0.3	0.3	0.3	0.2	0.2	0.2	0.4	0.2	0.3	0.2	-0.7	0.8
Smear η	-3.3	-1.5	-0.8	-0.4	-0.5	-0.8	-0.7	-1.3	-1.4	0.4	1.1	3.4	2.6	-13.9
Smear ϕ	-4.1	-2.1	-1.4	-0.9	-0.7	-1.0	-1.2	-2.0	-2.7	-0.3	1.3	1.8	7.6	21.3
Shared Hits	-0.8	-0.1	0.2	0.6	0.8	1.0	1.4	1.4	2.9	4.6	8.7	14.6	17.5	-47.7
Smear d_0	-1.7	-0.9	-0.4	-0.2	-0.3	-0.3	-0.5	-0.9	-1.1	-0.2	0.4	-0.2	-4.0	5.9
Smear z_0	-1.5	-0.7	-0.4	-0.2	-0.3	-0.2	-0.3	-0.6	-0.8	-0.0	0.1	2.4	-1.2	9.6
Fake Rate	-1.3	-0.6	-0.1	0.1	0.2	-0.0	0.0	-0.3	-0.3	1.3	2.2	5.3	3.6	73.8
Total Syst	6.1	2.9	1.8	1.3	1.3	1.7	2.0	3.0	4.5	4.9	9.2	16.2	20.6	93.4
Stat Err	0.9	0.6	0.6	0.5	0.4	0.5	0.5	0.7	0.8	0.9	0.5	1.2	16.2	74.5

	η			
	0-0.6	0.6-1.2	1.2-1.8	1.8-2.5
Jet Systs	0.1	0.1	0.2	0.2
Plie Up	0.2	0.2	0.1	0.1
Track Multiplicity	0.3	0.3	0.3	0.5
Smear η	-1.3	-1.3	-1.6	-1.6
Smear ϕ	-1.8	-2.0	-2.2	-2.4
Shared Hits	0.6	0.8	1.4	1.6
Smear d_0	-0.7	-0.9	-1.0	-0.9
Smear z_0	-0.4	-0.7	-1.2	-0.8
Fake Rate	-0.5	-0.4	-0.2	0.0
Total Syst	2.5	2.8	3.5	3.6
Stat Err	0.3	0.4	0.5	0.8

TABLE 5.2: A breakdown of the contribution of the systematic uncertainties for each p_T (top) and η (bottom) bin using the MV1 tagger at 70% efficiency for b-jets. Values show the percentage error for each point.

	p_T GeV													
	20-30	30-40	40-50	50-60	60-75	75-90	90-110	110-140	140-200	200-300	300-500	500-800	800-1200	1200-2000
Jet Systs	4.0	4.7	4.5	6.2	3.6	3.1	1.7	2.3	0.5	1.0	1.0	1.8	21.4	6.3
Plie Up	1.1	0.1	-0.0	0.3	-0.5	1.1	-0.6	-0.2	0.5	0.5	0.4	0.1	-0.2	-3.4
Track Multiplicity	0.7	0.6	0.1	0.3	0.2	0.5	-0.2	-0.0	0.7	0.5	0.9	0.9	1.7	-0.1
Smear η	-4.3	-1.0	-1.5	-1.9	0.7	-0.3	-3.1	-0.1	0.7	0.0	8.0	3.0	5.6	-7.6
Smear ϕ	-6.5	-1.4	-0.4	-2.5	-1.1	-2.3	-8.4	-0.3	0.9	1.5	8.4	3.0	-3.5	9.4
Shared Hits	-1.0	0.0	1.5	2.1	3.3	3.2	3.7	6.2	6.6	8.1	14.1	15.4	23.5	-80.2
Smear d_0	-3.6	-1.3	-4.1	-2.7	-2.7	-2.7	-7.6	-3.4	-3.5	-3.8	2.1	-4.5	7.8	-72.0
Smear z_0	-4.4	-3.1	0.2	-4.3	-2.2	-3.6	-3.3	-1.0	-3.6	-2.5	0.1	-0.7	4.5	-10.7
Fake Rate	-0.7	1.4	-0.9	0.7	0.5	1.0	-2.1	1.0	3.1	3.6	10.1	9.4	19.6	12.8
Total Syst	10.6	6.2	6.5	8.9	6.2	6.9	13.0	7.6	9.0	10.2	21.1	19.2	39.0	109.9
Stat Err	3.4	3.4	3.7	4.2	3.7	4.1	4.2	4.0	2.7	2.5	2.3	3.3	18.9	65.6

	η			
	0-0.6	0.6-1.2	1.2-1.8	1.8-2.5
Jet Systs	0.2	0.2	0.8	0.3
Plie Up	0.4	0.5	-0.1	0.3
Track Multiplicity	0.3	0.7	0.3	0.4
Smear η	-2.0	-1.5	2.0	-1.3
Smear ϕ	-1.7	-2.5	0.6	-5.8
Shared Hits	3.2	3.8	5.5	4.0
Smear d_0	-4.4	-4.8	-0.6	-1.4
Smear z_0	-1.4	-2.9	-4.1	-6.0
Fake Rate	-0.2	0.8	3.8	2.6
Total Syst	6.3	7.4	8.2	9.8
Stat Err	1.7	1.9	2.5	3.7

TABLE 5.3: A breakdown of the contribution of the systematic uncertainties for each p_T (top) and η (bottom) bin using the MV1 tagger at 70% efficiency for c-jets. Values show the percentage error for each point.

	p_T GeV													
	20-30	30-40	40-50	50-60	60-75	75-90	90-110	110-140	140-200	200-300	300-500	500-800	800-1200	1200-2000
Jet Systs	3.7	1.8	8.7	10.1	4.4	5.5	6.2	6.4	2.6	2.5	2.0	2.1	23.1	34.0
Plie Up	1.1	0.1	2.4	2.0	0.3	0.0	3.0	-0.2	0.3	1.6	-0.1	0.8	-0.5	2.6
Track Multiplicity	0.8	1.6	1.0	1.8	0.9	0.4	1.7	1.4	0.9	0.7	0.5	0.5	-0.2	3.7
Smear η	-2.2	2.0	-4.4	-8.0	7.1	2.2	8.6	0.2	1.0	0.1	-4.5	3.5	3.8	9.2
Smear ϕ	-0.1	-2.6	-1.9	1.0	2.9	9.9	7.8	-2.1	1.0	-2.7	-7.6	1.1	8.7	0.9
Shared Hits	1.1	0.2	-2.1	2.0	5.8	2.7	4.5	8.5	9.3	10.7	15.8	23.9	36.0	73.3
Smear d_0	-5.3	-4.2	-10.4	-9.0	-7.5	-17.2	-9.2	-10.7	-10.7	-13.0	-15.6	-7.7	-6.9	-17.7
Smear z_0	-8.2	-14.7	-17.5	-25.4	-9.2	-15.5	-13.9	-8.7	-16.4	-10.9	-10.2	-5.3	13.8	-79.1
Fake Rate	30.8	16.1	11.7	12.6	10.5	10.9	15.2	8.9	16.1	14.5	19.1	27.0	36.4	18.6
Total Syst	32.7	22.6	25.7	32.6	19.1	28.3	26.8	19.7	27.2	25.1	32.3	37.5	59.1	116.5
Stat Err	4.7	6.4	7.6	9.5	8.1	9.8	8.9	8.6	5.1	4.5	2.9	4.1	22.4	47.0

	η			
	0-0.6	0.6-1.2	1.2-1.8	1.8-2.5
Jet Systs	0.8	0.6	1.4	1.4
Plie Up	0.5	1.0	0.4	1.8
Track Multiplicity	1.3	0.7	1.3	1.3
Smear η	0.4	0.0	-3.1	2.9
Smear ϕ	-2.6	-2.6	-0.6	5.7
Shared Hits	2.4	3.8	4.6	7.3
Smear d_0	-14.1	-8.3	-8.0	-4.2
Smear z_0	-2.3	-11.9	-28.2	-16.3
Fake Rate	10.7	18.1	22.3	29.4
Total Syst	18.3	23.7	37.3	35.3
Stat Err	3.5	3.9	4.2	4.0

TABLE 5.4: A breakdown of the contribution of the systematic uncertainties for each p_T (top) and η (bottom) bin using the MV1 tagger at 70% efficiency for mistagged jets. Values show the percentage error for each point.

	p_T GeV											
	20-30	30-40	40-50	50-60	60-75	75-90	90-110	110-140	140-200	200-300	300-500	500-800
Jet Systs	1.5	0.6	2.9	3.2	1.1	0.8	0.8	1.5	1.3	4.2	1.4	3.3
Plie Up	-0.0	-0.3	-0.5	-0.8	-1.1	-1.2	-1.1	-1.6	-1.6	-2.1	-2.4	-12.2
Track Multiplicity	-0.3	-0.7	-1.0	-1.5	-1.8	-2.2	-2.6	-3.3	-3.5	-5.4	-4.2	-2.9
Smear η	0.3	1.1	0.5	0.7	1.2	1.9	3.2	0.9	1.0	-5.4	-0.8	2.2
Smear ϕ	0.4	0.8	-0.2	0.0	0.5	0.2	1.6	-0.6	-1.9	-11.7	-10.5	3.4
Shared Hits	1.3	2.3	2.2	3.3	3.8	4.9	7.6	7.9	9.7	12.5	13.6	-19.1
Smear d_0	0.4	0.7	0.2	-0.2	-0.4	-0.8	-0.5	-1.6	-1.7	-6.1	1.1	24.9
Smear z_0	-0.0	0.4	-0.3	-0.9	-0.0	-0.6	-0.0	-1.4	-0.6	-4.5	2.0	6.5
Fake Rate	4.4	4.1	2.8	3.3	2.8	2.8	4.0	2.2	1.4	-5.8	2.2	25.4
Total Syst	4.9	5.1	4.7	6.0	5.5	6.6	9.8	9.4	11.0	21.6	18.2	43.1
Stat Err	0.7	0.6	0.7	0.8	0.7	0.9	1.1	1.5	2.9	8.6	14.4	85.4

	η			
	0-0.6	0.6-1.2	1.2-1.8	1.8-2.5
Jet Systs	0.2	0.2	0.2	0.3
Plie Up	-0.8	-0.5	-0.4	-0.6
Track Multiplicity	-1.6	-1.1	-0.9	-1.5
Smear η	0.7	1.0	1.5	1.3
Smear ϕ	0.0	0.3	0.8	0.4
Shared Hits	3.0	3.1	4.3	3.5
Smear d_0	0.4	-0.5	-0.1	-0.4
Smear z_0	1.2	-1.1	-1.3	-1.4
Fake Rate	2.4	3.0	5.3	6.5
Total Syst	4.5	4.7	7.2	7.8
Stat Err	0.4	0.5	0.6	0.9

TABLE 5.5: A breakdown of the contribution of the systematic uncertainties for each p_T (top) and η (bottom) bin using the MV1 tagger at 70% efficiency for τ-jets. Values show the percentage error for each point.

Chapter 6

$ZH \rightarrow \nu\nu bb$ Physics Analysis

6.1 Introduction

The search for the Standard Model Higgs boson is a key goal of the LHC program. Since the LHC switched on many analyses have searched for and ruled out a wide area of phase space. In 2012, both ATLAS [23] and CMS [24] published results showing evidence for a new narrow resonance decaying in to a pair of photons, a pair of Z bosons or a pair of W bosons. This resonance was thought to be the Higgs boson and further study confirmed its discovery. The mass of the Higgs boson was measured to be around 125 GeV [69]. The discovery of the Higgs boson has already been discussed in more detail in section 2.3.

Observing the decay of this particle to a pair of b-quarks would offer the first observation of direct coupling of the Higgs to quarks. This observation is extremely important as at the measured mass of 125 GeV the Higgs boson is predicted to predominately decay to a pair of b-quarks with a branching ratio of $\approx 58\%$ [70]. This is illustrated in figure 2.4. Despite having such a high branching ratio a direct analysis of $H \rightarrow b\bar{b}$ is made impossible by the high multijet background. Instead associated production mechanisms are utilised where the Higgs is produced in association with a Z or W boson (referred to collectively as a V boson). Feynman diagrams showing these processes can be seen in figure 6.1.

The leptonic decay of the associated vector boson helps distinguish the Higgs decay from the large multijet background. This chapter outlines one such decay channel where a Higgs boson is produced in association with a Z boson, which decays into two neutrinos; hereafter referred to as the 0-lepton channel. Similarities between the other 1- and 2-lepton decay channels (illustrated in figure 6.1) make it preferable to perform complimentary analyses which can be analysed and interpreted collectively. Although this

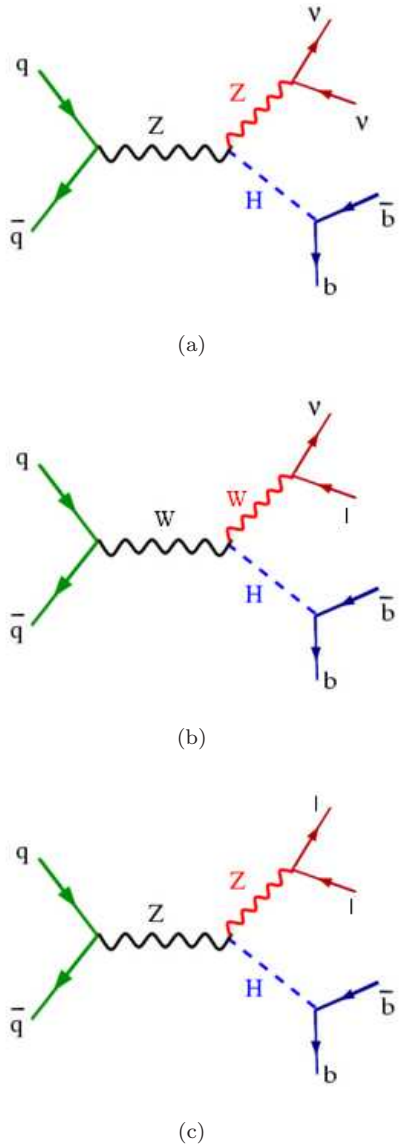

FIGURE 6.1: Feynman diagrams showing Higgs associated production mechanisms with a vector boson decaying to b-quarks (a) $ZH \rightarrow \nu\nu b\bar{b}$, (b) $WH \rightarrow l\nu b\bar{b}$ and (c) $ZH \rightarrow llb\bar{b}$

chapter will primarily discuss the 0-lepton analysis, results will also be shown for the overall VH associated production channel.

The analysis presented in this chapter is the culmination of over three years work. Only the state of the art analysis is discussed. Details of intermediate analyses worked on by the author can be found in [71–73]. The analysis presented is based on work done towards the published VH analysis [74]. It is, however, independent in the fact that all inputs and results have been produced by the author, where this is not the case it will be made clear. Some of the selection criteria in the presented analysis have been

updated to improve on the published result. Section 7.1 outlines any differences between the presented and published analyses and compares the results.

The remaining sections of this chapter discuss details of the analysis. First section 6.2 introduces the data and MC samples used. Section 6.3 discusses the selection of events which are used within the analysis to train and evaluate the multivariate analysis (MVA) described in 6.5. Section 6.6 outlines the various systematic uncertainties associated with the analysis. Finally section 6.7 introduces the statistical method used to extract a result and set limits on the search.

6.2 Data and Monte Carlo Samples

The data used in this analysis is the full 2012 ATLAS proton-proton data collected at $\sqrt{s} = 8$, TeV corresponding to a total integrated luminosity of 20.3 fb^{-1}. Data from ATLAS is split into different periods, A-M, based on run number. As the Z boson in the 0-lepton analysis decays to two neutrinos, data is selected by E_T^{miss} triggers as outlined in table 6.1. More details of the trigger choice and implementation can be found in section 6.3.2.

Trigger Object	Data Period	Run Number	Trigger Name	Luminosity (fb^{-1})
$E_T^{\text{miss}} < 160$ GeV	A - B5	200804 - 203680	EF_xe80T_tclcw_loose	1.919
	B6 - L	203719 - 215643	EF_xe80_tclcw_loose	18.132
$E_T^{\text{miss}} > 160$ GeV	A - B5	200804 - 203680	EF_xe80_tclcw	2.126
	B6 - L	203719 - 215643	EF_xe80_tclcw_loose	18.132

TABLE 6.1: Outline of the different E_T^{miss} triggers used in the analysis and their associated data luminosities.

Simulated signal and background MC are all generated at at same centre of mass energy as the data, $\sqrt{s} = 8$ TeV.

A signal sample is produced for each of the ZH production mechanisms; $q\bar{q} \rightarrow ZH$ and $gg \rightarrow ZH$. Although the quark anti-quark annihilation process dominates ZH production, gluon-gluon fusion contributes approximately 5%. This approximation is, however, a function of p_T due to top quark loop processes [75], the uncertainty increases with p_T. The $q\bar{q}$ signal sample is generated using PYTHIA8 [76] and the CTEQ6L1 [77] parton distribution functions (PDFs) along with the AU2 [78, 79] tune for the parton shower, hadronisation and multiple parton interactions. The gg signal sample is generated using the POWHEG generator [80–82] interfaced to PYTHIA8 with the CT10 PDFs [83], again using the AU2 tune.

The main backgrounds to the analysis are $W/Z+$ jets and $t\bar{t}$ production with additional background contributions from single-top-quark, multijet and diboson (WW, WZ and ZZ) processes. MC is used in this analysis for all backgrounds apart from the multijet background which is derived using a data driven method, details of which can be found in section 6.4. The MC is corrected and normalised in control regions. Table 6.2 lists the various background MC used in the analysis along with their associated generators.

In order to increase the number of events generated and therefore minimise the statistical uncertainty fast simulation is used for the majority of background samples.

Process	Generator
Signal	
$q\bar{q} \rightarrow ZH \rightarrow \nu\nu b\bar{b}/llb\bar{b}$	PYTHIA8
$gg \rightarrow ZH \rightarrow \nu\nu b\bar{b}/llb\bar{b}$	POWHEG+PYTHIA8
$q\bar{q} \rightarrow WH \rightarrow l\nu b\bar{b}$	PYTHIA8
Vector boson + jets	
$W \rightarrow l\nu$	SHERPA 1.4.1
$Z/\gamma* \rightarrow ll$	SHERPA 1.4.1
$Z \rightarrow \nu\nu$	SHERPA 1.4.1
Top-quark	
$t\bar{t}$	POWHEG+PYTHIA
Single Top	
t-channel	ACERMC+PYTHIA
s-channel	POWHEG+PYTHIA
Wt	POWHEG+PYTHIA
Diboson	
WW	POWHEG+PYTHIA8
WZ	POWHEG+PYTHIA8
ZZ	POWHEG+PYTHIA8

TABLE 6.2: A summary of the backgrounds used in the analysis shown with their associated generators.

Each event recorded within the ATLAS detector is subject to so called 'pile-up' events occurring due to soft interactions between protons during a bunch crossing. These interactions result in extra particles measured by the detector which can affect the performance of the detector. In order to account for pile-up events, from minimum-bias interactions are simulated and overlaid on the signal and background MC events. The average number of interactions per bunch crossing, $< \mu >$, is dependant on the luminosity of the beam. As run conditions may change throughout data taking the MC must be appropriately re-weighted to match the measured $< \mu >$ in a given data collecting period.

6.3 Event Selection

The 0-lepton analysis requires a Higgs boson which decays into a pair of b-quarks, observed in the detector as jets, with an associated Z boson that decays into a pair of neutrinos, the presence of which is inferred by missing transverse energy in an event. This section will describe the process of selecting relevant data and discuss how the analysis sensitivity is maximised by separating the data into several different categories. The physics objects used are those defined in section 4.

6.3.1 Preselection

It is essential that the data and MC simulations used in the analysis are accurate and reliable. Before any selection cuts are made event cleaning is undertaken in order to account for any problems with the data. These cleaning cuts are standard throughout ATLAS and account for data quality and known problems in reconstruction.

Data is required to pass a good run list (GRL) which identifies runs where part of the detector was not fully operational. The GRL is produced by the ATLAS collaboration during data taking. Further cleaning cuts remove events which have been identified utilising parts of the detector with known defects, such as hot tile cells in the calorimeter.

6.3.2 Trigger

In order to maximise the acceptance of data into the analysis three E_T^{miss} triggers are utilised. Triggers are selected depending on the run conditions and event E_T^{miss}, as outlined in table 6.1.

To maintain accuracy throughout the analysis the triggers should be studied and well understood. This is of particular importance in the region where the trigger is not 100% efficient; the turn-on. Studies were undertaken by the analysis group in order to understand this turn-on region. Detailed information on this study can be found within the internal note [84]. This section will describe some of the key points and observations.

The E_T^{miss} trigger efficiency, ϵ, as a function of the measured 'offline' E_T^{miss} can be seen in figure 6.2 [84] where it is refered to as EF MissingET. Offline refers to the fact that the measurement is taken by the offline, L1, trigger. After the trigger is applied there is a disagreement between data and MC in the turn on curve. The dependence can be measured and corrected for with scale factors by studying an orthogonal dataset collected using an independent trigger. $W \rightarrow \mu\nu+$ jets and $Z \rightarrow \mu\mu+$ jets samples are

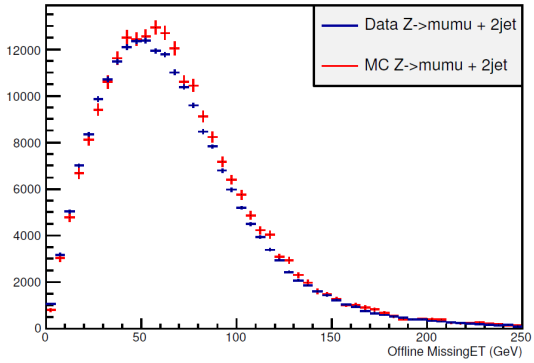

(a)

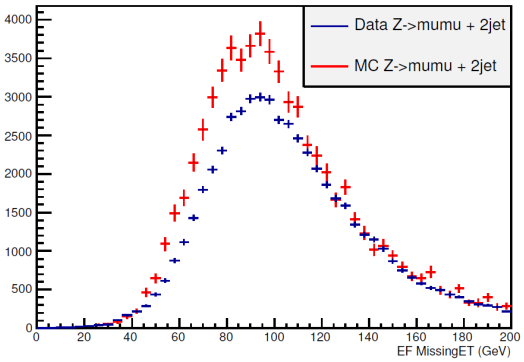

(b)

FIGURE 6.2: Comparison of data and MC E_T^{miss} distributions (a) before and (b) after triggers have been applied [84]. Prior to the triggers data is well described by the MC; dependence between the trigger efficiency and the measured E_T^{miss} causes mismodelling before corrections are applied.

acquired using a muon trigger. To mimic $Z \rightarrow \nu\nu$ events muon spectrometer information is not included in the E_T^{miss} calculation. This data can then be used to calculate the ϵ at each level using the general equation

$$\epsilon = \frac{\text{n passed trigger}}{\text{n passed independent trigger}}. \tag{6.1}$$

The efficiency for each level of the trigger is calculated. The product of the calculated efficiencies gives the total efficiency of the trigger, ϵ_{Total}. The efficiencies calculated using equation 6.1 are plotted as a function of E_T^{miss} and fitted to parametrise the turn-on curve. An example of this can be seen in figure 6.3 for the *EF_xe80_tclcw_loose* trigger [84].

Scale factors can be calculated as a function of E_T^{miss} by taking the ratio of the fitted efficiency curves for data and MC

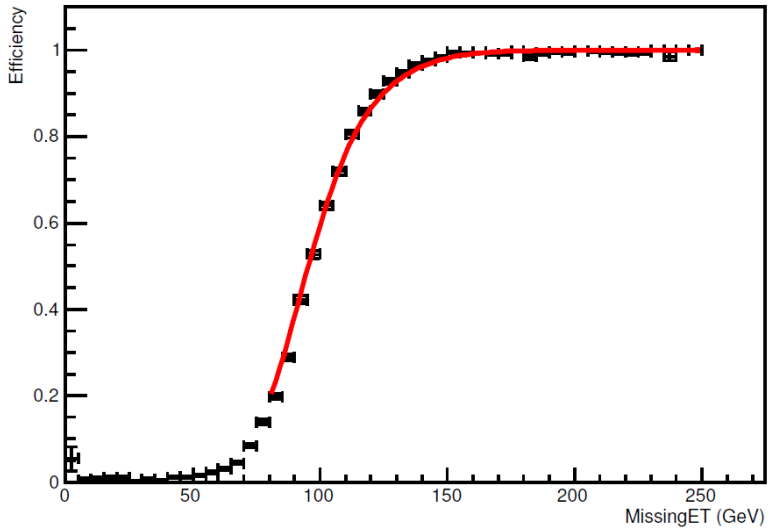

FIGURE 6.3: $EF\_xe80\_tclcw\_loose$ trigger efficiency calculated using $W \rightarrow \mu\nu$ events [84].

$$sf = \frac{Eff(MET)_{Data}}{Eff(MET)_{MC}} \tag{6.2}$$

Figure 6.4 shows a comparison of scale factors calculated using $W \rightarrow \mu\nu$ and $Z \rightarrow \mu\mu$ events [84]. It is shown that the scale factors agree within 3%, this difference is used as a systematic uncertainty.

6.3.3 Lepton Selection

Leptons in the analysis are labelled as loose, medium or tight as outlined in section 4.2. In the $ZH \rightarrow \nu\nu b\bar{b}$ analysis only events which contain no loose leptons are kept.

6.3.3.1 Lepton Inefficiency Study

It is possible to study the lepton efficiency in 0-lepton events using events taken from the orthogonal 1-lepton analysis. Using the method outlined below systematic uncertainties are calculated for various SM backgrounds.

This study was undertaken using the 2013 analysis baseline selection [71]. Two orthogonal samples, chosen before any kinematic selection, are used in the study:

- S0: 0-lepton analysis events

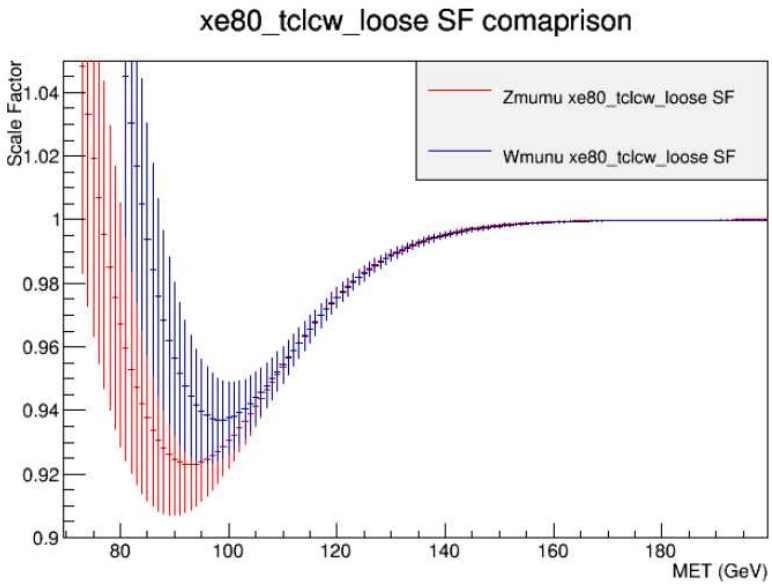

FIGURE 6.4: Comparison of *EF_xe80_tclcw_loose* scale factors as a function of E_T^{miss} calculated using $W \rightarrow \mu\nu$ and $Z \rightarrow \mu\mu$ events [84].

- S1: 1-lepton analysis events, including those which are triggered by the E_T^{miss} triggers. Events must contain at least one reconstructed electron or muon

Both sample 0 and sample 1 must then pass the 0-lepton kinematic selection criteria. Furthermore all events are required to have $E_T^{\text{miss}}(\text{nomuon}) > 120$ GeV.

Due to the selection the total number of events,

$$N = n_{S0} + n_{S1}, \tag{6.3}$$

is constant under a change in lepton efficiency of S1, ϵ_1. Here n_{S0} and n_{S1} are the number of events in S0 and S1 respectively. A loss of events in S0 will result in an increase of events in S1.

$$N = n'_{S0} + n'_{S1} = n'_{S0} + (1 + \epsilon_1)n_{S1}, \tag{6.4}$$

where n'_{S0} and n'_{S1} represent the number of events in S0 and S1 after a change in ϵ_1. From equation 6.4 it can be shown that,

$$\epsilon_1 n_{S1} = n'_{S1} - n_{S1} = \mathrm{d}n_{S1}, \tag{6.5}$$

where $\mathrm{d}n_{S1}$ is the change in the number of events in S1. By equating 6.3 and 6.4

$$\epsilon_1 n_{S1} = -(n'_{S0} - n_{S0}), \tag{6.6}$$

or,

$$\epsilon_1 n_{S1} = -\mathrm{d}n_{S0}. \tag{6.7}$$

The fraction change in the number of events in S0 is therefore,

$$\frac{\mathrm{d}n_{S0}}{n_{S0}} = -\epsilon_1 \frac{n_{S1}}{n_{S0}} \tag{6.8}$$

This gives the lepton inefficiency in 0-lepton events, ϵ_0. The terms on the right can be obtained from the MC, n_{S0} and n_{S1} are the total integrated number of events in the relevant sample and ϵ_1 can be calculated using muon and electron efficiency systematics from the 1-lepton analysis:

$$\epsilon_1 = \frac{S1_{up} - S1_{down}}{S1_{up} + S1_{down}}, \tag{6.9}$$

where $S1_{up}$ and $S1_{down}$ are the total number of events in sample B after applying muon or electron efficiency systematic shifts taken from the 1-lepton analysis [71], see section 6.6 for more details.

The study was undertaken separately for 2-jet and 3-jet events in the relevant analysis backgrounds; $t\bar{t}$, single top, W, WW and WZ. Results can be seen in a range of p_T^V bins for electrons and muons, here p_T^V is the transverse momentum of the vector boson, in table 6.3 and 6.4 respectively. The uncertainties on lepton inefficiency vary from 0.1% to 2.8%, in general the inefficiency is smaller for muons than electrons and increases with p_T^V.

These scale factors are then applied as normalisation uncertainties to the relevant background processes.

6.3.4 Jet Selection

Selected jets are used to define the Higgs boson decay. Jets are selected following the criteria given in section 4.3.

Background	E_T^{miss} (GeV)	Veto Efficiency (%)	
		2-jet	3-jet
$t\bar{t}$	120-160	0.92	0.75
	160-200	1.47	1.30
	200+	2.67	2.06
Single Top	120-160	0.57	0.50
	160-200	1.32	1.03
	200+	2.74	2.07
W	120-160	0.59	0.46
	160-200	1.26	1.06
	200+	2.80	1.91
WW	120-160	0.42	0.23
	160-200	1.00	0.58
	200+	1.80	0.98
WZ	120-160	0.10	0.11
	160-200	0.20	0.20
	200+	0.29	0.27

TABLE 6.3: Electron efficiency in the 0-lepton events.

Background	E_T^{miss} (GeV)	Veto Efficiency (%)	
		2-jet	3-jet
$t\bar{t}$	120-160	0.73	0.68
	160-200	0.83	0.71
	200+	1.02	0.81
Single Top	120-160	0.55	0.48
	160-200	0.78	0.66
	200+	1.20	0.90
W	120-160	0.58	0.48
	160-200	0.80	0.65
	200+	1.19	0.80
WW	120-160	0.46	0.27
	160-200	0.62	0.34
	200+	0.75	0.39
WZ	120-160	0.11	0.11
	160-200	0.13	0.12
	200+	0.12	0.12

TABLE 6.4: Muon efficiency in the 0-lepton events.

Two types of jets are used in the analysis. Signal jets must have $p_T > 20$ GeV and $|\eta| < 2.5$. Forward jets must have $p_T > 30$ GeV and be within $2.5 < |\eta| < 4.5$.

In order to increase the sensitivity of the analysis several jet categories are utilised, separated by the number of signal, forward and b-tagged jets. Events containing two b-tagged jets are then further categorised.

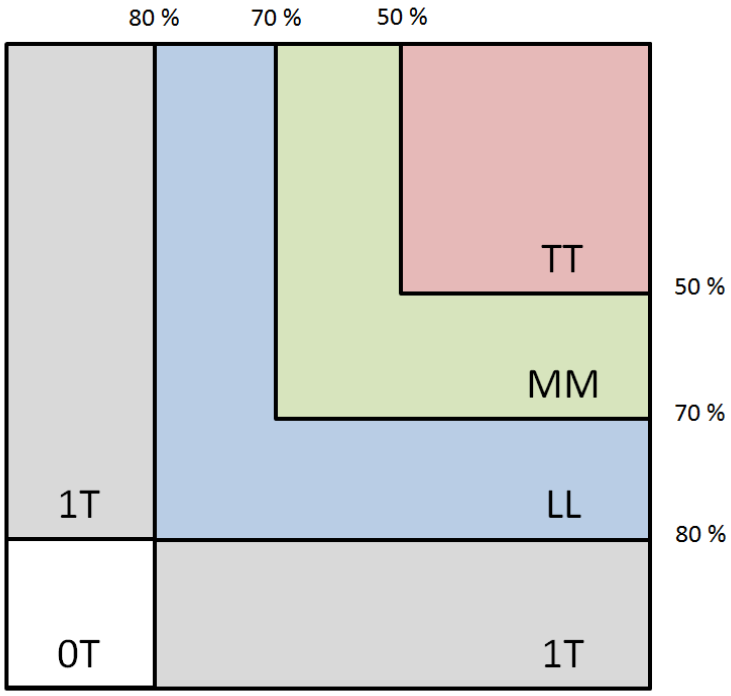

FIGURE 6.5: An illustration of the different b-tagging categories used in the analysis as a function of b-tagging efficiency.

Events are first split into jet categories. Events which contain exactly two signal jets and no forward jets are labelled as '2-jet' events, while events which have a total of three signal and/or forward jets are labelled as '3-jet' events. One of the jets, which is to be used in the dijet mass calculation, from each event must have $p_T > 45$ GeV.

Both 2- and 3-jet events are then further divided into one of five b-tagging categories, 'TT', 'MM', 'LL', '1T' or '0T'. The categories are defined by the number of b-tagged jets within the event. The MV1c tagging algorithm (see section 5.2.4) is used at several operating points to identify and label b-jets as outlined in table 6.6 and illustrated by figure 6.5. Events with two b-tagged jets are categorised as tight-tight (TT), medium-medium (MM) or loose-loose (LL). A b-tagged jet is exclusive to one category, it is placed in the group with most stringent criteria that it passes. Events with only one inclusive b-jet, passing the loose, medium or tight criteria, are labelled as '1T'. Events with no loose b-jets are labelled as '0T'. Furthermore 3-jet events where all three jets pass the loose b-tagging criteria are rejected. An overview of the jet categories is given in table 6.5.

Signal Jets	Forward Jets	b-tag Category
2	0	TT
		MM
		LL
		1T
		0T
Total = 3		TT
		MM
		LL
		1T
		0T

TABLE 6.5: An overview of the different jet categories used within the analysis.

Category	b-jet Efficiency (%)	c-jet RF	l-jet RF	τ-jet RF
loose (L)	79.85	3.04	29.12	6.40
medium (M)	70.00	5.34	135.76	14.90
tight (T)	49.99	26.22	1388.28	120.33

TABLE 6.6: An overview of the different b-jet categories used within the analysis selected by the MV1c b-tagging algorithm. Associated b-jet efficiency and c, l and τ rejection factors, RF, (1/efficiency) are taken from di-leptonic $t\bar{t}$ events with a p_t threshold of 20 GeV, given in [84].

6.3.4.1 3-Jet Study

When defining the 3-jet category studies were undertaken to determine the optimal selection criteria. This section outlines one such study performed by the author. In the published analyses [71, 72, 74] events where the two highest p_T jets, in a 3-jet event, did not pass the inclusive b-tagging criteria were rejected. A simple MC study is presented investigating the effect of keeping all 3-jet events where any two jets pass the inclusive b-tagging requirements. In this study m_{bb} distributions, reconstructed using the two b-tagged jets, are compared by calculating the significance of signal over background events. The calculated significance takes into account the shape of the distribution by calculating the bin by bin significance and adding in quadrature:

$$\text{significance} = \sqrt{\sum_{bins} \frac{n^2_{\text{Signal}}}{n_{\text{Background}}}} \tag{6.10}$$

Events were selected inclusive of b-tagging category based on the selection criteria outlined in previous sections. Figure 6.6 shows the m_{bb} distribution where the two b-tagged jets are also required to be the two leading p_T jets, here on known as sample A. Figure

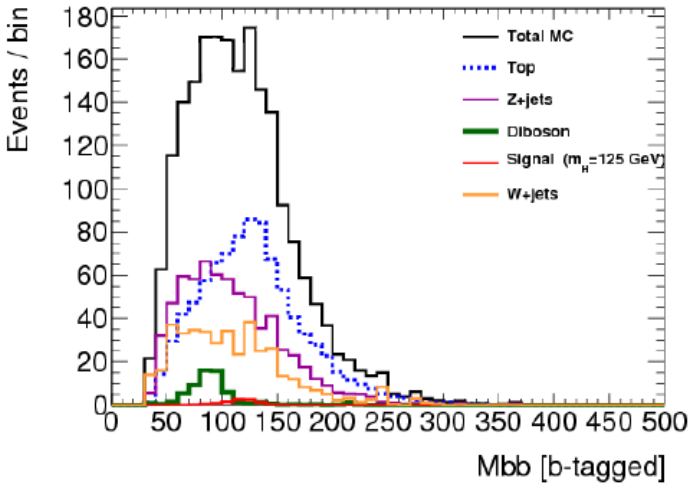

FIGURE 6.6: m_{bb} distribution when the two b-tagged jets are also required to be the two leading p_T jets

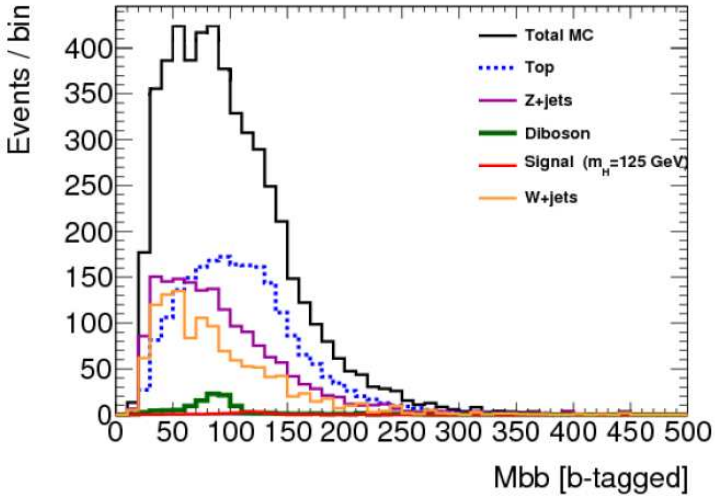

FIGURE 6.7: m_{bb} distribution when all 3-jet events containing exactly 2 b-tagged jets are kept.

6.7 shows the m_{bb} distribution where all 3-jet events containing exactly 2 b-tagged jets are kept, sample B.

Table 6.7 summarises the amount of background and signal MC present in each sample. Although sample A rejects more background events, it does so at the cost of signal events. It is also apparent comparing figure 6.6 and 6.7 that the shape of the total background is different. In sample A contributions from background processes result in a peak near to the simulated Higgs mass of 125 GeV, where as in sample B the peak

E_T^{miss} (GeV)	Signal Events		Background Events		Significance	
	A	B	A	B	A	B
90 - 120	2.3	3.3	879.7	2154.7	0.087	0.109
120 - 160	3.6	5.1	785.1	2067.5	0.124	0.159
160 - 200	2.0	2.8	214.0	631.6	0.130	0.161
200+	2.8	4.0	162.4	455.39	0.227	0.282
Inclusive	10.8	15.3	2040.1	5125.3	0.249	0.314

TABLE 6.7: Comparison of signal and background event yields and significance for 3-jet jet events. Sample A rejects events where the two b-tagged jets are not also the leading p_T jets. Sample B is inclusive of any 3-jet events with exactly two b-tagged jets.

is shifted to a lower value of m_{bb}. This shift improves the overall significance due to increased contributions in the signal region. Table 6.7 also compares the significance of the two samples for a range of E_T^{miss}. The inclusive E_T^{miss} shows an increase in significance of $\sim 26\%$ between sample A and B, similar improvements can be seen in all of the E_T^{miss} bins. It was concluded that 3-jet events should contain exactly two jets which pass the inclusive b-tagging criteria independent of their rank in p_T.

6.3.4.2 Truth Tagging

The MV1c b-tagging algorithm provides powerful discrimination against non-b-jets. It is therefore difficult to produce enough MC to provide a large enough sample of events with the requirement of two reconstructed b-tagged jets when there is no true b-jet. Truth tagging is used to increase the MC statistics in the $W/Z+$ jets backgrounds.

The method uses distributions of the tagging efficiencies above the loose operating point for each background, the distributions are parameterised as a function of jet flavour, p_T and η. For each jet a random efficiency is sampled from the distribution and the corresponding MV1c output weight is assigned. Instead of applying a selection cut on the b-tag weight events are weighted by the efficiency of the jet passing the loose operating point.

This method is only utilised for events where there is no truth b-jet matched to either of the reconstructed jets. In the case where one of the reconstructed jets has a truth jet matched to it the original weight of each jet is cut on. More information on the truth tagging procedure can be found in [84].

6.3.5 Kinematic Selection

Once events have passed the preselection and have been split into the different jet categories, further kinematic selection is applied to increase the signal over background ratio. Kinematic selection achieves this by taking advantage of the differences between the signal and SM backgrounds in a variety of distributions.

The definition of the physics objects used in the following selection cuts has already been described in section 4 and unless otherwise stated will follow the outlined conventions. Throughout this section the reconstructed Higgs boson is denoted by H and is always constructed from the vectoral sum of the two b-tagged jets in the event.

It has already been shown that the E_T^{miss} triggers used in this analysis are not 100% efficient at $E_T^{\text{miss}} < 120$ GeV (see section 6.3.2). Analysis of the trigger turn on region is difficult, therefore events with $E_T^{\text{miss}} < 120$ GeV are rejected from the multivariate (MVA) analysis. Work has been undertaken to understand this low E_T^{miss} region of the analysis. Although the author did not contribute to these studies, inputs from this region are used in the final result. An explanation of the treatment of low E_T^{miss} events can be found in [84].

In previous iterations of this analysis a cut-based approach was used [72, 73] where selection cuts were placed on various distributions in order to maximise signal over background in the final di-jet mass distribution, which was used as the discriminant. In the MVA analysis many of the selection criteria have been loosened or dropped. Some further kinematic selection is, however, undertaken. Table 6.8 summarises the analysis event selection.

Variable	Jet Category	
	2-jet	3-jet
E_T^{miss}	> 120 GeV	> 120 GeV
p_T^{miss}	> 30 GeV	> 30 GeV
$\Delta R(j_1, j_2)$	> 0.7 ($E_T^{\text{miss}} < 200$ GeV)	> 0.7 ($E_T^{\text{miss}} < 200$ GeV)
$\Delta\phi(E_T^{\text{miss}}, p_T^{\text{miss}})$	$< \frac{\pi}{2}$	$< \frac{\pi}{2}$
$\Delta\phi(E_T^{\text{miss}}, \text{jets})$	> 1.5	> 1.5
$\sum_i p_T^{jet_i}$	> 120 GeV	> 150 GeV

TABLE 6.8: A summary of the kinematic event selection for the MVA analysis.

Events selected for the MVA analysis must have $E_T^{\text{miss}} > 120$ GeV, as well as $p_T^{\text{miss}} > 30$ GeV to remove events which contain fake E_T^{miss}. Selection cuts on the angular separation between the two signal jets, $\Delta R(j_1, j_2)$, helps reduce the vector boson + jets background. Further topological cuts help to significantly reduce the multi-jet background; the azimuthal angle between E_T^{miss} and p_T^{miss}, $\Delta\phi(E_T^{\text{miss}}, p_T^{\text{miss}}) < \pi/2$, ensures

the E_T^{miss} measured in the tracker and calorimeter are measured in the same direction; the azimuthal angle between E_T^{miss} and any jet, $\Delta\phi(E_T^{\text{miss}}, \text{jets}) > 1.5$, to ensure the dijet-pair and E_T^{miss} are back to back. Finally the scalar sum of the jet transverse momenta, $\sum_i p_T^{jet_i}$, must reach a minimum value which is dependant on jet multiplicity.

6.4 Multijet Background

Multijet processes have an extremely large cross section resulting in final states containing jets. Searches for $H \rightarrow b\bar{b}$ in associated production channels suffer from large multijet backgrounds.

Rare instrumental effects in the high cross section multijet processes make simulation difficult and CPU intensive. For example jets in multijet backgrounds can be mistagged as leptons and photons and fluctuations in jet energy measurements results in fake E_T^{miss}. Although the cross section of multijet processes is considerably lower at high E_T^{miss} it is still large compared to the Higgs production cross section. Data driven estimates are, therefore, necessary.

In this analysis a so-called 'ABCD' method is used to estimate the multijet contribution to the various signal regions. A two-dimensional plane is constructed using two weakly correlated variables; $\Delta\phi(E_T^{\text{miss}}, p_T^{\text{miss}})$, the azimuthal separation between E_T^{miss} and p_T^{miss} and $\Delta\phi(E_T^{\text{miss}}, jet)$, the minimum azimuthal separation between E_T^{miss} and any jet within an event. An illustration of this can be seen in figure 6.8.

These two variables were chosen such that the multijet background has a different shape from the electroweak background and signal. The signal region must contain real E_T^{miss} from the neutrinos, in this case one would expect the E_T^{miss}, measured in the calorimeter, and p_T^{miss}, measured in the tracker, to point in the same direction. Fake E_T^{miss} produced by fluctuations in jet energy measurements can be identified if the E_T^{miss} lies close to a jet. A signal region can therefore be defined by a high value of $\Delta\phi(E_T^{\text{miss}}, jet)$ and a low value of $\Delta\phi(E_T^{\text{miss}}, p_T^{\text{miss}})$. By studying MC the optimal selection cuts were obtained for the different regions. Regions B and D, and A and C are separated by $\Delta\phi(E_T^{\text{miss}}, p_T^{\text{miss}}) = \pi/2$, regions B and D cover the range $0 < \Delta\phi(E_T^{\text{miss}}, jet) < 0.4$, A and C cover $\Delta\phi(E_T^{\text{miss}}, jet) > 1.5$.

The multijet background shape is taken from region C, where there is a large multijet contribution, by subtracting the total non-multijet MC background from data. This shape can then be normalised into region A, the signal region, by taking the ratio of multijet events in region B to D:

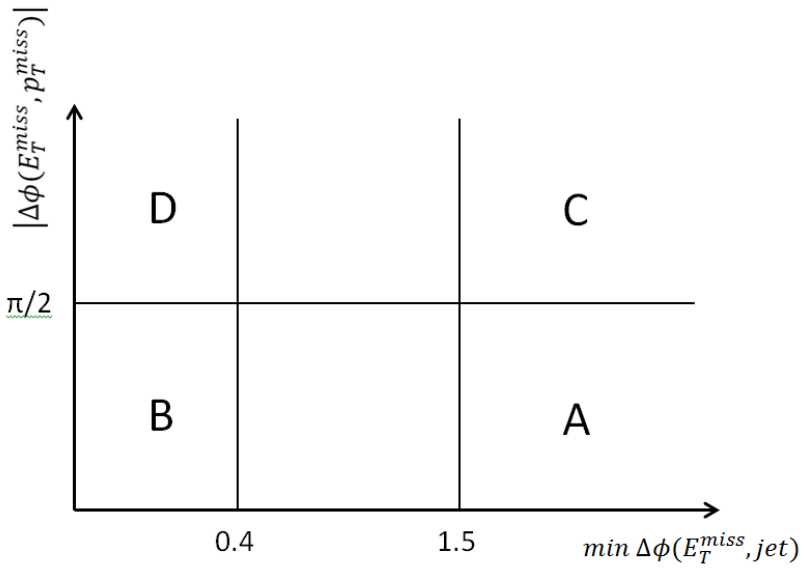

FIGURE 6.8: An illustration of the 2-dimensional plane used to estimate the multijet contribution to signal region A.

$$N_{\text{multijet}}(A) = \frac{N(B)}{N(D)} \times N(C). \tag{6.11}$$

In order to reduce statistical fluctuations caused by low statistics, b-tagging restrictions are dropped in regions B, C and D. A normalisation factor, $R_{B(D)}$ is calculated as the probability of an event in region B (or D) passing the b-tagging requirements of that category. Equation 6.12 then becomes:

$$N_{multijet}(A) = \frac{N(B)}{N(D)} \times N(C) \times R_B. \tag{6.12}$$

Templates of the multijet background are produced for 2- and 3-jets in the LL, MM, TT, 1 tag and 2 tag categories. A summary of the number of events found in each can be seen in table 6.9. In total the multijet background amounts to less than 1 % of the total background.

6.5 Multivariate Analysis Technique

A MVA can be used to increase the sensitivity of an analysis beyond the reach of traditional techniques which use a signal discriminant to separate signal from background. The analysis presented here uses a Boosted Decision Tree (BDT) [85] which naturally builds upon earlier iterations where a single discriminant, the dijet mass, was used

Jets	b-tag Region	MJ Events	EW Events	MJ/EW (%)
2	LL	35.87	3843.39	0.93
	MM	24.98	1719.60	1.45
	TT	13.69	1164.54	1.18
	1 tag	354.91	79057.18	0.45
	0 tag	290.97	436017.45	0.07
3	LL	8.17	1688.90	0.43
	MM	14.97	2457.31	0.61
	TT	21.21	4923.94	0.48
	1 tag	99.79	54252.56	0.23
	0 tag	126.80	193637.38	0.05

TABLE 6.9: Summary of the number of multijet, MJ, events found in each category of the analysis. As well as the total electroweak, EW, background events.

[71–73]. The BDT uses many variables to take advantage of kinematic and topological features of the selected events, as well as b-tagging information to provide a better separation of signal and background.

A decision tree is a natural progression from the dijet mass analysis as at each stage of the algorithm variables are split by a selection cut, see figure 6.9 [85]. Starting with a root node containing a pre-selected training sample of signal and background events input variables are tested one by one to determine which delivers the best separation. Each input variable is tested at a defined number of points in order to determine its optimal selection cut. In this analysis the training sample used is defined by the selection outlined in section 6.3. If separation has increased the root node is split into two daughter nodes using the optimal selection cut. This process is repeated on each daughter node until some 'stop' criteria is met. The resultant nodes are are called leaf nodes and labelled as signal, s, or background, b, depending on their purity.

At each node the BDT checks to see if separation of s and b has increased using the Gini-index [85]

$$\mathcal{G} = p(1-p), \tag{6.13}$$

where p is the purity of the sample given by

$$p = \frac{s}{s+b}. \tag{6.14}$$

If the sum of $\mathcal{G}$ for the two daughter nodes, after being weighted to the same number of events, is less than $\mathcal{G}$ of the parent node then separation has increased.

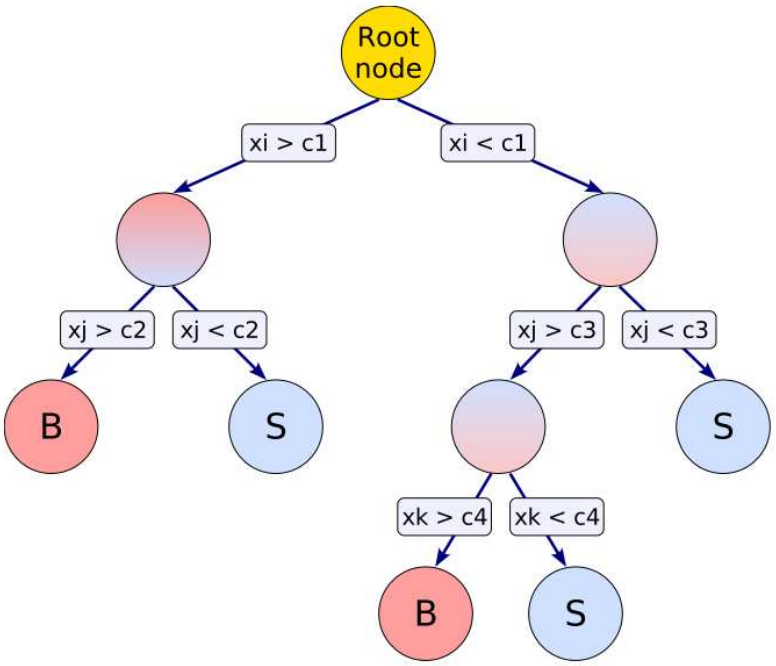

FIGURE 6.9: A schematic representation of a simple decision tree, x_i, j, k represent the selection cuts on input variables [85].

BDTs are susceptible to instabilities caused by poor statistics in the training sample. Take, for example, the case where two input variables are of a similar discriminating power. The BDT algorithm selects one variable to cut on, however, the apparent separation was caused by a fluctuation. This decision then changes the structure of the BDT in later nodes possibly leading to a substantially different result. This problem can be overcome by constructing many decision trees (a forest) from the same training sample. A technique known as 'boosting' reweights the training sample in each of the trees and takes a weighted average to produce the final discriminant.

In this analysis adaptive boost (AdaBoost) is used [85]. AdaBoost constructs the first tree using the nominal training sample, following trees are first re-weighted by a common weight, α, given by

$$\alpha = \frac{1 - err}{err}, \tag{6.15}$$

where err is the rate of misclassification in the leaf nodes of the previous tree i.e. the rate that s is incorrectly classified as b or visa-versa. The rate of misclassification is defined by the purity of the node. Signal nodes should have a purity > 0.5 and background nodes should have a purity of < 0.5. The weights are then renormalised ensuring the sum of the weights of the entire sample remains constant.

6.5.1 Analysis Training

The analysis trains BDTs for 2-tag events with $E_T^{\text{miss}} > 120$ GeV; LL, MM and TT events are combined in the training. Separate BDTs are trained for the 2- and 3-jet categories. The 2-jet region is more sensitive therefore training separate BDTs for 2- and 3-jet events allows the analysis to gain sensitivity, furthermore extra variables are used to maximise the sensitivity of the 3-jet catagory.

In order to maximise statistics and use all of the selected events in an unbiased manner two BDTs are trained for each category. Half the events, sample A (B), from the training sample are used for training the BDT, the performance of the BDT is then evaluated using the other events from sample B (A). In data a random choice is made to determine which sample the event is added to. After being evaluated the two samples are summed together.

Input variables were selected based up on their separating power. Starting with m_{bb} variables were added to the BDT one by one to ensure that they increased overall separation. Table 6.10 outlines the MVA input variables used in this analysis. Figures 6.10 and 6.11 show the input variables split into signal and background for the 2- and 3-jet selections respectively.

Input Variable	2-jet	3-jet
$E_{\text{T}}^{\text{miss}}$	✓	✓
$p_{\text{T}}^{b_1}$	✓	✓
$p_{\text{T}}^{b_2}$	✓	✓
m_{bb}	✓	✓
$\Delta R(b_1, b_2)$	✓	✓
$\lvert\Delta\eta(b_1, b_2)\rvert$	✓	✓
$\Delta\phi(V, bb)$	✓	✓
MV1c($b1$)	✓	✓
MV1c($b2$)	✓	✓
$p_{\text{T}}^{\text{jet}_3}$		✓
m_{bbj}		✓

TABLE 6.10: Input variables used in the analysis for the 2- and 3- jet MVA.

The BDT output for 2- and 3- jet training samples can be seen in figures 6.12 (a) and (b) respectively, again split in to background and signal.

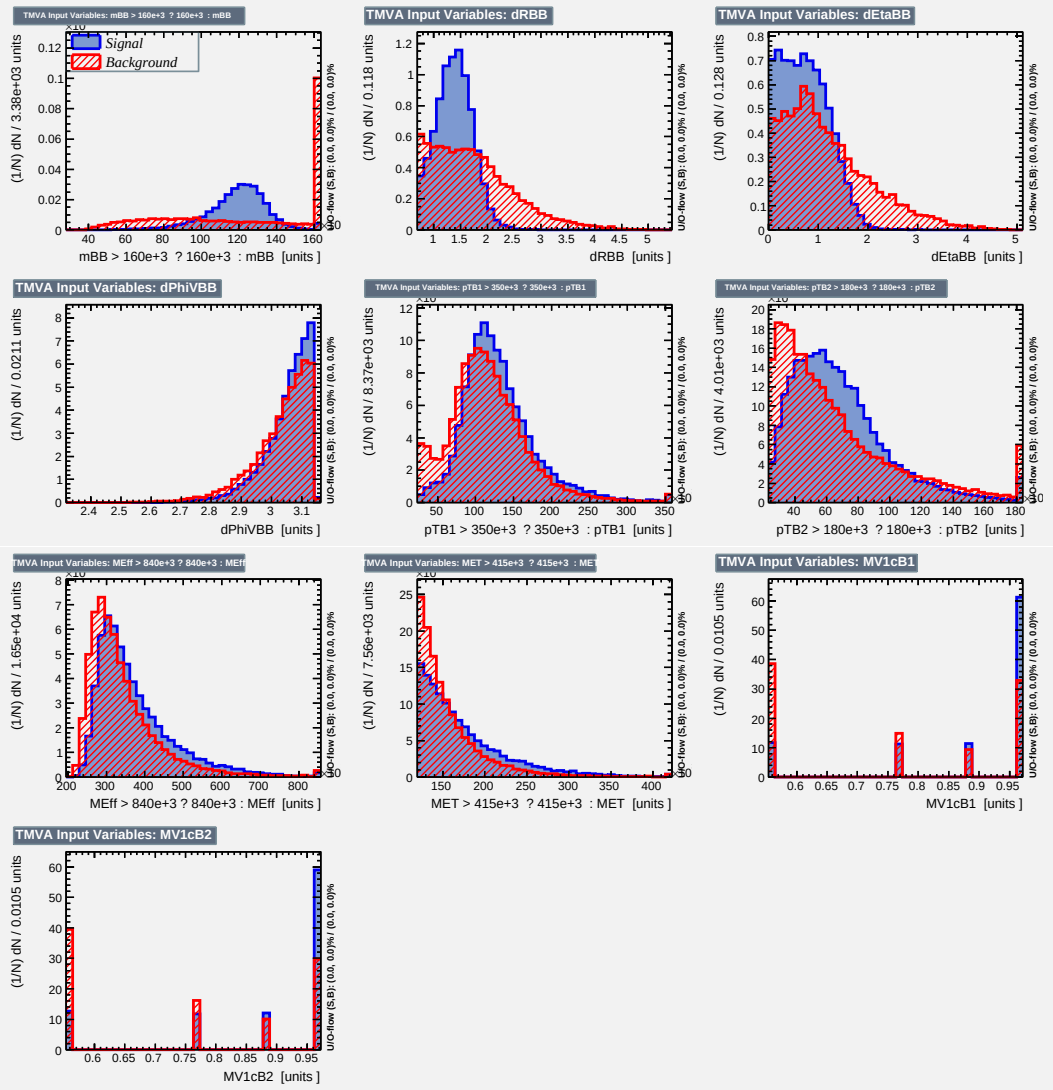

FIGURE 6.10: BDT input variables split into signal (blue) and background (red) for 2-jet selection.

6.6 Systematic Uncertainties

This section will give an overview of the systematic uncertainties used within the analysis. Experimental systematic uncertainties take into consideration the corrections to the efficiency and/or calibration of simulated physics objects, the modelling of the various background and signal processes, along with uncertainties associated to the data such as luminosity, triggering and the data driven determination of the multijet background. Many of the uncertainties discussed are provided by independant ATLAS analyses or are the result of independant stuides by the VH analysis group. A more detailed explaination of the uncertainties can be found in [84] or, when relevant, by following the citations given for each study.

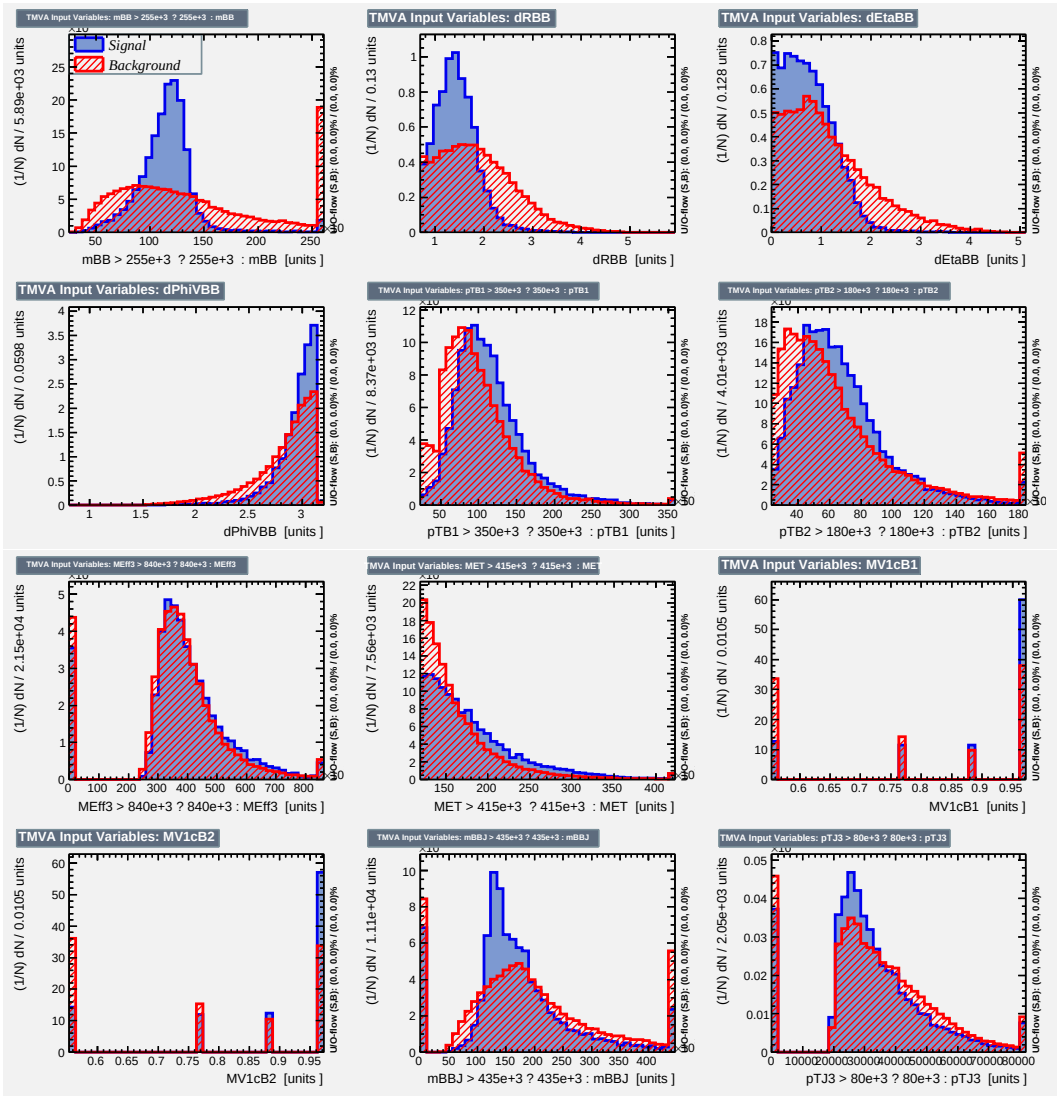

FIGURE 6.11: BDT input variables split into signal (blue) and background (red) for 2-jet selection.

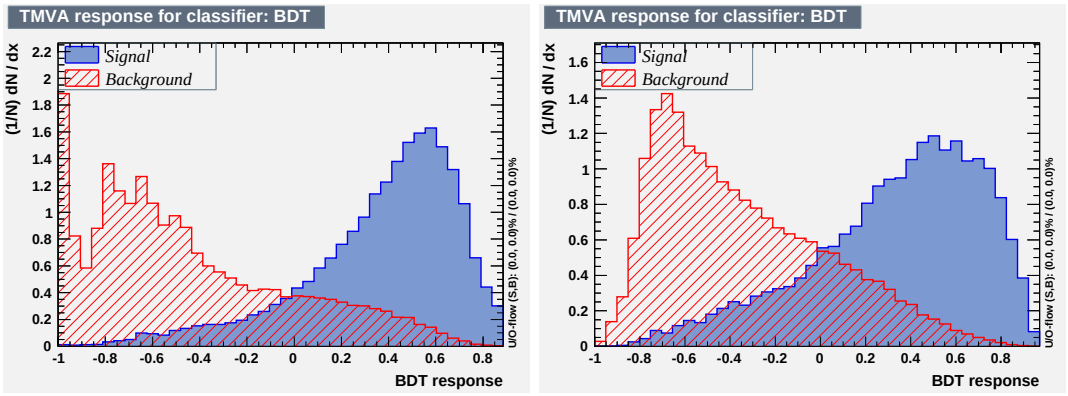

(a) (b)

FIGURE 6.12: BDT output split into signal (blue) and background (red) for (a) 2-jet and (b) 3-jet training.

6.6.1 Uncertainties Associated with Physics Objects

The uncertainties associated with physics objects are generally provided by independant analyses which provide ATLAS wide prescriptions. The following section will outline the uncertainties and the method by which they are applied to the analysis.

6.6.1.1 Leptons

The uncertainties on lepton efficiciency in 0-lepton events have already been discussed in some detail in section 6.3.3.1. The two orthogonal analyses, 1- and 2-lepton, have their own associated lepton uncertainties which take into account the electon and muon triggers [86, 87], isolation efficiency, energy measurment and resolution [88, 89]. The impact of these uncertainties is very small, generally less than 1%.

Lepton energy and resolution uncertainties are estimated by shifting lepton energies up and down and then in each case reselecting events [88, 89].

The electron and muon isolation efficiencies are applied using scale factors derived through a tag-and-probe method. Efficiencies are calculated as a function of p_T and $|\eta|$ in both data and MC. The MC efficiency is then corrected to data by applying the calculated scale factor. Further detail can be found in [84].

6.6.1.2 Jets

Jets carry several sources of systematic uncertainty applied to the jet energy scale (JES), jet energy resoultion (JER) and the jet vertex fraction (JVF).

In total there are 56 uncertainties associated with the JES [90], a detailed discussion of which can be found in [91]. The uncertainties are provided as uncorrelated components and can therefore be treated as independant sources of uncertainty in the analysis. Contributions to the total JES uncertainty come from the various in-situ calibration analyses, η-dependent modelling, behaviour of high-p_T jets, pile-up and jet flavour response.

In total the combined systematic uncertainty from JES ranges from $\approx 3\%$ for jets with $p_T = 20$ GeV to $\approx 1\%$ for jets with $p_T = 1$ TeV. A summary of the JES uncertainty used in this analysis as a function of p_T and η can be seen in figures 6.13 (a) and 6.13 (b) respectively.

Further uncertainties, determined from MC studies, are applied to the b-jet energy scale [90]. The uncertainty of the calorimeter response is measured by comparing the single

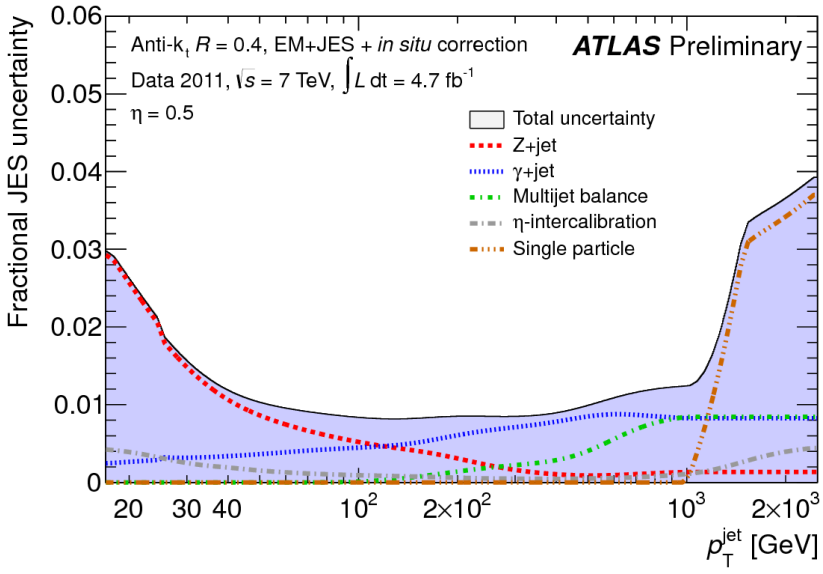

(a)

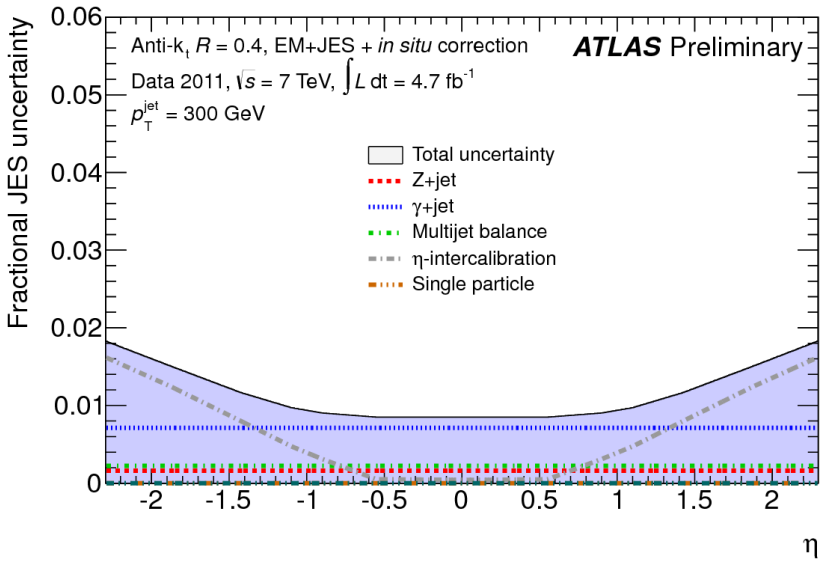

(b)

FIGURE 6.13: Fractional JES uncertainty as a function of jet (a) p_T and (b) η for anti-kt jets with a distance parameter of R = 0.4 [47].

hadron response measurement [92] in different MC simulations. Uncertainties range from 1.5% to 3.0% and are applied in addition to the previously described JES uncertainties.

The JER has two components contributing to the total uncertainty [93], one for all jets and a one specifically for b-jets [94]. In each case uncertainties were determined by MC to data resolution comparisons. The impact of these systematic uncertainties was then measured on the analysis by smearing the jet p_T spectrum by a Gaussian, centred on 1, with a width equal to the true resolution plus the relative uncertainty. In total the combined systematic uncertainty from JER ranges from $\approx 10 - 20\%$ for jets with $p_T = 20$ GeV, depending on η_{jet} to $< 5\%$ for jets with $p_T > 200$ GeV.

6.6.1.3 Missing Transverse Energy

The systematic uncertainty associated to E_T^{miss} is based upon the energy calibration and resolution of energy clusters within the calorimeter which have not already been associated with another physical object as defined in 4. Systematic variations of other physical objects are all propagated through the E_T^{miss} calculation. In total an uncertainty of $\approx 8\%$ comes from the E_T^{miss} energy calibration and $\approx 2.5\%$ from the resolution [95].

6.6.1.4 Flavour Tagging

The systematic uncertainties associated to flavour tagging using the MV1c algorithm are provided through p_T and MV1c output dependant scale factors which correct the measured MC efficiency to data [96]. Each scale factor carries an uncertainty which takes into account the associated experimental, theoretical and statistical uncertainties. Scale factors are provided for b-, c- and light-flavour jets.

6.6.2 Uncertainties Associated with Signal and Background Modelling

The 0-lepton analysis presented here and the 1- and 2-lepton associated production channels are complimentary analyses which share modelling systematics. The wide phase space of the three analyses allows for detailed studies of the different backgrounds. Associated systematic uncertainties have been studied in detail by the analysis group [74]. This section will outline the treatment of these systematics, more detail can be found in [74, 84].

In general, uncertainties have been assessed focusing on the quantities used in the limit-extraction fit, see section 6.7, and those which are input into the BDT, see section 6.5. Where possible, dedicated control regions are used, dominated by the background in

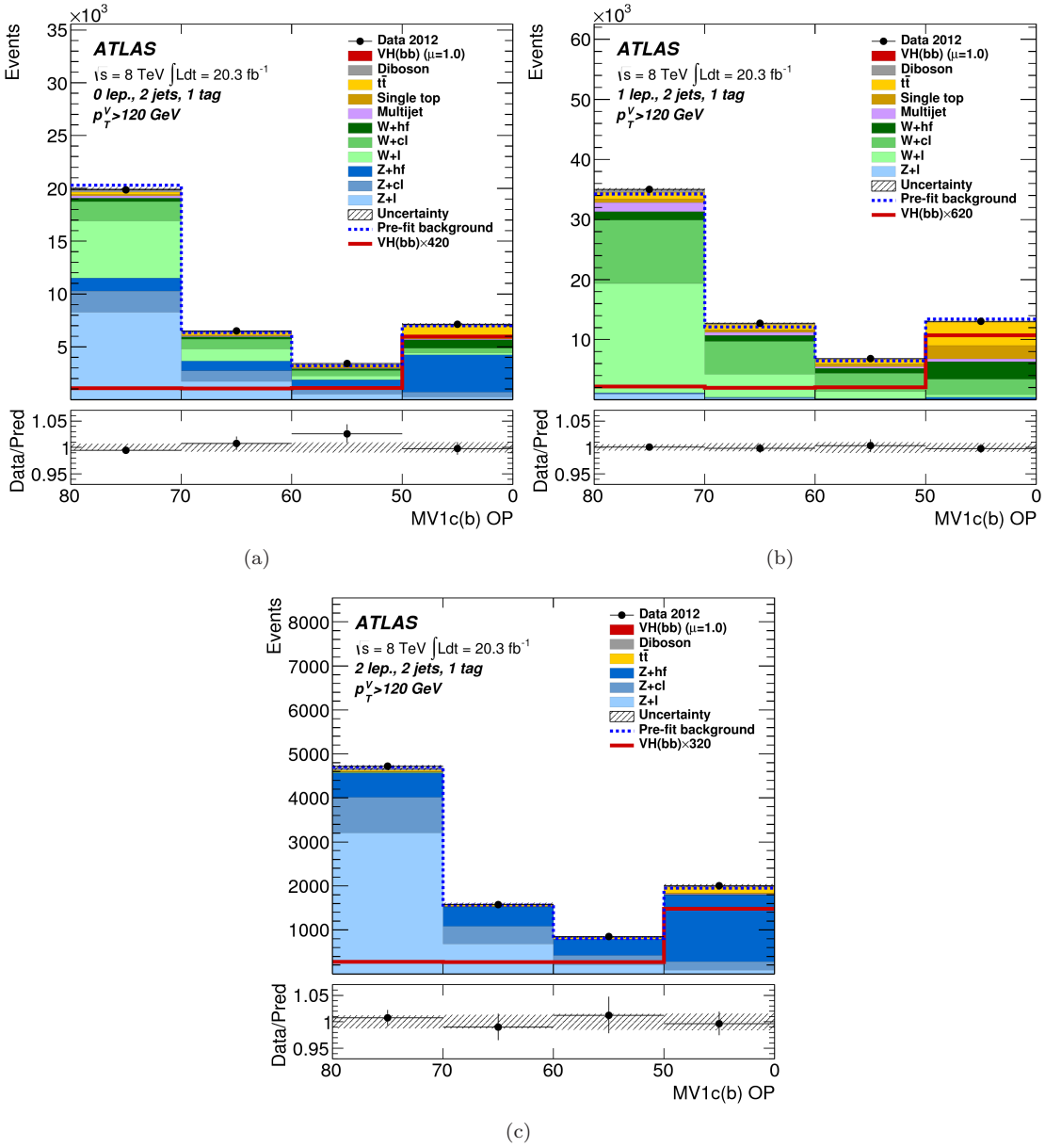

FIGURE 6.14: Distributions of the MV1c b-tagging algorithm output for the 1-tag control regions for (a) 0-, (b) 1- and (c) 2-lepton analyses used to constrain the $Z/W+$ jets backgrounds [74].

question, to directly compare data to MC simulation. W and $Z+$ jets and $t\bar{t}$ backgrounds are studied in this way, figure 6.14 gives an example of the 1-tag control regions used to constrain the $Z/W+$ jets background in the fit. The multijet background is estimated using a data driven method, see sec 6.4. Section 6.6.2.1 discusses the systematic uncertainty applied to this background.

Other MC backgrounds can be studied by comparing distributions produced by a variety of MC generators to the nominal generator used for each background, see table 6.2 for a list of nominal generators. When comparing generators each variable is considered

individually for each background. The variable which has the largest discrepancy for any studied generator to the nominal provides the uncertainty. This uncertainty is then symmeterised and propagated through into the BDT distribution. If the uncertainty covers variations from other generators the systematic is sufficient otherwise the variable which causes the next most discrepancy is considered in addition and the process is repeated until the systematic uncertainty covers all generator variations.

Modeling studies showed that the in some cases the MC shape was different to that which was measured in data [74, 84]. Additional systematic uncertainties are applied: The $t\bar{t}$ top-quark p_T distribution is reweighted at generator level [97] and a systematic uncertainty is applied as half the shifted value. The $\Delta\Phi(j_1, j_2)$ distribution is reweighted for $Z + ll$, $W + ll$ and $W + cl$ components and again a systematic uncertainty of half the shifted value is applied. For all other Z/W+jets components the distrbution is not corrected for, instead a systematic uncertainty covers the full correction. A correction to p_Z^T is applied to the Z+jets background.

Table 6.11 [74] outlines the overall uncertainty applied to the various backgrounds used in the presented analysis.

Signal sample cross sections and branching ratios carry an associated uncertainty [98, 99] from the choice of scale and PDF. Further shape and accpetance uncertainties, after kinematic selection, also arise from this choice. These uncertainties are estimated following the procedure outlined in [100] and [101]. A summary of the signal modelling systematic uncertainties is given in 6.12 [74].

Cross section scale and PDF uncertainties are taken from the CERN yellow report [102], see table 6.13. Uncertainties are higher for the gg process due to one-loop induced sub-processes shown in figure 6.15 [103]. An additional factor is taken into account for the ratio of 2- and 3-jet events.

QCD scale acceptance and p_T^V shape uncertainties are measured by comparing different signal MC produced with varying renormalisation and factorisation scales MC produced with the nominal values, as prescribed in [104]. Acceptance uncertainties due to the choice of PDF are estimated using a similar method prescribed by [105], however, this time PDF uncertainty is varied.

6.6.2.1 Multijet

The multijet background is determined through a data driven method, see sec 6.4. In total it accounts for $< 1\%$ of the total background. Two methods were used to estimate the uncertainty associated with the measurement

Z+jets	
Zl normalisation, 3/2-jet ratio	5%
Zcl 3/2-jet ratio	26%
$Z+$ hf 3/2-jet ratio	20%
$Z+$ hf/Zbb ratio	12%
$\Delta\phi(\mathrm{jet}_1, \mathrm{jet}_2), \mathrm{p_V^T}, \mathrm{m_{bb}}$	Shape only
W+jets	
Wl normalisation, 3/2-jet ratio	10%
Wcl, $W+$ hf 3/2-jet ratio	10%
Wbl/Wbb ratio	35%
Wbc/Wbb, Wcc/Wbb ratio	12%
$\Delta\phi(\mathrm{jet}_1, \mathrm{jet}_2), \mathrm{p_V^T}, \mathrm{m_{bb}}$	Shape only
$t\bar{t}$	
3/2-jet ratio	20%
High/low $p_{\mathrm{T}}^{\mathrm{V}}$ ratio	7.5%
Top quark $p_{\mathrm{T}}, m_{bb}, E_{\mathrm{T}}^{\mathrm{miss}}$	Shape only
Single top	
Cross section	4% (s-, t-channel), 7% (Wt)
Acceptance (generator)	3%-52%
$m_{bb}, p_{\mathrm{T}^{\mathrm{b}_2}}$	Shape only
Diboson	
Cross section and acceptance (scale)	3%-29%
Cross section and acceptance (PDF)	2%-4%
m_{bb}	Shape only

TABLE 6.11: A summary of the background modelling systematics used within the presented analysis taken from [74].

Signal	
Cross section (scale)	1% ($q\bar{q}$), 50% (gg)
Cross section (PDF)	2.4% ($q\bar{q}$), 17% (gg)
Branching ratio	3.3%
Acceptance	1.5% – 3.3%
3-jet acceptance (scale)	3.3% – 4.2%
p_{T}^{V} shape (scale)	Shape only
Acceptance (PDF)	2% – 5%
p_{T}^{V} shape (NLO EW correction)	Shape only
Acceptance (parton shower)	8% – 13%

TABLE 6.12: A summary of the signal modelling systematics used within the presented analysis taken from [74].

- Vary the upper and lower $\Delta\phi(E_T^{\mathrm{miss}}, jet)$ selection which define the different regions, see figure 6.8. This test ensured that the predicted number of multijet events is not sensitive, within the systematic uncertainty, to the number of MC events used in the method.

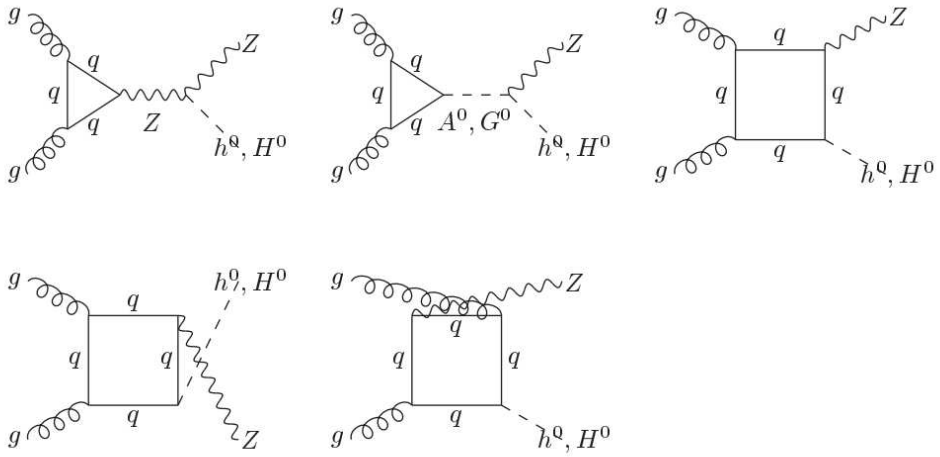

FIGURE 6.15: Feynman diagrams for the one-loop induced $gg \to ZH$ sub-processes.

m_H GeV	$qq \to ZH$			$gg \to ZH$		
	σ (pb)	Scale (%)	PDF (%)	σ (fb)	Scale (%)	PDF (%)
115	0.4995	$\pm$1.0	$\pm$2.3	36.34	$\pm$50.0	$\pm$19.0
120	0.4366	$\pm$1.0	$\pm$2.5	34.39	$\pm$50.0	$\pm$12.8
125	0.3828	$\pm$1.0	$\pm$2.3	32.46	$\pm$50.0	$\pm$16.9
130	0.3365	$\pm$1.0	$\pm$2.4	30.60	$\pm$50.0	$\pm$14.2
135	0.2971	$\pm$1.0	$\pm$2.5	28.79	$\pm$50.0	$\pm$16.4

TABLE 6.13: Inclusive cross sections and related uncertainties for $qq \to ZH$ and $gg \to ZH$ production at $\sqrt{s} = 8$ TeV. Uncertainties are derived from the CERN yellow report [102].

- Calculate the b-tagging rate using region D rather than B to ensure the different selection of events give an estimate which is consistent within the systematic uncertainty.

As a result of these studies an uncertainty of 100% is placed on the background measurement for each region. The uncertainties are treated as uncorrelated. For more details see [84].

6.7 Statistical Procedure

This section will outline the statistical procedure used to obtain a meaningful result from the analysis. The procedure is based on the CL_s [106] method where results are derived based on the level of agreement between the observed data and either a background only, null, or a background plus signal hypothesis. It is used to extract a signal strength, μ,

defined as the ratio of the measured Higgs boson production cross section times the $H \rightarrow b\bar{b}$ branching ratio relative to the SM value and set exclusion limits on the cross section times branching fraction of $H \rightarrow b\bar{b}$. An introduction to hypothesis testing can be found in section 6.7.1. The application of such methods to this analysis is then discussed in section 6.7.2.

6.7.1 Introduction to Hypothesis Testing

This section attempts to give a generalised introduction to hypothesis testing methods utilised by ATLAS in the search for new physics. Detailed explanations and discussion of these methods can be found in [106] [107].

6.7.1.1 Introduction to the Likelihood Function

It is useful to first consider the simple example of a single histogram of an output variable from an analysis. From this histogram it is possible to measure the expected signal, s_i, and background, b_i, in each bin, as predicted by MC, along with the number of recorded data events d_i.

Next consider two different hypotheses which are defined by the signal strength, μ. The null or background only hypothesis expects no signal to be present in the data; $\mu = 0$. The signal + background hypothesis expects there to be a signal present in the data, on top of the expected background; $\mu = 1$.

Using a likelihood function it is possible to find the value of μ which results in the best overall agreement between the predicted number of signal + background events, p_i, and the actual data yield in each bin. Here p_i is defined as

$$p_i(\mu) = b_i + \mu s_i. \tag{6.16}$$

It is clear that in the null hypothesis there is no predicted signal.

In each bin of the histogram agreement between p_i and d_i can be measured with a Poisson probability term, L_i [106],

$$L_i = \frac{p_i(\mu)^{d_i}}{d_i!} e^{-p_i(\mu)}, \tag{6.17}$$

L_i reaches a maximum when p_i and d_i are equal. The likelihood function, $\mathcal{L}$, is defined as the product of poisson probability terms over all bins,

$$\mathcal{L} = \prod_{i=1}^{N} L_i. \tag{6.18}$$

$\mathcal{L}$ is used to test the overall agreement of p_i and d_i. It reaches a maxiumum for the most likely value of μ. Converting the likelihood to a log likelihood converts the product term to a summation. The log likelihood is easier to handle mathematically and is therefore generally prefered.

6.7.1.2 Nuisance Parameters

In reality such a simplified likelihood model does not work in an analysis such as the one presented in this thesis. It does not take into account all of the information known about the signal and background predictions. In particular it does not account for the associated systematic uncertainties. These uncertainties are incorporated into the statistical model as a set of nusiance parameters (NP).

Each NP is given a range of values which it may take, together the NPs are denoted by θ. In the analysis described here NPs are input in the form of histograms at the nominal and $\pm 1\sigma$ level. The histograms can be used to define either shape or normalisation uncertainties. The likelihood function can then vary each NP along with μ in order to find a maxiumum. Equation 6.19 is explicitly written as

$$\mathcal{L}(\mu, \theta) = \prod_{i=1}^{N} \frac{(b_i(\theta) + \mu s_i(\theta))^{d_i}}{d_i!} e^{-b_i(\theta)+\mu s_i(\theta)}. \tag{6.19}$$

6.7.1.3 Control Bins

It is sometimes possible to take additional measurements from control regions in order to constrain a certain NP. For example normalisation of backgrounds can be constrained if there is sufficient statistical power in the data. An additional term is added to the likelihood function taken from a control histogram in a region dominated by a particular background,

$$\mathcal{L}(\mu, \theta) = \prod_{i=1}^{N} \frac{(b_i(\theta) + \mu s_i(\theta))^{d_i}}{d_i!} e^{-b_i(\theta)+\mu s_i(\theta)} \prod_{j=1}^{N} \frac{b_j(\theta)^{d_j}}{d_j!} e^{-b_j(\theta)}, \tag{6.20}$$

where the control histograms are denoted by j.

6.7.1.4 Profile Likelihood Ratio

A profile likelihood ratio is used to test a hypothesised value of μ [106],

$$\lambda(\mu) = \frac{\mathcal{L}(\mu, \hat{\hat{\theta}})}{\mathcal{L}(\hat{\mu}, \hat{\theta})}, \tag{6.21}$$

where $\hat{\hat{\theta}}$ is the set of values for θ which maximise $\mathcal{L}$ for a given hypothesised value of μ and $\hat{\theta}$ and $\hat{\mu}$ are the set of values which give the absolute maximum value of $\mathcal{L}$. $\mathcal{L}(\mu, \hat{\hat{\theta}})$ is known as the conditional maximum-likelihood function and $\mathcal{L}(\hat{\mu}, \hat{\theta})$ the maximised unconditional likelihood function.

In reality many physics analyses contain more than one channel. It is possible to combine these as a product into the profile likelihood ratio [108]

$$\lambda(\mu)_{\text{multi-region}} = \prod_{j=1}^{N_{\text{channels}}} \lambda(\mu) \tag{6.22}$$

6.7.1.5 Statistical Tests

As well as extracting a best fit signal strength, the profile likelihood ratio allows further statistical tests to be carried out giving information on the hypothesis. A test statistic, q_μ, is used [106] to quantify agreement between a proposed hypothesis and the measured data,

$$q_\mu = -2\ln\lambda_\mu. \tag{6.23}$$

The test statistic can be constructed in different ways to provide information about the proposed hypothesis.

An exclusion limit is set on the largest signal strength which is compatible with the measured data. This allows a given hypothesis, e.g. there is a SM Higgs + background in the data, to be excluded to a given confidence level. The test statistic is defined as [106],

$$q_\mu = \begin{cases} -2ln\lambda_\mu & \hat{\mu} \leq \mu, \\ 0 & \hat{\mu} > \mu. \end{cases} \tag{6.24}$$

The test statistic is set to zero when $\hat{\mu} > \mu$ as when setting an upper limit data with $\hat{\mu} > \mu$ does not represent less compatibility with μ than the data obtained and therefore should not be taken as part of the rejection region of the test. This can then be used to calculate a p-value for a hypothesised value of μ given by [106],

$$p_\mu = \int_{q_{\mu,obs}}^{\infty} f(q_\mu|\mu) dq_\mu. \tag{6.25}$$

The p-value quantifies the level of agreement between the measured data and hypothesis. Here $q_{\mu,obs}$ is the observed test statistic and $f(q_\mu|\mu)$ is the function given by the test statistic for a given μ. The value of μ which corresponds to $p_\mu = 0.05$ gives an upper limit to μ at a 95% confidence level.

By assuming the background only hypothesis and setting $\mu = 0$ the background only hypothesis can be tested in a similar way. The test statistic is constructed as,

$$q_0 = \begin{cases} -2ln\lambda_0 & \hat{\mu} \geq 0, \\ 0 & \hat{\mu} < 0. \end{cases} \tag{6.26}$$

The test statistic can be then used to ask what is the probability that the observed signal strength, $\hat{\mu}$, is seen given the background only hypothesis. The data is only considered to show a lack of agreement with the background only hypothesis if an upward fluctuation is seen. Although a downward fluctuation could point to a deviation from the background only hypothesis, the downwards deviation would not be compatible with new signal events. Again a p-value can be calculated to quantify the level of agreement between the measured data and given hypothesis,

$$p_0 = \int_{q_{\hat{\mu}}}^{\infty} f(q_0|0) dq_0. \tag{6.27}$$

Using the calculated p_0 a statistical significance, Z, can be calculated,

$$Z = \phi^{-1}(1 - p_0), \tag{6.28}$$

where ϕ^{-1} is the quantile of the normal distribution. The value of Z shows how many standard deviations the observed signal strength is from the background only hypothesis of $\mu = 0$.

6.7.2 VH Analysis Fit Overview

This section will describe the VH analysis fit which uses information from all three of the VH analysis channels to extract a best fit value of μ. The signal hypothesised is the SM Higgs boson. In the case where results are presented for an individual analysis channel the same method has been used, however, only the relevant analysis regions and NP are input into the fit. The statistical procedure has been developed by the analysis group and is based upon the RooStats framework [109, 110].

Using information from various input histograms produced from the three analyses a binned likelihood function is constructed as the product of Poisson-probability terms, see section 6.7.1. For each bin from each histogram in each analysis region a probability term is calculated based on the number of data events and the expected signal and background events, given by equation 6.17.

In total there are 38 analysis regions based upon the selection outlined in section 6.6; 27 are taken from the 2 b-tag signal regions and 11 from the 1-tag region. Table 6.14 gives an overview. Each of the three analyses provides inputs for two p_T^V regions; $0 < p_T^V < 120$ GeV and $p_T^V > 120$ GeV for the 1- and 2-lepton analyses and $100 < p_T^V < 120$ GeV and $p_T^V > 120$ GeV for the 0-lepton analysis. In the 1-lepton analysis the electron channel is only used in the $p_T^V > 120$ GeV region. Each region is then separated into 2- and 3-jet categories with the exception of the low E_T^{miss} region of the 0-lepton analysis where only 2-jet inputs are provided to the fit. Finally these regions are once again split based on their b-tagging catagory.

The MV1c distribution is used as the discriminant for all of the 11 1T regions included in the fit. The m_{bb} distribution is used for the 3 low E_T^{miss} 2-jet, 2-tag regions of the 0-lepton analysis. The remaining 24 2-tag (LL or MM, TT) regions use the BDT output as a discriminant, see section 6.5. In the 0- and 2- lepton analyses the MM + TT regions are merged together for each jet and p_T^V region [84]. Figures 6.16-6.26 show the distributions which are used in the fit after normalisation. The prefit background distribution is also shown.

The impact of systematic uncertainties, as outlined in section 6.6, on the signal and background expectation is estimated by a set of NPs following the method described in section 6.7. Systematic uncertainties are constrained in the fit by Gaussian probability density functions. Further NPs deal with the normalisation of the various background processes to data. These NP are constrained by log-normal probability density functions to prevent negative normalisation values. The main backgrounds; $t\bar{t}$, Wbb, Wcl, Zbb and Zcl are left to float freely in the fit as the data has sufficient statistical power to constrain them.

		0-lepton ($100 < E_T^{\text{miss}} < 120$)	0-lepton	1-lepton	2-lepton
b-tagging category	1T	MV1c	MV1c	MV1c	MV1c
	LL	m_{bb}	BDT	BDT	BDT
	MM	m_{bb}	BDT	BDT	BDT
	TT	m_{bb}		BDT	

TABLE 6.14: An overview of the distributions used as input to the likelihood fit where BDT is the evaluated boosted decision tree discriminant trained in the given regions. The 1- and 2- lepton channels are further divided into two p_T^V regions ($p_T^V < 120$ GeV and $p_T^V > 120$ GeV). All of the analysis channels are also divided in to 2- and 3- jet regions aside from the low E_T^{miss} region of the 0-lepton analysis which only provides inputs for the 2-jet catagory.

Some of the systematics can have shape variations given by the input histogram templates. Due to limited statistical power in parts of the analysis events migrating in and out of the selection cause fluctuations adding a statistical component to the template which is not a true part of the uncertainty.

In order to account for this a series of smoothing and pruning procedures are applied to the NPs. These procedures first try to remove the fluctuations by merging bins within the nominal templates, then NPs which have a small impact on the analysis and fall below certain criteria are removed from the fit. Full details can be found in [84]. After pruning there are 184 NP entering the fit a table of which can be found in appendix B taken from [84].

It is possible to assess the impact of NP on the signal strength and rank the NP. Figure 6.27 shows the ten highest ranked systematics which cause the biggest impact on the fitted signal strength in the combinend 0-, 1- and 2-lepton (012) fit. To assess the impact of the NP whilst properly accounting for correlations with other NP the fit is performed again with each NP fixed to its post-fit value shifted up and down by its nominal uncertainty, all other NPs are allowed to vary. The amount by which the fitted signal strength is shifted gives a measure of the impact of the considered NP.

Results of the fit are presented through several statistical tests, as outlined in section 6.7. The best fit signal strength $\hat{\mu}$ is obtained by maximising the likelihood function with respect to all parameters. Expected results are obtained using the fitting procedure described by replacing the data with the expectation from simulations and setting all of the NPs to their best fit values.

6.7.3 MVA Training at Different Mass Points

The presented analysis has been optimised for a Higgs boson mass of 125 GeV. Results, however, are shown for a variety of mass points around 125 GeV, see section 6.5. The

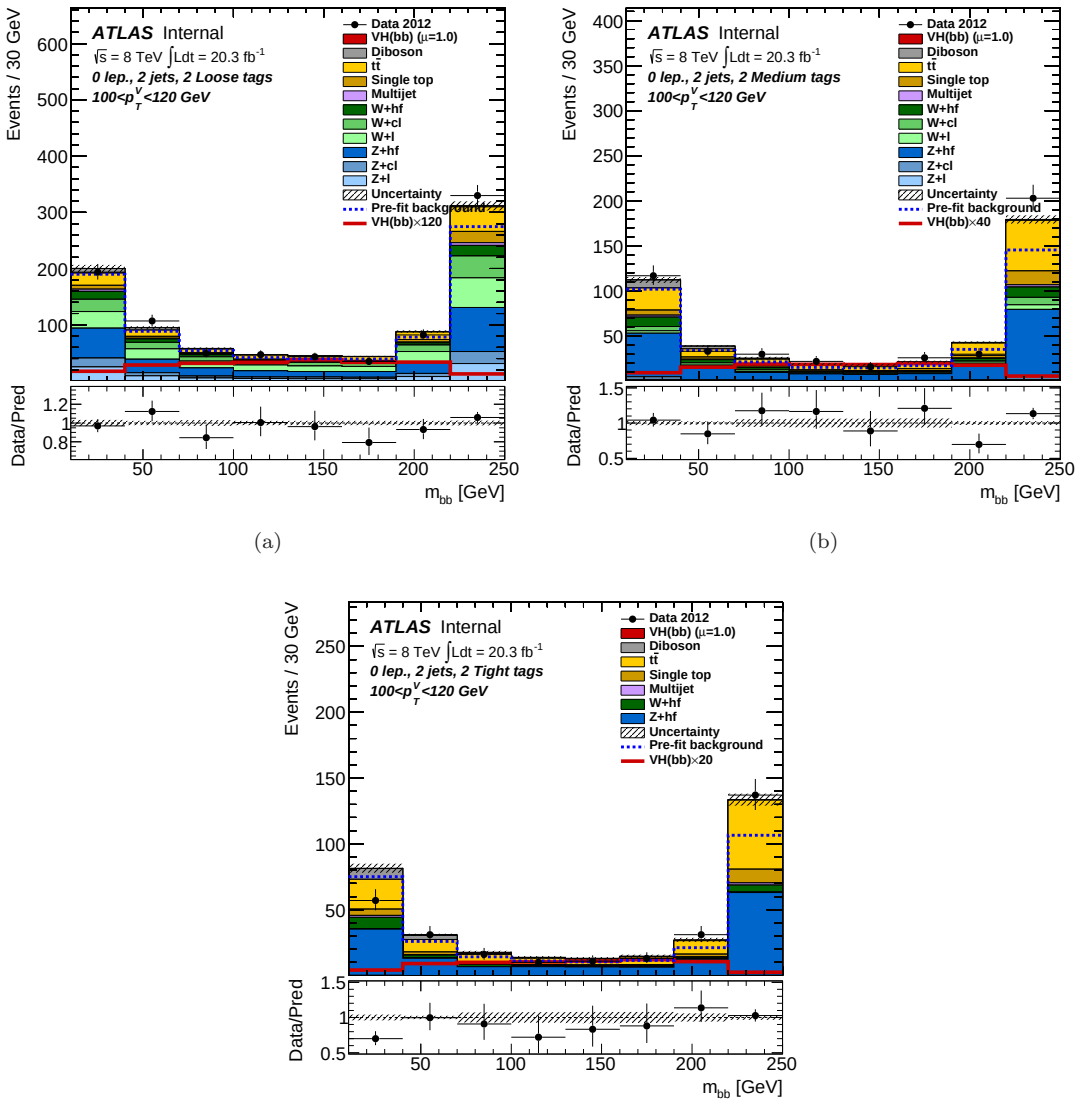

FIGURE 6.16: Post-fit distributions of the dijet mass for the low E_T^{miss} regions of the 0-lepton analysis; (a) LL, (b) MM and (c) TT. The fitted background is shown through the various stacked MC histograms along with the observed data points and expected signal for a 125 GeV SM Higgs boson. The pre-fit background is also shown.

m_{bb} distribution is the most powerful discriminant in the BDT and its performance therefore is reduced at mass points other than 125 GeV. A study was undertaken to show that analysis sensitivity at mass points other than 125 GeV could be improved by training the BDT individually for each mass point.

The simultaneous fit is run using inputs from the 0-lepton analysis for the following mass points: 110, 115, 120, 125, 130, 135 and 140 GeV, for two different training methods.

- (a) The BDT is trained using only the 125 GeV signal sample

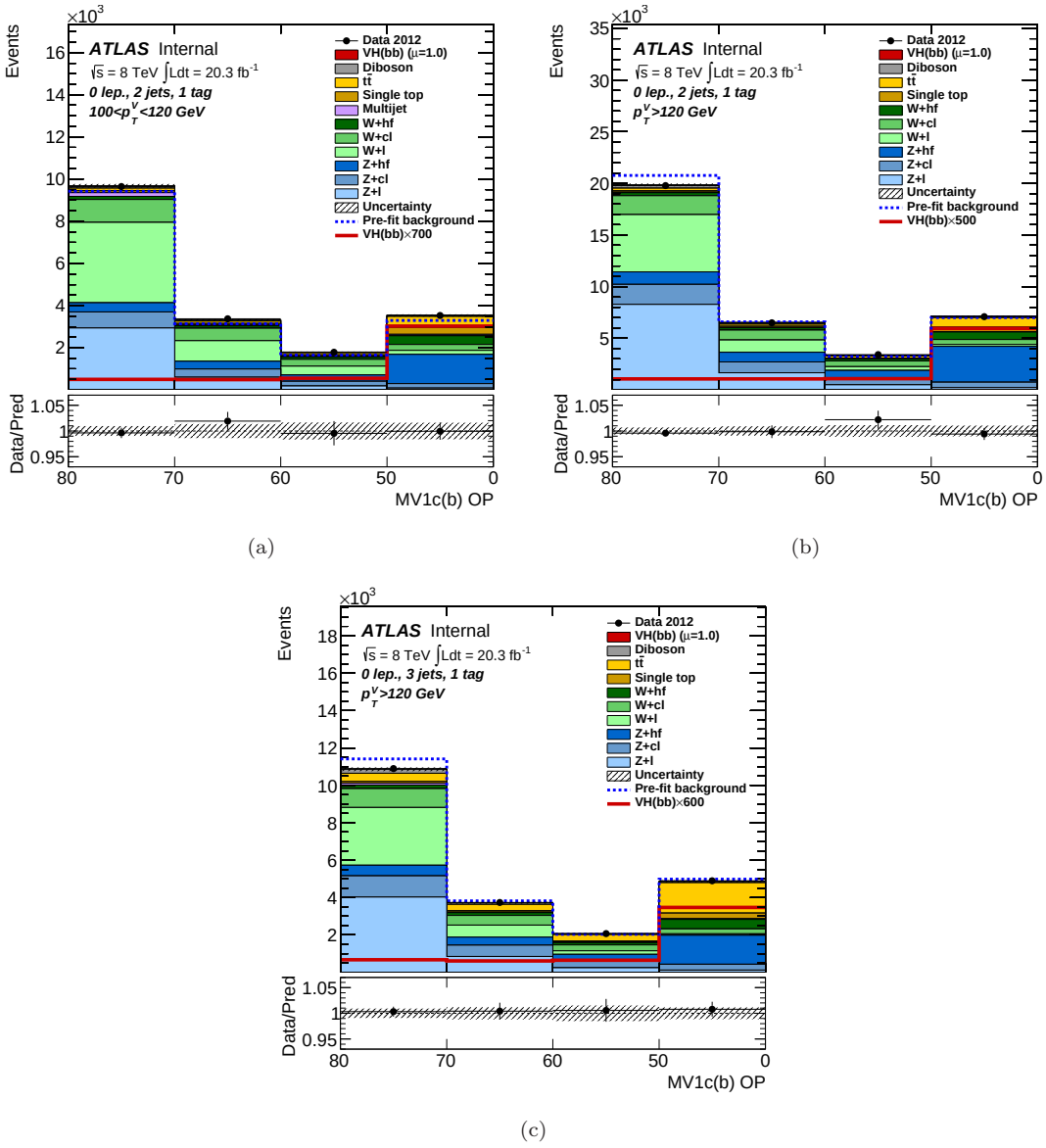

FIGURE 6.17: Post-fit distributions of the MV1c tag weight from the 0-lepton analysis 1-tag regions; (a) 2-jet low E_T^{miss} (b) 2-jet and (c) 3-jet. The fitted background is shown through the various stacked MC histograms along with the observed data points and expected signal for a 125 GeV SM Higgs boson. The pre-fit background is also shown.

- (b) The BDT is trained individually for the specific mass point under consideration

The result of the different training can be seen in figure 6.28 for the 0-lepton analysis defined in [74]. Figure 6.28 (a) shows the 125 GeV training and 6.28 (b) shows the individual mass point training, table 6.15 gives a comparison between the two results. The result at 125 GeV is, as expected, the same. However, it can be clearly seen that at mass points other than 125 GeV by training the BDT for that mass point the analysis gains sensitivity. This is particulary apparent at the extreme mass points which

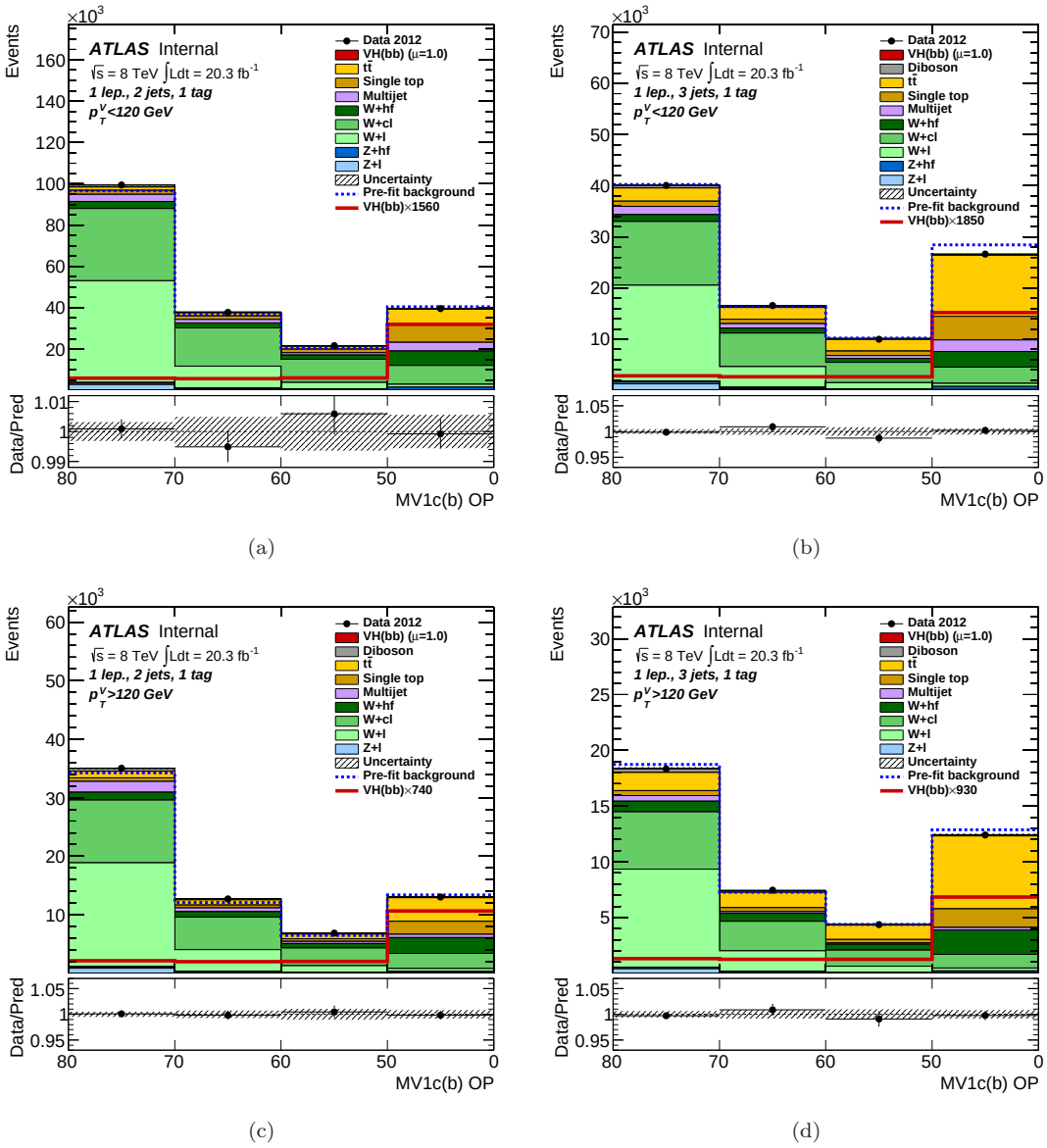

FIGURE 6.18: Post-fit distributions of the MV1c tag weight from the 1-lepton analysis 1-tag regions for $p_T^V < 120$ (a) 2-jet and (b) 3-jet, and $p_T^V > 120$ (c) 2-jet and (d) 3-jet. The fitted background is shown through the various stacked MC histograms along with the observed data points and expected signal for a 125 GeV SM Higgs boson. The pre-fit background is also shown.

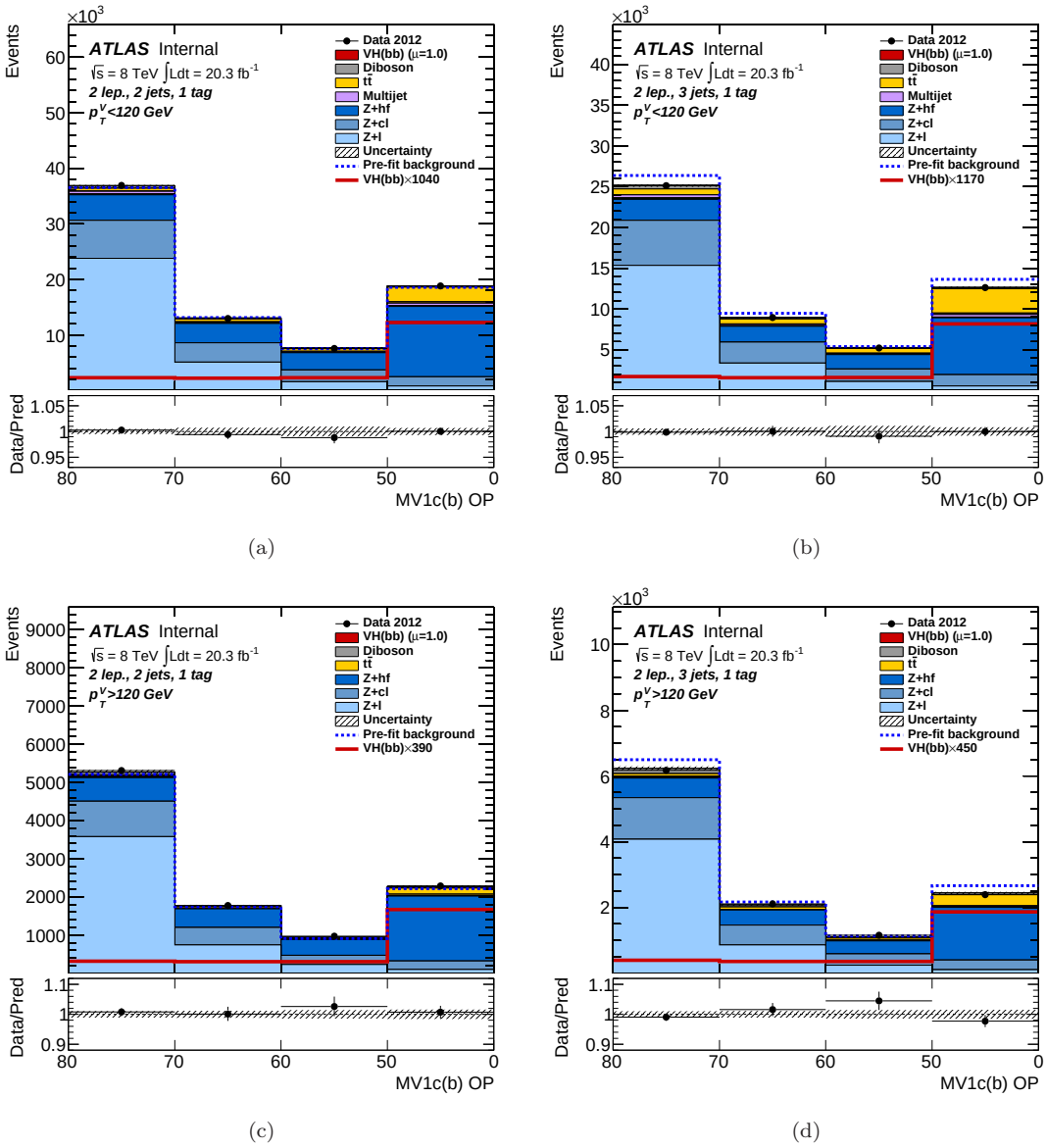

FIGURE 6.19: Post-fit distributions of the MV1c tag weight from the 2-lepton analysis 1-tag regions for $p_T^V < 120$ (a) 2-jet and (b) 3-jet, and $p_T^V > 120$ (c) 2-jet and (d) 3-jet. The fitted background is shown through the various stacked MC histograms along with the observed data points and expected signal for a 125 GeV SM Higgs boson. The pre-fit background is also shown.

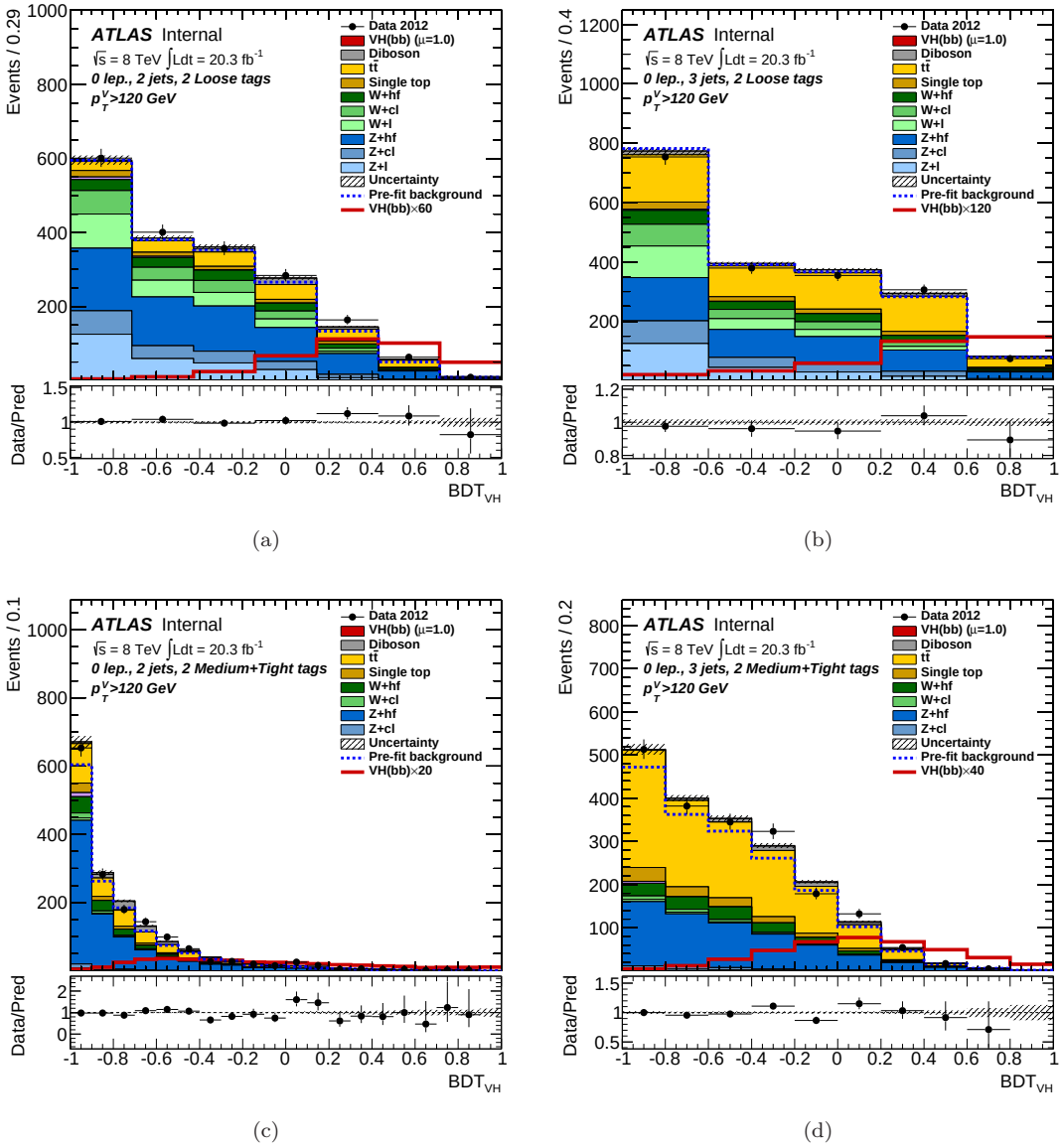

FIGURE 6.20: Post-fit distributions of the BDT output from the 0-lepton analysis 2-tag regions for $E_T^{\text{miss}} > 120$ 2-jet (a) LL and (b) MM+TT, and 3-jet (c) LL and (d) MM+TT. The fitted background is shown through the various stacked MC histograms along with the observed data points and expected signal for a 125 GeV SM Higgs boson. The pre-fit background is also shown.

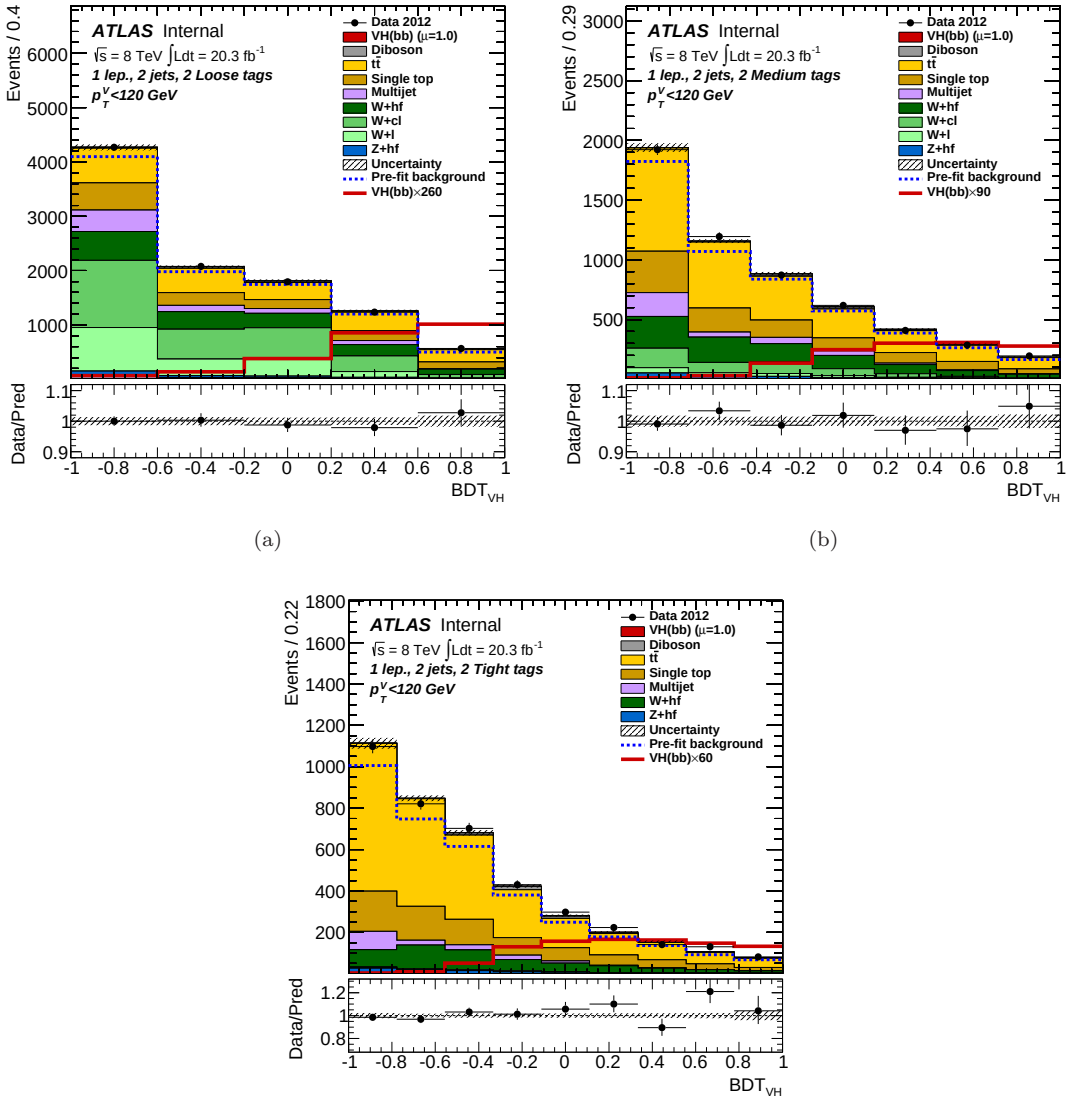

FIGURE 6.21: Post-fit distributions of the BDT output from the 1-lepton analysis 2-tag regions for $p_T^V < 120$ 2-jet (a) LL and (b) MM and (c) TT. The fitted background is shown through the various stacked MC histograms along with the observed data points and expected signal for a 125 GeV SM Higgs boson. The pre-fit background is also shown.

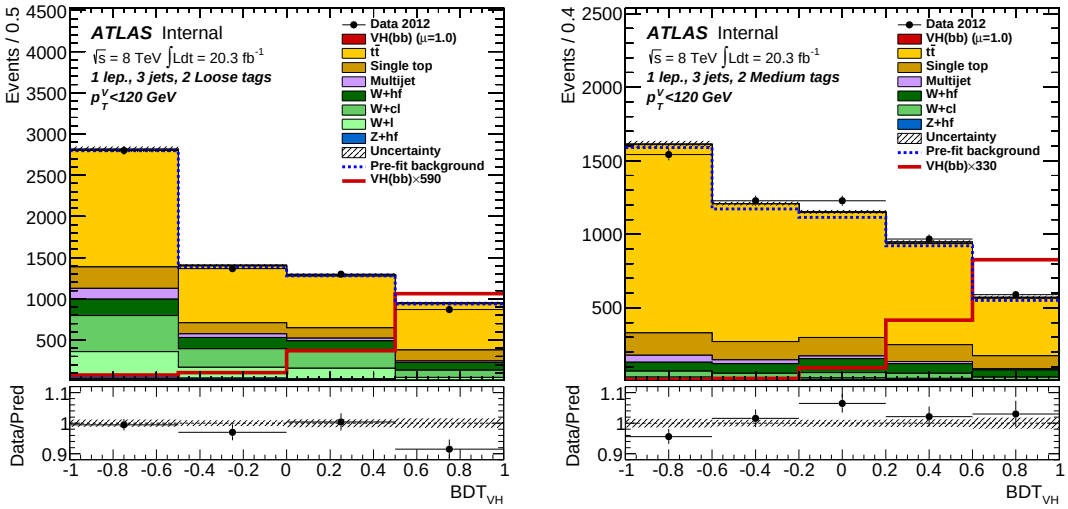

(a)

(b)

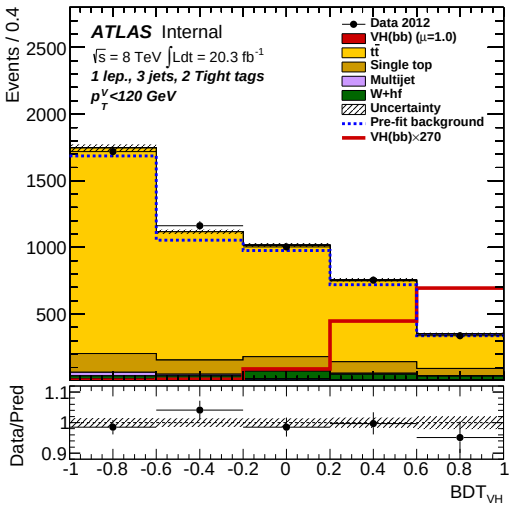

(c)

FIGURE 6.22: Post-fit distributions of the BDT output from the 1-lepton analysis 2-tag regions for $p_T^V < 120$ 3-jet (a) LL and (b) MM and (c) TT. The fitted background is shown through the various stacked MC histograms along with the observed data points and expected signal for a 125 GeV SM Higgs boson. The pre-fit background is also shown.

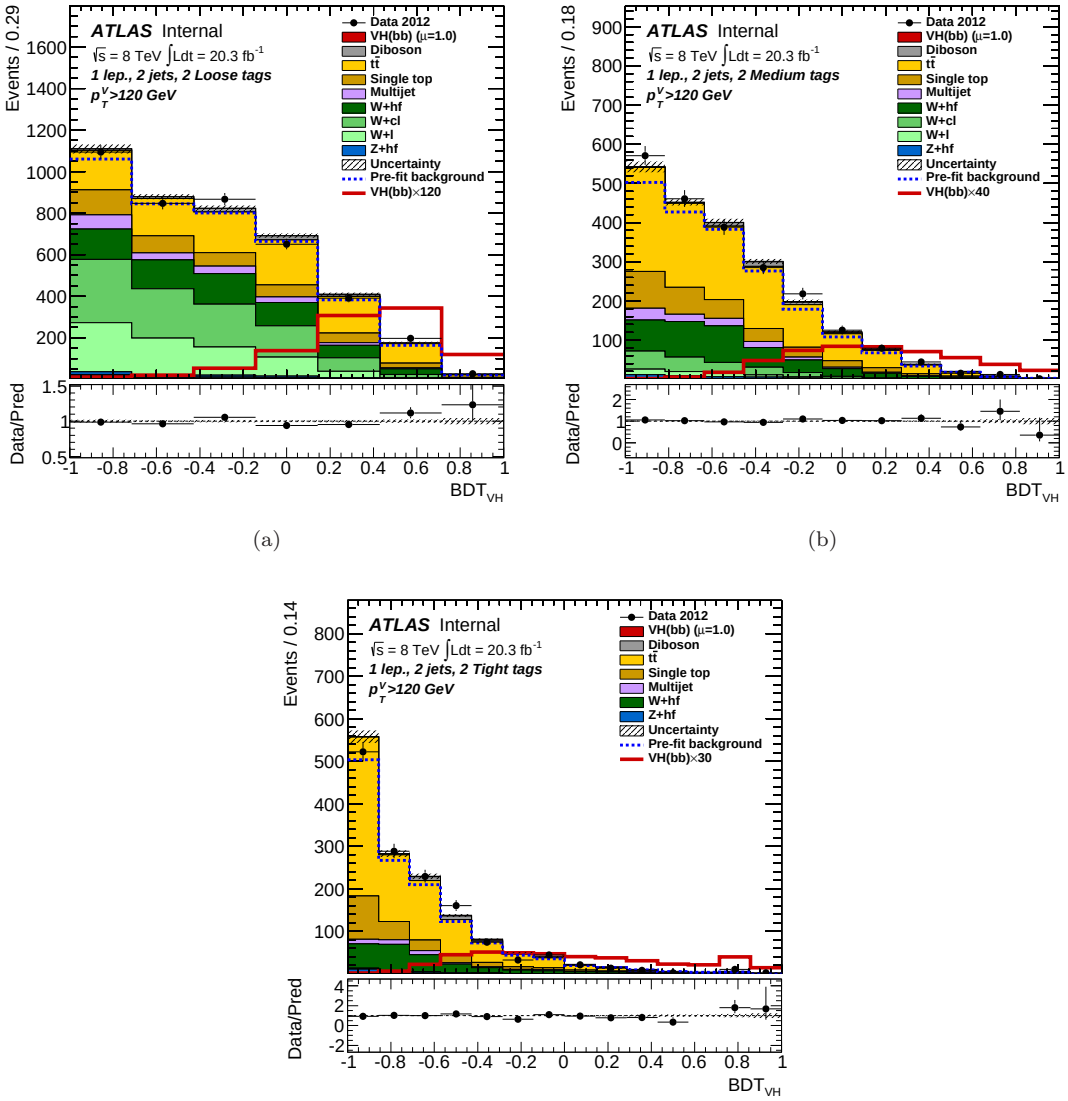

(a) (b)

(c)

FIGURE 6.23: Post-fit distributions of the BDT output from the 1-lepton analysis 2-tag regions for $p_T^V > 120$ 2-jet (a) LL and (b) MM and (c) TT. The fitted background is shown through the various stacked MC histograms along with the observed data points and expected signal for a 125 GeV SM Higgs boson. The pre-fit background is also shown.

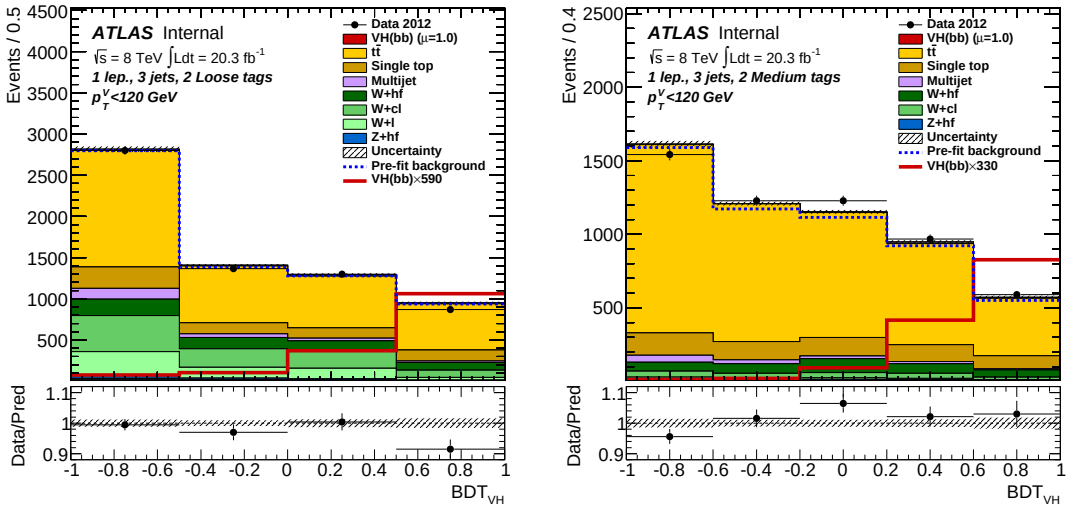

(a)

(b)

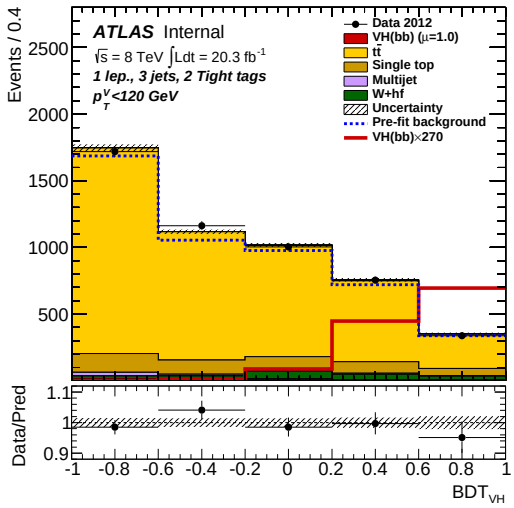

(c)

FIGURE 6.24: Post-fit distributions of the BDT output from the 1-lepton analysis 2-tag regions for $p_T^V > 120$ 3-jet (a) LL and (b) MM and (c) TT. The fitted background is shown through the various stacked MC histograms along with the observed data points and expected signal for a 125 GeV SM Higgs boson. The pre-fit background is also shown.

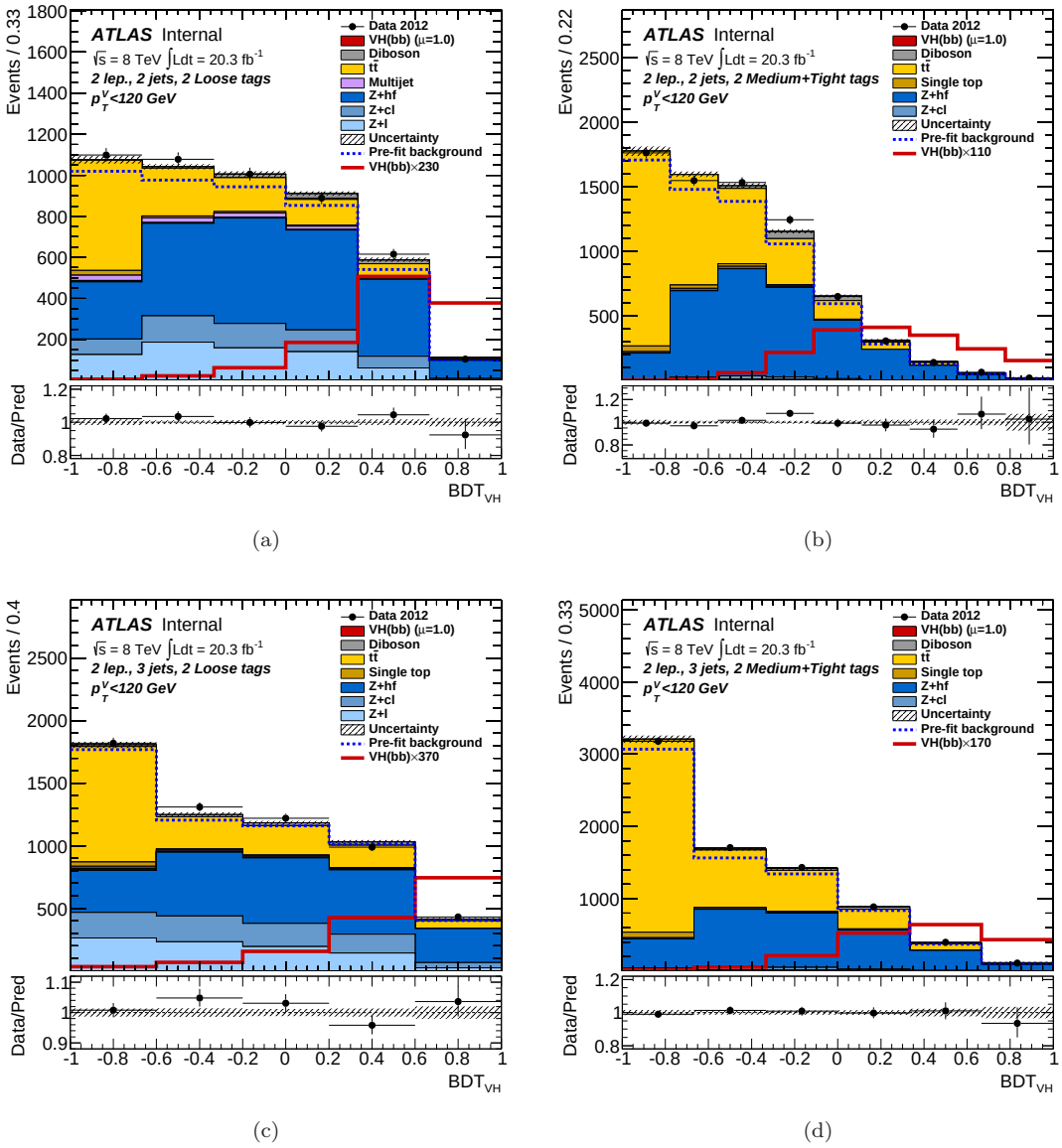

FIGURE 6.25: Post-fit distributions of the BDT output from the 2-lepton analysis 2-tag regions for $p_T^V < 120$ 2-jet (a) LL and (b) MM+TT, and 3-jet (c) LL and (d) MM+TT. The fitted background is shown through the various stacked MC histograms along with the observed data points and expected signal for a 125 GeV SM Higgs boson. The pre-fit background is also shown.

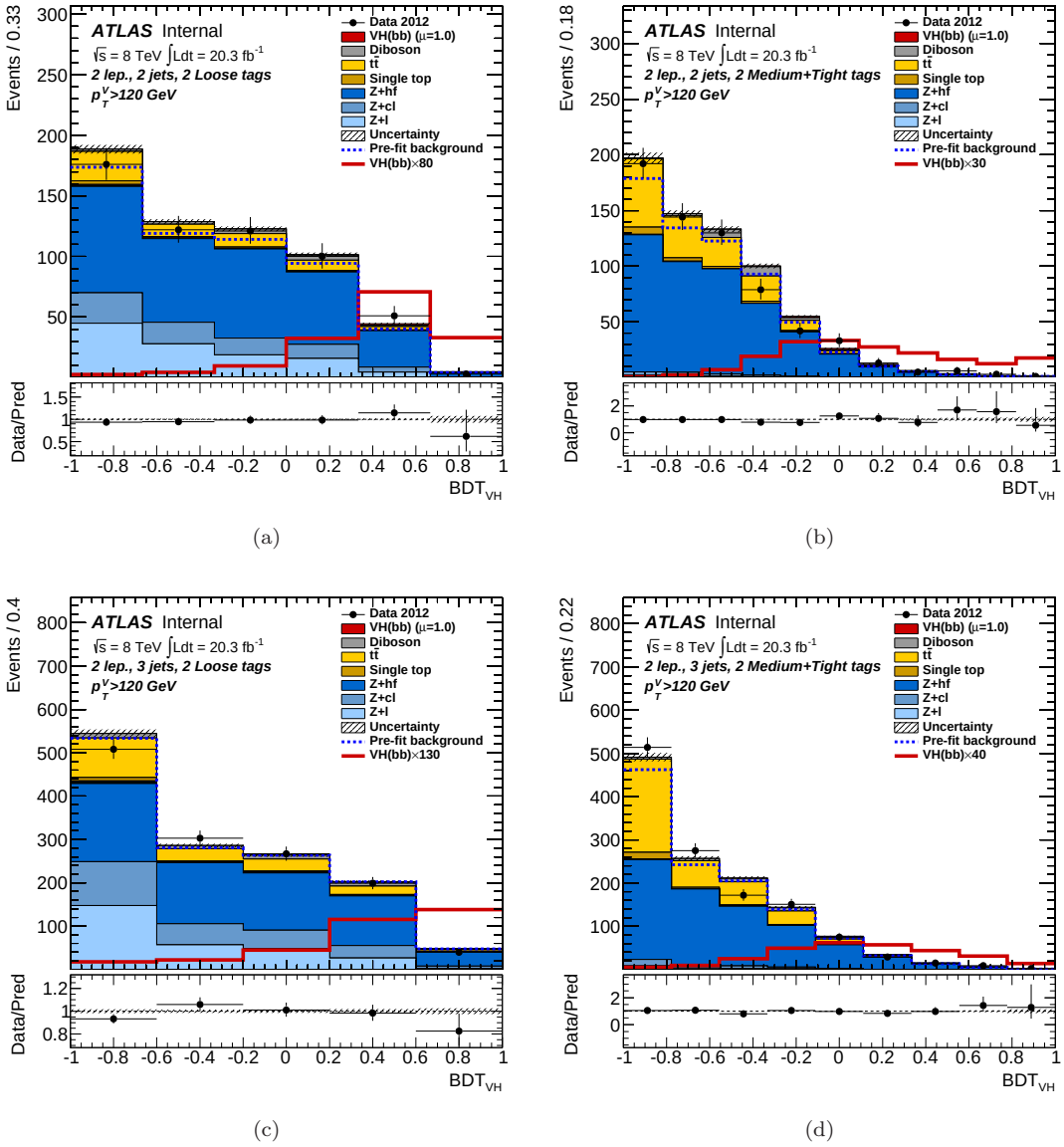

FIGURE 6.26: Post-fit distributions of the BDT output from the 2-lepton analysis 2-tag regions for $p_T^V > 120$ 2-jet (a) LL and (b) MM+TT, and 3-jet (c) LL and (d) MM+TT. The fitted background is shown through the various stacked MC histograms along with the observed data points and expected signal for a 125 GeV SM Higgs boson. The pre-fit background is also shown.

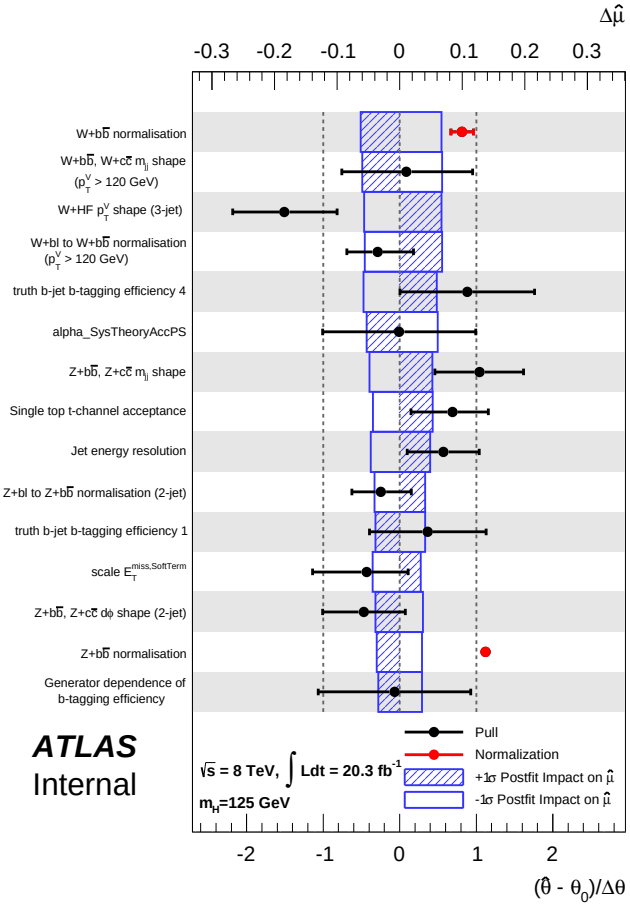

FIGURE 6.27: Impact of the top ten ranked NP in the combined 012 fit on the fitted signal strength, μ. The NP are listed in order of rank down the y-axis. The black circles show the deviation of the NPs from the nominal pre-fit values expressed in terms of standard deviations with respect to the nominal pre-fit uncertainties. The black lines show the post-fit uncertainties on the given NP relative to the pre-fit value, measured by the bottom x-axis. The red circles and lines show the corresponding values for NP which float freely in the fit. The blue box shows the fractional variation of the signal strength, measured by the top x-axis. These variations are calculated by performing the fit again with each NP fixed to its post-fit value shifted up (dashed box) and down (open box) by its nominal uncertainty with all other NPs are allowed to vary.

benifit more from the retraining as they are further away from 125 GeV. The respective sensitivity gain is around 39% and 70% for the 110 GeV and 140 GeV mass points.

Mass	Expected		Observed	
(GeV)	125 GeV Training	Mass Training	125 GeV Training	Mass Training
110	1.29	0.93	1.41	1.00
115	1.21	1.03	1.13	1.07
120	1.23	1.19	1.11	1.09
125	1.38	1.34	1.25	1.61
130	1.93	1.81	1.92	2.11
135	2.97	2.33	3.72	2.62
140	5.21	3.06	6.06	4.35

TABLE 6.15: Expected and observed significances for the published VH analysis [74] shown with and without individual mass point training on the MVA.

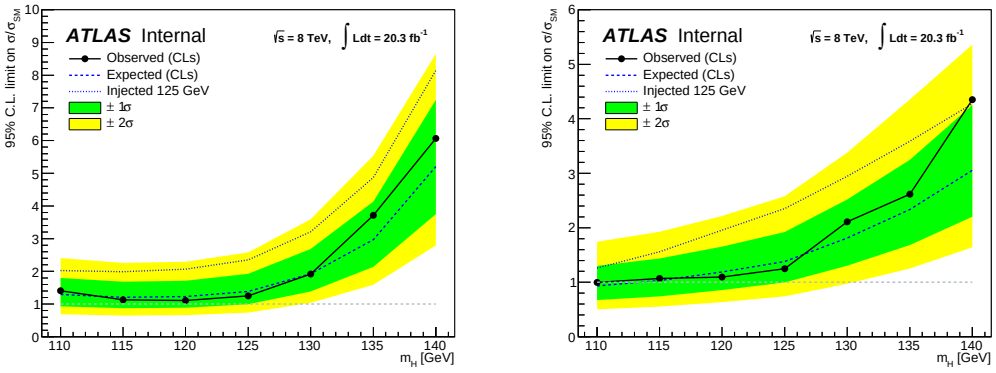

(a) (b)

FIGURE 6.28: Expected exclusion limits as a function of Higgs Mass for the 0-lepton analyses defined in [74], (a) shows the result using 125 GeV training and (b) shows the result for individual mass point training

Chapter 7

Results

This chapter will present the results of the analysis presented in section 6. The 0-lepton MVA inputs to the fit, where $E_T^{\text{miss}} > 120$ GeV, have been produced independently from the published analysis [74], any differences are outlined in section 7.1. The low E_T^{miss} inputs are produced through a separate cut based analysis, details of which can be found in [74]. The 2-lepton inputs used in the fit are produced following [74] however the selection of 3-jet events has been changed to that described in section 7.1. The 1-lepton inputs to the fit are identical to those used in the published result.

7.1 Differences to Paper Analysis

The results presented in this thesis are based on the analysis presented in [74]. It is, however, independent in the fact that the inputs have been produced using a different analysis framework. It should be noted, the framework has been verified through analysis cut flows and cross checks of the 0- and 2- lepton analyses, it was also used to produce the 2-lepton inputs used in the paper.

There are some small improvements in selection and implementation to the paper. Primarily the selection of 3-jet events. The 3-jet events in the 0- and 2-lepton analyses are selected based on the studies presented in section 6.3.4.1. Furthermore, the selection has been updated to include forward jets; events containing a total of 3 signal + forward jets are labelled as 3-jet.

Any other discrepancies are due to the different analysis chains. The published analysis [74] uses centrally produced ATLAS ntuples. The analysis presented here is undertaken using ntuples produced independently. This difference allowed for a detailed cross check of the published result.

7.2 Results

Results have been obtained following the statistical procedure outlined in 6.7 using the 0-, 1- and 2- lepton analysis inputs simultaneously, henceforth referred to as the 012 fit. This section will present the outcome of this fit, as well as the individual 0-lepton fit results. Postfit plots have already been shown in figures 6.16 - 6.26. The impact of NPs has also been discussed in section 6.7.2.

Figure 7.1 shows the 95% confidence level upper limits on SM Higgs boson cross section times branching ratio for $pp \rightarrow V(H \rightarrow b\bar{b})$ in the mass range 110 - 140 GeV. The observed limit for $m_H = 125$ GeV is 1.6 times the SM value compared to an expected value of 0.8 in the absence of any signal. For the 0-lepton only fit, figure 7.3 the observed limit for $m_H = 125$ GeV is 1.6 times the SM value compared to an expected value of 1.3.

The corresponding p_0 value tests the probability of obtaining the observed result assuming the background only hypothesis. Figure 7.2 and 7.4 show the expected and observed p_0 as a function of m_H for the 012 and 0-lepton only fit respectively. The combined fit sees an excess with an observed (expected) significance of 2.1σ (2.5σ), the 0-lepton only fit sees an excess with an observed (expected) significance of 0.4σ (1.5σ).

The best fit values of the signal strength, $\hat{\mu}$, for $m_H = 125$ GeV are shown in figure 7.5 for individual channels and the combined fit. The resulting $\hat{\mu} = 0.84^{+045}_{-0.32}$ and for the 0-lepton only fit $\hat{\mu} = 0.22^{+0.73}_{-0.67}$.

7.2.1 Comparison to Published Results

Section 7.1 has already highlighted the improvements which have been made from the published analysis, this section offers a direct comparison to the 8 TeV data results.

Table 7.2.1 compares the measured significance of the different channels at the 125 GeV mass point. Results are compared for the 0- and 2-lepton channels and the combined 012-lepton fit. Values are shown for the observed and expected significances, as well as a so called Asimov significance. The Asimov significance is obtained by defining a pseudo-dataset built from MC, the Asimov dataset, where all NPs are set to 0 and scale factors set to 1. The error on each bin of the Asimov dataset is Poisson. The Asimov dataset, unlike real data, will not have fluctuations. However, the associated errors are the same as one would obtain with real data. When the Asimov dataset is fit, scale factor and NP errors correspond to the constrains one would get from real data without

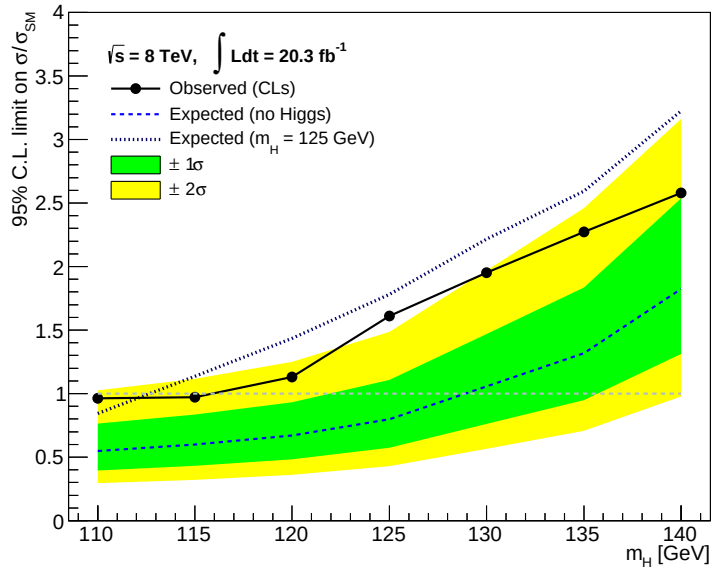

FIGURE 7.1: Observed (solid) and expected 95% CL cross-section upper limits, as a function of m_H, obtained through the simultaneous 0-, 1- and 2-lepton fit. The expected upper limit is given for the background only hypothesis (dashed) and with the injection of a 125 GeV Higgs boson (dotted). The dark and light bands represent the 1σ and 2σ ranges of the background only expectation.

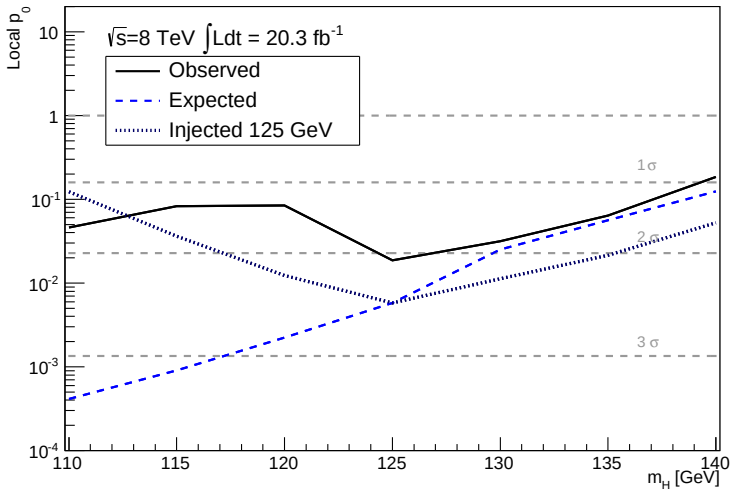

FIGURE 7.2: Observed (solid) and expected p_0 values, as a function of m_H, obtained through the simultaneous 0-, 1- and 2-lepton fit. The expected p_0 is shown for several values of m_H (dashed), as well as for $m_H = 125$ GeV (dotted).

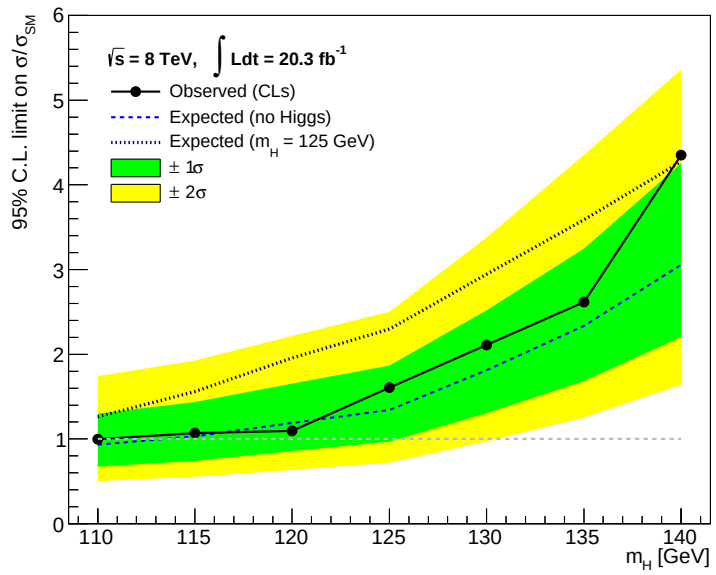

FIGURE 7.3: Observed (solid) and expected 95% CL cross-section upper limits, as a function of m_H, obtained through the 0-lepton fit. The expected upper limit is given for the background only hypothesis (dashed) and with the injection of a 125 GeV Higgs boson (dotted). The dark and light bands represent the 1σ and 2σ ranges of the background only expectation.

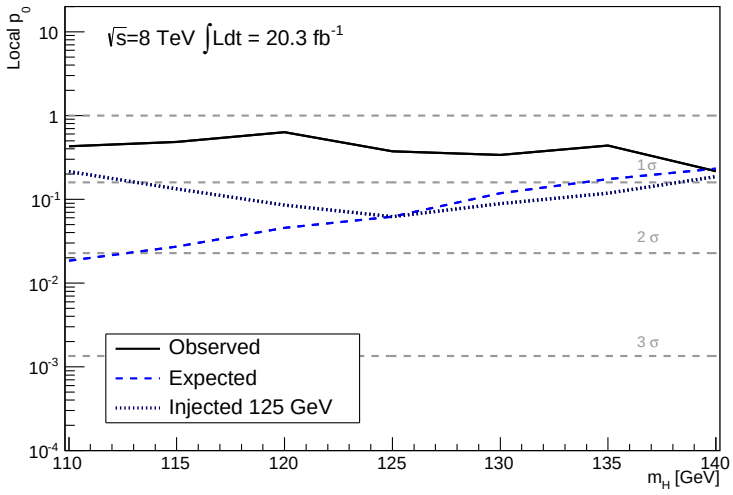

FIGURE 7.4: Observed (solid) and expected p_0 values, as a function of m_H, obtained through the 0-lepton fit. The expected p_0 is shown for several values of m_H (dashed), as well as for $m_H = 125$ GeV (dotted).

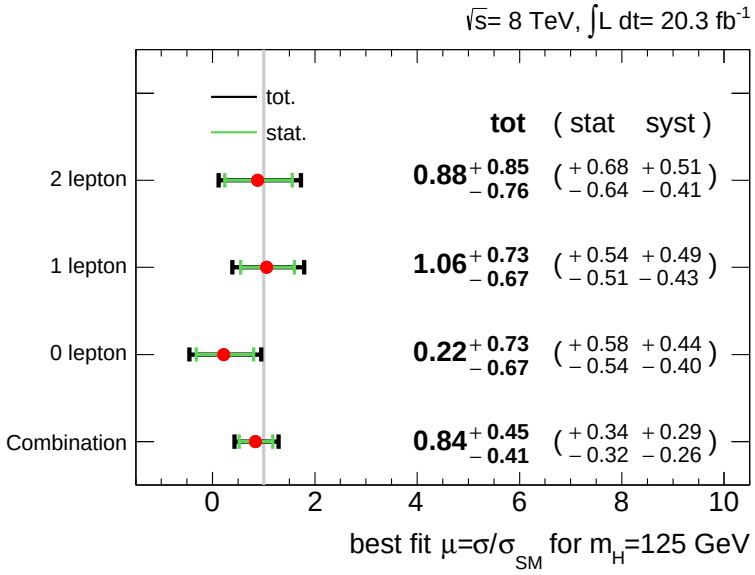

(a)

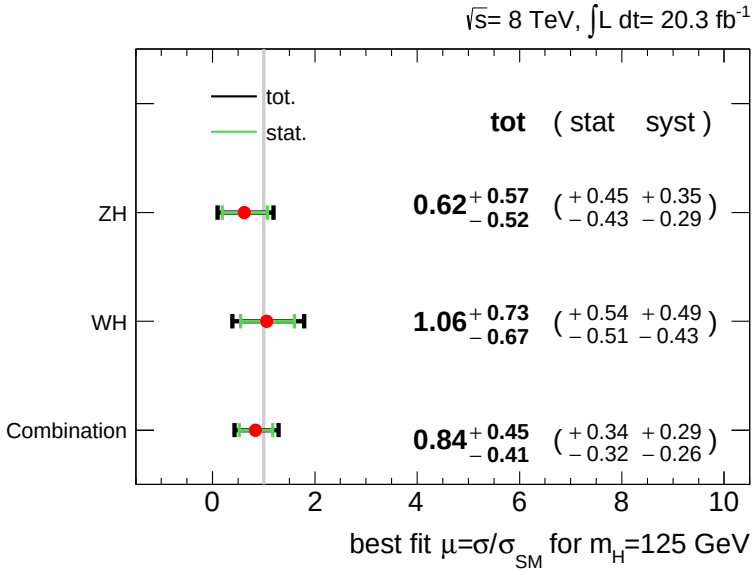

(b)

FIGURE 7.5: The best fit signal strength, $\hat{\mu}$, for $m_H = 125$ GeV shown with associated uncertainties for (a) the individual 0-, 1- and 2-lepton analyses and the combined simultaneous fit result, (b) ZH and WH processes and the combined simultaneous fit result.

0-Lepton		
	Thesis	Paper
Asimov	1.62	1.59
Expected	1.54	1.48
Observed	0.33	-0.38

2 Lepton		
	Thesis	Paper
Asimov	1.32	1.26
Expected	1.29	1.22
Observed	1.16	1.20

012 Combined		
	Thesis	Paper
Asimov	2.52	2.50
Expected	2.53	2.53
Observed	2.08	1.68

TABLE 7.1: Comparison of published [84] and presented Asimov, expected and observed significance at $m_H = 125$ GeV.

any statistical fluctuations. The Asimov significance is therefore a good indication of analysis improvement.

Improvements are seen in both the 0- and 2-lepton analysis, the Asimov significance increases from 1.59 to 1.62 and 1.26 to 1.32 respectively. In the overall fit the Asimov significance increases from 2.50 to 2.52. The observed combined significance is seen to increase from 1.68 to 2.08 times the standard model value. This is driven by an increase seen in the 0-lepton analysis.

The best fit signal strength for the 0-lepton analysis is measured to be $\hat{\mu} = 0.22^{+0.73}_{-0.67}$, compared to the $\hat{\mu} = -0.25^{+0.60}_{0.78}$ in the published analysis. The published result measured a low $\hat{\mu}$ due to a data deficit observed in the most sensitive bins of the BDT output [74]. The overall value of the best fit signal strength is measured to be $\hat{\mu} = 0.84^{+045}_{-0.32}$ compared to $\hat{\mu} = 0.65^{+043}_{-0.40}$ measured in the published analysis. This increase is due to the changes in the 0 and 2-lepton analyses.

7.3 Summary

A search for the SM Higgs boson decaying in to a pair of b-quarks produced in association with a Z boson using 20.3fb^{-1} of $\sqrt{8}$ TeV ATLAS proton-proton data has been presented.

Results have been shown for the $ZH \rightarrow \nu\nu b\bar{b}$ channel, presented in section 6. As well as for a combined analysis with two other associated production channels; $WH \rightarrow l\nu b\bar{b}$ and $ZH \rightarrow llb\bar{b}$.

The search is performed using a BDT analysis. Each of the three channels are categorised by the number of leptons, jets and b-tagged jets, as well as the transverse momentum of the associated vector boson. A complex simultaneous fit uses the BDT output as a discriminant along with b-tagging information from the MV1c algorithm. In the low E_T^{miss} region of the 0-lepton channel the m_{bb} distribution is used as the discriminant. The fit considers the impact of systematic uncertainties as a series of NP and extracts a best fit value for the signal strength by comparing the agreement between collected data and simulated MC events.

For a Higgs boson $m_H = 125$ GeV best fit values of the signal strength are measured to be $\hat{\mu} = 0.22^{+0.73}_{-0.67}$ for the 0-lepton only fit and $\hat{\mu} = 0.84^{+0.45}_{-0.32}$ for the combined simultaneous fit. The observed (expected) deviation from the background only hypothesis corresponds to 0.3σ (1.5σ) for the 0-lepton only fit and 2.1σ (2.5σ) for the combined simultaneous fit.

Chapter 8

Thesis Summary

The LHC is a tool which allows the study of fundamental particle physics at extremely high energies. The four main experiments situated around the LHC enable a broad physics program to be studied. This thesis has presented two analyses undertaken with $p-p$ data recorded by the ATLAS detector it highlights only a small contribution to a vast amount of work which has been produced by the collaboration so far.

Chapter 5 presented a technical study using MC to investigate the b-jet efficiency and estimate systematic uncertainties as a function of p_T and η. This analysis resulted in the implimentation of a MC extrapolation of the associated b-tagging uncertainties in ATLAS data in high p_T events; up to 1.2 TeV for b-, c- and l-jets, and to 800 GeV for τ flavoured jets. The extrapolation for 2012 data is currently used throughout ATLAS and is vital for analyses with a signal which contains several high p_T jets.

Chapter 6 then presented a search for the Standard Model Higgs boson. The analysis probes one particular decay channel where the Higgs boson, decaying into a pair of b-quarks, is produced in association with another massive vector boson, identified through a decay to two neutrinos. The MVA analysis is combined and simultaneously fit with two other associated production channels. For a higgs Boson $m_H = 125$ GeV best fit values of the signal strength are measured to be $\hat{\mu} = 0.22^{+0.73}_{-0.67}$ for the 0-lepton only fit and $\hat{\mu} = 0.84^{+0.45}_{-0.32}$ for the combined simultaneous fit. The observed (expected) deviation from the background only hypothesis corresponds to 0.3σ (1.5σ) for the 0-lepton only fit and 2.1σ (2.5σ) for the combined simultaneous fit. The results are consistant with the SM, however, a discovery of the Higgs boson decaying to a pair of b-quarks can not be stated, further data and analysis is required.

Appendix A

Estimating b-Tagging Efficiency Uncertainties in Monte Carlo Results

This appendix contains tables of numbers for the tagging algorithms reccomended for 2012 physic analyses at several operating points. The tables show a breakdown of the total systematic uncertainty on b-tagging efficiency as a function of p_T and η.

	p_T GeV													
	20-30	30-40	40-50	50-60	60-75	75-90	90-110	110-140	140-200	200-300	300-500	500-800	800-1200	1200-2000
Jet Systs	3.0	0.3	0.9	0.3	0.3	0.8	0.8	1.0	0.6	0.5	0.7	1.6	7.1	10.0
Plie Up	0.2	0.7	0.3	0.2	0.3	0.3	-0.1	0.2	0.4	0.1	0.2	-0.1	-0.6	-16.6
Track Multiplicity	1.0	0.8	0.6	0.6	0.7	0.5	0.5	0.4	0.8	0.7	0.8	0.7	3.0	-3.4
Smear η	-5.6	-2.9	-1.1	-0.8	-0.9	-1.6	-1.1	-2.4	-3.2	-0.2	2.9	4.6	10.7	37.8
Smear ϕ	-6.9	-3.5	-1.8	-1.2	-1.6	-2.7	-1.7	-3.3	-5.2	-2.2	3.6	3.3	4.5	33.5
Shared Hits	-1.3	0.2	1.1	1.3	1.9	2.2	3.3	3.6	5.6	8.2	16.7	24.8	22.6	24.7
Smear d_0	-2.9	-1.9	-0.7	-0.5	-0.7	-0.9	-0.7	-1.5	-1.5	-0.4	2.7	-1.4	5.0	5.0
Smear z_0	-1.9	-0.7	-0.7	-0.5	-0.0	0.2	0.2	-1.3	-0.1	0.6	1.3	4.1	14.2	14.2
Fake Rate	-3.1	-1.4	0.0	0.2	0.1	-0.2	-0.1	-0.8	-0.9	0.6	3.9	7.6	8.4	20.9
Total Syst	10.5	5.3	2.8	2.2	2.8	4.0	4.1	6.0	8.5	8.6	18.0	26.9	31.7	64.9
Stat Err	1.8	1.2	1.1	1.0	0.8	0.9	1.0	1.2	1.6	1.8	1.2	3.4	22.5	36.6

	η			
	0-0.6	0.6-1.2	1.2-1.8	1.8-2.5
Jet Systs	0.2	0.2	0.3	0.4
Plie Up	0.3	0.3	0.2	0.5
Track Multiplicity	0.7	0.6	0.7	1.2
Smear η	-2.4	-2.7	-2.7	-2.6
Smear ϕ	-3.4	-4.0	-4.0	-3.7
Shared Hits	1.7	1.9	3.8	3.0
Smear d_0	-1.3	-1.7	-1.7	-2.1
Smear z_0	-0.6	-0.9	-0.8	-0.7
Fake Rate	-0.9	-1.3	-0.5	-0.5
Total Syst	4.9	5.8	6.5	6.0
Stat Err	0.6	0.7	1.0	1.6

TABLE A.1: A breakdown of the contribution of the systematic uncertainties for each p_T (top) and η (bottom) bin using the MV1 tagger at 60% efficiency for b-jets. Values show the percentage error for each point.

	p_T GeV													
	20-30	30-40	40-50	50-60	60-75	75-90	90-110	110-140	140-200	200-300	300-500	500-800	800-1200	1200-2000
Jet Systs	0.9	0.2	0.6	0.1	0.2	0.2	0.1	0.2	0.5	0.5	0.5	0.6	4.7	14.4
Plie Up	-0.1	0.2	0.2	0.1	0.2	0.1	0.1	0.1	0.3	0.1	0.1	-0.3	0.9	3.8
Track Multiplicity	0.5	0.4	0.3	0.3	0.3	0.2	0.2	0.2	0.4	0.2	0.3	0.2	-0.7	0.8
Smear η	-3.3	-1.5	-0.8	-0.4	-0.5	-0.8	-0.7	-1.3	-1.4	0.4	1.1	3.4	2.6	-13.9
Smear ϕ	-4.1	-2.1	-1.4	-0.9	-0.7	-1.0	-1.2	-2.0	-2.7	-0.3	1.3	1.8	7.6	21.3
Shared Hits	-0.8	-0.1	0.2	0.6	0.8	1.0	1.4	1.4	2.9	4.6	8.7	14.6	17.5	-47.7
Smear d_0	-1.7	-0.9	-0.4	-0.2	-0.3	-0.3	-0.5	-0.9	-1.1	-0.2	0.4	-0.2	-4.0	5.9
Smear z_0	-1.5	-0.7	-0.4	-0.2	-0.3	-0.2	-0.3	-0.6	-0.8	-0.0	0.1	2.4	-1.2	9.6
Fake Rate	-1.3	-0.6	-0.1	0.1	0.2	-0.0	0.0	-0.3	-0.3	1.3	2.2	5.3	3.6	73.8
Total Syst	6.1	2.9	1.8	1.3	1.3	1.7	2.0	3.0	4.5	4.9	9.2	16.2	20.6	93.4
Stat Err	0.9	0.6	0.6	0.5	0.4	0.5	0.5	0.7	0.8	0.9	0.5	1.2	16.2	74.5

	η			
	0-0.6	0.6-1.2	1.2-1.8	1.8-2.5
Jet Systs	0.1	0.1	0.2	0.2
Plie Up	0.2	0.2	0.1	0.1
Track Multiplicity	0.3	0.3	0.3	0.5
Smear η	-1.3	-1.3	-1.6	-1.6
Smear ϕ	-1.8	-2.0	-2.2	-2.4
Shared Hits	0.6	0.8	1.4	1.6
Smear d_0	-0.7	-0.9	-1.0	-0.9
Smear z_0	-0.4	-0.7	-1.2	-0.8
Fake Rate	-0.5	-0.4	-0.2	0.0
Total Syst	2.5	2.8	3.5	3.6
Stat Err	0.3	0.4	0.5	0.8

TABLE A.2: A breakdown of the contribution of the systematic uncertainties for each p_T (top) and η (bottom) bin using the MV1 tagger at 70% efficiency for b-jets. Values show the percentage error for each point.

	p_T GeV													
	20-30	30-40	40-50	50-60	60-75	75-90	90-110	110-140	140-200	200-300	300-500	500-800	800-1200	1200-2000
Jet Systs	0.6	0.3	0.5	0.2	0.2	0.2	0.1	0.1	0.2	0.2	0.1	0.3	3.3	14.5
Plie Up	0.1	0.0	0.1	0.1	0.1	-0.0	0.1	-0.0	0.2	0.0	0.1	-0.0	0.8	2.1
Track Multiplicity	0.2	0.1	0.1	0.1	0.1	0.1	0.1	0.0	0.3	0.1	0.2	-0.0	1.1	0.1
Smear η	-1.7	-0.6	-0.4	-0.3	-0.1	-0.5	-0.3	-0.6	-1.4	0.1	0.0	1.1	0.8	-21.8
Smear ϕ	-2.2	-0.8	-0.8	-0.6	-0.2	-0.7	-0.6	-0.8	-1.8	0.1	0.2	0.4	1.9	13.4
Shared Hits	-0.5	0.0	0.1	0.1	0.4	0.3	0.4	0.5	0.5	1.7	3.4	6.3	9.9	0.2
Smear d_0	-1.2	-0.7	-0.4	-0.6	-0.3	-0.5	-0.4	-0.5	-1.3	-0.0	-0.3	-0.8	-2.6	-1.1
Smear z_0	-1.0	-0.6	-0.4	-0.6	-0.1	-0.4	-0.5	-0.6	-1.1	-0.3	-0.5	-0.0	-0.1	13.1
Fake Rate	-0.7	-0.3	-0.0	-0.1	0.2	-0.1	-0.1	-0.1	-0.5	0.5	1.0	2.3	3.7	3.7
Total Syst	3.3	1.4	1.1	1.1	0.7	1.1	1.0	1.4	3.0	1.8	3.6	6.9	11.6	32.5
Stat Err	0.6	0.4	0.4	0.3	0.3	0.3	0.3	0.4	0.5	0.5	0.3	0.6	5.3	30.5

	η			
	0-0.6	0.6-1.2	1.2-1.8	1.8-2.5
Jet Systs	0.1	0.1	0.1	0.2
Plie Up	0.1	0.1	0.1	0.1
Track Multiplicity	0.1	0.1	0.2	0.3
Smear η	-0.5	-0.7	-0.9	-0.6
Smear ϕ	-0.7	-0.9	-1.3	-0.9
Shared Hits	0.2	0.2	0.4	0.7
Smear d_0	-0.6	-0.6	-0.9	-0.8
Smear z_0	-0.2	-0.6	-1.3	-0.9
Fake Rate	-0.2	-0.2	-0.3	0.2
Total Syst	1.2	1.5	2.3	1.8
Stat Err	0.2	0.2	0.3	0.5

TABLE A.3: A breakdown of the contribution of the systematic uncertainties for each p_T (top) and η (bottom) bin using the MV1 tagger at 80% efficiency for b-jets. Values show the percentage error for each point.

	p_T GeV													
	20-30	30-40	40-50	50-60	60-75	75-90	90-110	110-140	140-200	200-300	300-500	500-800	800-1200	1200-2000
Jet Systs	0.6	0.3	0.3	0.2	0.1	0.1	0.2	0.2	0.2	0.2	0.1	0.1	3.6	16.2
Plie Up	0.1	0.0	0.0	0.1	0.0	0.0	0.0	0.0	0.2	-0.0	0.1	-0.0	-0.0	1.7
Track Multiplicity	0.1	0.1	0.1	0.1	0.1	0.1	0.1	0.0	0.3	0.1	0.1	0.0	-0.5	-0.8
Smear η	-1.1	-0.4	-0.2	-0.2	-0.1	-0.5	-0.3	-0.5	-1.0	-0.1	0.0	1.1	0.5	-0.9
Smear ϕ	-1.6	-0.5	-0.6	-0.5	-0.2	-0.7	-0.5	-0.7	-1.5	-0.3	0.1	0.4	0.1	8.0
Shared Hits	-0.2	0.0	0.0	0.1	0.3	0.2	0.3	0.3	0.4	1.1	2.5	5.0	9.6	10.4
Smear d_0	-1.0	-0.7	-0.4	-0.5	-0.4	-0.5	-0.4	-0.6	-1.1	-0.3	-0.4	-0.8	-2.8	6.4
Smear z_0	-0.8	-0.5	-0.5	-0.6	-0.2	-0.5	-0.5	-0.5	-0.8	-0.5	-0.6	-0.1	0.6	-0.6
Fake Rate	-0.4	-0.1	0.1	-0.0	0.1	-0.1	-0.0	-0.1	-0.4	0.4	0.8	2.2	2.7	12.2
Total Syst	2.5	1.1	0.9	1.0	0.6	1.1	0.9	1.2	2.4	1.4	2.7	5.7	11.0	25.0
Stat Err	0.5	0.4	0.3	0.3	0.2	0.3	0.3	0.4	0.5	0.4	0.3	0.5	4.3	15.0

	η			
	0-0.6	0.6-1.2	1.2-1.8	1.8-2.5
Jet Systs	0.1	0.1	0.0	0.1
Plie Up	0.1	0.1	0.1	0.1
Track Multiplicity	0.1	0.1	0.2	0.2
Smear η	-0.4	-0.5	-0.7	-0.4
Smear ϕ	-0.6	-0.8	-1.0	-0.6
Shared Hits	0.1	0.1	0.3	0.5
Smear d_0	-0.5	-0.6	-0.9	-0.5
Smear z_0	-0.2	-0.5	-1.3	-0.9
Fake Rate	-0.1	-0.2	-0.2	0.3
Total Syst	0.9	1.3	2.0	1.4
Stat Err	0.2	0.2	0.3	0.4

TABLE A.4: A breakdown of the contribution of the systematic uncertainties for each p_T (top) and η (bottom) bin using the MV1 tagger at 85% efficiency for b-jets. Values show the percentage error for each point.

	p_T GeV													
	20-30	30-40	40-50	50-60	60-75	75-90	90-110	110-140	140-200	200-300	300-500	500-800	800-1200	1200-2000
Jet Systs	1.2	0.2	0.7	0.3	0.3	0.4	0.3	0.3	0.5	0.4	0.7	0.2	5.7	15.6
Plie Up	-0.0	0.4	0.2	0.1	0.2	0.0	0.0	0.2	0.2	0.0	0.1	-0.1	-0.3	3.3
Track Multiplicity	0.6	0.5	0.4	0.3	0.3	0.3	0.2	0.2	0.5	0.3	0.4	0.4	-3.0	-4.7
Smear η	-3.8	-2.2	-0.9	-0.9	-0.7	-0.7	-0.8	-1.4	-1.3	0.6	1.8	4.0	9.7	-55.2
Smear ϕ	-4.9	-2.8	-1.5	-1.4	-0.9	-1.0	-1.4	-1.8	-2.6	0.3	2.3	2.2	17.6	-146.5
Shared Hits	-0.8	-0.0	0.5	0.7	1.3	1.6	2.0	2.3	4.2	6.2	11.4	18.0	25.0	-207.4
Smear d_0	-1.9	-1.5	-0.6	-0.5	-0.5	-0.2	-0.3	-0.7	-0.5	0.7	1.3	-1.3	1.6	-237.8
Smear z_0	-1.6	-1.0	-0.5	-0.6	-0.1	0.1	-0.2	-0.5	0.0	0.6	0.9	2.9	8.8	-33.9
Fake Rate	-1.7	-0.9	-0.0	-0.0	0.2	0.2	0.1	-0.1	0.2	1.4	3.0	6.1	11.6	52.4
Total Syst	7.0	4.1	2.1	2.0	1.8	2.1	2.6	3.4	5.1	6.5	12.2	19.8	35.8	358.1
Stat Err	1.1	0.8	0.7	0.7	0.5	0.6	0.7	0.8	1.0	1.1	0.7	1.7	27.1	99.6

	η			
	0-0.6	0.6-1.2	1.2-1.8	1.8-2.5
Jet Systs	0.2	0.2	0.2	0.3
Plie Up	0.2	0.2	0.1	0.3
Track Multiplicity	0.4	0.4	0.4	0.6
Smear η	-1.3	-1.7	-1.9	-2.0
Smear ϕ	-1.9	-2.5	-2.6	-2.9
Shared Hits	1.2	1.3	2.1	2.2
Smear d_0	-0.5	-1.0	-1.0	-1.4
Smear z_0	-0.2	-0.7	-1.1	-0.7
Fake Rate	-0.4	-0.5	-0.1	0.1
Total Syst	2.7	3.5	4.2	4.5
Stat Err	0.4	0.4	0.6	1.0

TABLE A.5: A breakdown of the contribution of the systematic uncertainties for each p_T (top) and η (bottom) bin using the MV1c tagger at 50% efficiency for b-jets. Values show the percentage error for each point.

	p_T GeV													
	20-30	30-40	40-50	50-60	60-75	75-90	90-110	110-140	140-200	200-300	300-500	500-800	800-1200	1200-2000
Jet Systs	1.1	0.1	0.7	0.2	0.1	0.3	0.2	0.2	0.4	0.4	0.5	0.5	5.2	14.5
Plie Up	0.0	0.3	0.2	0.0	0.2	0.0	0.1	0.1	0.3	0.0	0.1	-0.2	0.3	-0.7
Track Multiplicity	0.5	0.4	0.3	0.3	0.3	0.2	0.2	0.2	0.5	0.2	0.4	0.1	-1.6	-2.1
Smear η	-3.8	-1.9	-0.7	-0.5	-0.5	-0.7	-0.8	-1.3	-1.2	0.8	1.3	3.6	7.1	-13.9
Smear ϕ	-4.6	-2.4	-1.4	-1.0	-0.7	-0.9	-1.3	-2.0	-2.4	-0.4	1.6	1.4	14.0	-108.7
Shared Hits	-0.9	-0.1	0.3	0.8	1.0	1.2	1.6	1.9	3.4	5.6	9.9	15.7	22.0	-217.2
Smear d_0	-2.0	-1.2	-0.3	-0.4	-0.2	-0.3	-0.4	-0.8	-0.6	0.4	0.6	-0.4	-0.2	-158.6
Smear z_0	-1.9	-0.5	-0.3	-0.3	0.0	-0.2	-0.3	-0.6	-0.6	0.4	0.3	2.9	2.0	-143.6
Fake Rate	-1.6	-0.8	0.1	0.1	0.3	0.1	0.0	-0.2	-0.2	1.4	2.5	5.7	6.4	36.1
Total Syst	6.9	3.5	1.8	1.5	1.4	1.8	2.3	3.2	4.5	5.9	10.4	17.4	28.4	326.3
Stat Err	1.0	0.7	0.6	0.6	0.5	0.5	0.6	0.7	0.9	1.0	0.6	1.4	20.0	67.1

	η			
	0-0.6	0.6-1.2	1.2-1.8	1.8-2.5
Jet Systs	0.2	0.1	0.2	0.3
Plie Up	0.2	0.1	0.1	0.2
Track Multiplicity	0.4	0.3	0.3	0.6
Smear η	-1.3	-1.3	-1.6	-1.8
Smear ϕ	-1.9	-2.2	-2.3	-2.5
Shared Hits	0.9	1.0	1.7	1.9
Smear d_0	-0.7	-0.8	-0.8	-1.2
Smear z_0	-0.3	-0.6	-1.1	-0.6
Fake Rate	-0.4	-0.4	-0.2	0.0
Total Syst	2.6	3.0	3.6	3.9
Stat Err	0.3	0.4	0.5	0.9

TABLE A.6: A breakdown of the contribution of the systematic uncertainties for each p_T (top) and η (bottom) bin using the MV1c tagger at 57% efficiency for b-jets. Values show the percentage error for each point.

	p_T GeV													
	20-30	30-40	40-50	50-60	60-75	75-90	90-110	110-140	140-200	200-300	300-500	500-800	800-1200	1200-2000
Jet Systs	1.0	0.2	0.5	0.1	0.2	0.3	0.1	0.2	0.5	0.5	0.6	0.6	4.5	15.2
Plie Up	-0.1	0.2	0.2	0.1	0.1	0.1	0.1	0.1	0.3	0.0	0.1	-0.3	0.9	3.9
Track Multiplicity	0.5	0.4	0.3	0.3	0.3	0.2	0.2	0.2	0.4	0.2	0.3	0.2	-0.7	0.8
Smear η	-3.5	-1.6	-0.7	-0.5	-0.6	-0.8	-0.8	-1.2	-1.5	0.4	1.3	3.8	5.5	-12.3
Smear ϕ	-4.3	-2.1	-1.4	-0.9	-0.7	-1.0	-1.2	-1.9	-2.6	-0.5	1.3	1.9	12.3	21.3
Shared Hits	-0.7	0.0	0.2	0.7	0.8	1.1	1.5	1.8	2.8	5.1	9.2	15.1	18.5	-13.5
Smear d_0	-1.7	-0.9	-0.4	-0.3	-0.3	-0.4	-0.5	-0.7	-1.0	-0.0	0.5	0.1	1.3	8.6
Smear z_0	-1.4	-0.5	-0.4	-0.2	-0.3	-0.2	-0.4	-0.5	-1.1	0.3	0.3	2.9	2.7	10.7
Fake Rate	-1.5	-0.7	-0.0	0.1	0.2	-0.0	-0.0	-0.2	-0.2	1.2	2.3	5.4	6.6	75.6
Total Syst	6.3	3.0	1.8	1.4	1.4	1.8	2.2	3.0	4.4	5.3	9.7	16.9	24.4	83.3
Stat Err	0.9	0.7	0.6	0.5	0.4	0.5	0.5	0.7	0.8	0.9	0.6	1.3	17.2	74.6

	η			
	0-0.6	0.6-1.2	1.2-1.8	1.8-2.5
Jet Systs	0.1	0.1	0.2	0.2
Plie Up	0.2	0.1	0.2	0.2
Track Multiplicity	0.3	0.3	0.3	0.5
Smear η	-1.3	-1.3	-1.6	-1.8
Smear ϕ	-1.9	-2.0	-2.3	-2.5
Shared Hits	0.7	1.0	1.5	1.8
Smear d_0	-0.7	-0.7	-1.0	-1.2
Smear z_0	-0.3	-0.5	-1.3	-0.9
Fake Rate	-0.5	-0.3	-0.2	-0.1
Total Syst	2.6	2.8	3.6	3.9
Stat Err	0.3	0.4	0.5	0.8

TABLE A.7: A breakdown of the contribution of the systematic uncertainties for each p_T (top) and η (bottom) bin using the MV1c tagger at 60% efficiency for b-jets. Values show the percentage error for each point.

	p_T GeV													
	20-30	30-40	40-50	50-60	60-75	75-90	90-110	110-140	140-200	200-300	300-500	500-800	800-1200	1200-2000
Jet Systs	0.8	0.2	0.4	0.1	0.1	0.2	0.1	0.1	0.4	0.4	0.3	0.6	4.5	14.6
Plie Up	0.0	0.1	0.1	0.1	0.1	0.0	0.1	0.1	0.3	0.1	0.1	-0.1	0.3	3.8
Track Multiplicity	0.4	0.3	0.2	0.2	0.2	0.1	0.1	0.1	0.4	0.2	0.3	0.2	0.6	1.3
Smear η	-2.8	-1.1	-0.8	-0.3	-0.3	-0.7	-0.8	-1.2	-1.5	0.3	0.5	2.3	4.4	-26.1
Smear ϕ	-3.6	-1.4	-1.2	-0.8	-0.5	-0.7	-1.0	-1.7	-2.5	0.1	0.7	1.0	3.6	7.8
Shared Hits	-0.7	-0.0	0.1	0.4	0.6	0.8	0.9	0.9	1.6	3.4	6.5	11.3	16.4	-14.3
Smear d_0	-1.8	-0.9	-0.5	-0.5	-0.3	-0.5	-0.7	-1.1	-1.4	0.0	-0.1	-0.7	-0.9	5.2
Smear z_0	-1.4	-0.7	-0.5	-0.6	-0.2	-0.4	-0.4	-1.0	-1.0	0.0	-0.1	1.1	-0.9	-1.8
Fake Rate	-1.3	-0.4	-0.1	0.0	0.1	-0.0	-0.1	-0.3	-0.3	1.0	1.8	3.8	5.2	13.0
Total Syst	5.4	2.2	1.7	1.3	0.9	1.4	1.8	2.7	3.8	3.6	6.8	12.2	18.7	37.1
Stat Err	0.8	0.5	0.5	0.4	0.4	0.4	0.4	0.5	0.7	0.7	0.4	0.9	9.9	53.2

	η			
	0-0.6	0.6-1.2	1.2-1.8	1.8-2.5
Jet Systs	0.1	0.1	0.2	0.2
Plie Up	0.2	0.1	0.1	0.2
Track Multiplicity	0.3	0.2	0.3	0.5
Smear η	-1.0	-1.0	-1.5	-1.3
Smear ϕ	-1.4	-1.5	-2.0	-1.9
Shared Hits	0.4	0.5	0.9	1.2
Smear d_0	-0.8	-0.8	-1.2	-1.0
Smear z_0	-0.3	-0.7	-1.3	-1.0
Fake Rate	-0.5	-0.3	-0.2	0.1
Total Syst	2.0	2.2	3.2	3.0
Stat Err	0.3	0.3	0.4	0.7

TABLE A.8: A breakdown of the contribution of the systematic uncertainties for each p_T (top) and η (bottom) bin using the MV1c tagger at 70% efficiency for b-jets. Values show the percentage error for each point.

	p_T GeV													
	20-30	30-40	40-50	50-60	60-75	75-90	90-110	110-140	140-200	200-300	300-500	500-800	800-1200	1200-2000
Jet Systs	0.6	0.3	0.5	0.2	0.1	0.1	0.1	0.1	0.2	0.2	0.1	0.3	3.5	14.5
Plie Up	0.1	0.0	0.1	0.1	0.1	-0.0	0.1	-0.0	0.2	0.0	0.1	-0.0	0.7	2.2
Track Multiplicity	0.2	0.1	0.1	0.1	0.1	0.1	0.1	0.0	0.3	0.1	0.2	-0.0	1.0	-0.1
Smear η	-1.7	-0.7	-0.4	-0.4	-0.2	-0.5	-0.4	-0.7	-1.4	0.2	0.1	1.1	0.9	-9.6
Smear ϕ	-2.2	-0.8	-0.7	-0.7	-0.3	-0.7	-0.6	-0.8	-1.8	0.1	0.3	0.5	1.6	15.7
Shared Hits	-0.5	-0.0	0.1	0.1	0.4	0.3	0.4	0.5	0.6	1.8	3.5	6.6	10.0	1.4
Smear d_0	-1.2	-0.8	-0.3	-0.6	-0.4	-0.5	-0.4	-0.6	-1.3	-0.0	-0.3	-0.8	-3.0	-0.1
Smear z_0	-0.9	-0.6	-0.5	-0.6	-0.2	-0.4	-0.6	-0.6	-1.0	-0.3	-0.5	0.0	-0.5	13.8
Fake Rate	-0.7	-0.3	-0.0	-0.1	0.1	-0.1	-0.1	-0.1	-0.4	0.5	1.0	2.4	3.9	4.0
Total Syst	3.3	1.5	1.1	1.2	0.8	1.1	1.1	1.5	2.9	1.9	3.8	7.1	11.9	27.6
Stat Err	0.6	0.4	0.4	0.4	0.3	0.3	0.3	0.4	0.5	0.5	0.3	0.6	5.4	30.9

	η			
	0-0.6	0.6-1.2	1.2-1.8	1.8-2.5
Jet Systs	0.1	0.1	0.1	0.2
Plie Up	0.1	0.1	0.1	0.1
Track Multiplicity	0.1	0.1	0.2	0.3
Smear η	-0.6	-0.7	-1.0	-0.6
Smear ϕ	-0.8	-1.0	-1.3	-0.9
Shared Hits	0.2	0.2	0.4	0.7
Smear d_0	-0.6	-0.6	-1.0	-0.7
Smear z_0	-0.2	-0.6	-1.3	-0.8
Fake Rate	-0.3	-0.2	-0.3	0.2
Total Syst	1.2	1.5	2.4	1.8
Stat Err	0.2	0.2	0.3	0.5

TABLE A.9: A breakdown of the contribution of the systematic uncertainties for each p_T (top) and η (bottom) bin using the MV1c tagger at 80% efficiency for b-jets. Values show the percentage error for each point.

	p_T GeV													
	20-30	30-40	40-50	50-60	60-75	75-90	90-110	110-140	140-200	200-300	300-500	500-800	800-1200	1200-2000
Jet Systs	0.5	0.3	0.2	0.2	0.1	0.1	0.2	0.2	0.2	0.2	0.1	0.1	3.6	16.2
Plie Up	0.0	-0.0	0.0	0.1	0.0	0.0	0.0	0.0	0.2	-0.0	0.1	-0.0	-0.1	1.8
Track Multiplicity	0.1	0.1	0.1	0.1	0.1	0.1	0.1	0.0	0.2	0.1	0.1	0.1	-0.4	-0.7
Smear η	-1.0	-0.2	-0.2	-0.2	-0.1	-0.4	-0.3	-0.6	-0.9	-0.1	-0.0	1.0	-0.2	-0.8
Smear ϕ	-1.4	-0.3	-0.6	-0.4	-0.2	-0.6	-0.5	-0.8	-1.4	-0.3	0.1	0.5	0.1	5.0
Shared Hits	-0.2	0.1	0.0	0.1	0.3	0.2	0.2	0.3	0.3	1.1	2.4	4.8	8.5	11.2
Smear d_0	-1.0	-0.5	-0.4	-0.5	-0.4	-0.5	-0.4	-0.7	-1.1	-0.4	-0.4	-0.8	-3.1	6.8
Smear z_0	-0.8	-0.4	-0.5	-0.6	-0.3	-0.5	-0.6	-0.6	-0.8	-0.6	-0.6	-0.1	0.3	-0.5
Fake Rate	-0.3	0.0	0.1	0.0	0.1	-0.0	-0.0	-0.2	-0.3	0.4	0.8	2.2	2.9	11.4
Total Syst	2.3	0.8	1.0	1.0	0.6	1.0	0.9	1.4	2.3	1.4	2.6	5.4	10.2	24.4
Stat Err	0.5	0.4	0.3	0.3	0.2	0.3	0.3	0.4	0.4	0.4	0.2	0.5	4.2	14.7

	η			
	0-0.6	0.6-1.2	1.2-1.8	1.8-2.5
Jet Systs	0.1	0.1	0.0	0.1
Plie Up	0.1	0.0	0.1	0.1
Track Multiplicity	0.1	0.1	0.1	0.2
Smear η	-0.4	-0.4	-0.7	-0.4
Smear ϕ	-0.5	-0.7	-0.9	-0.6
Shared Hits	0.1	0.1	0.3	0.4
Smear d_0	-0.5	-0.6	-0.9	-0.5
Smear z_0	-0.2	-0.5	-1.3	-1.0
Fake Rate	-0.1	-0.1	-0.2	0.3
Total Syst	0.9	1.2	2.0	1.5
Stat Err	0.2	0.2	0.3	0.4

TABLE A.10: A breakdown of the contribution of the systematic uncertainties for each p_T (top) and η (bottom) bin using the MV1c tagger at 85% efficiency for b-jets. Values show the percentage error for each point.

	p_T GeV													
	20-30	30-40	40-50	50-60	60-75	75-90	90-110	110-140	140-200	200-300	300-500	500-800	800-1200	1200-2000
Jet Systs	0.9	0.4	0.4	0.4	0.3	0.4	0.3	0.6	0.5	0.6	0.5	0.3	1.3	4.3
Plie Up	-0.1	-0.2	-0.4	-0.2	-0.2	-0.1	-0.2	-0.1	-0.5	-0.1	0.0	0.3	-0.1	-1.5
Track Multiplicity	-0.4	-0.4	-0.4	-0.4	-0.5	-0.4	-0.4	-0.2	-0.6	-0.3	-0.1	0.3	-0.1	-0.2
Smear η	2.3	1.2	0.8	0.6	0.9	1.3	1.7	1.7	2.2	-1.5	-1.1	-2.1	-2.0	11.8
Smear ϕ	3.0	1.8	1.5	1.0	1.0	2.0	2.3	2.8	3.4	-0.6	-1.3	-1.2	-3.2	10.1
Shared Hits	0.6	-0.2	-0.4	-0.7	-1.4	-1.7	-2.2	-2.3	-4.0	-7.1	-9.2	-8.1	-6.1	-1.8
Smear d_0	1.5	1.3	0.9	0.5	0.6	1.4	1.7	1.7	2.5	0.1	0.0	0.7	-0.8	1.3
Smear z_0	1.1	1.1	0.9	0.8	0.5	0.9	1.5	2.0	2.4	0.5	-0.4	-1.0	-0.1	0.8
Fake Rate	0.5	-0.2	-0.5	-0.6	-0.7	-0.6	-0.1	0.0	0.3	-2.2	-2.9	-3.7	-3.1	-0.2
Total Syst	4.4	2.8	2.3	1.9	2.3	3.5	4.3	4.8	6.7	7.7	9.8	9.3	7.9	16.4
Stat Err	0.7	0.8	0.8	0.8	0.8	0.9	1.0	1.2	1.3	1.4	0.6	0.8	4.3	24.1

	η			
	0-0.6	0.6-1.2	1.2-1.8	1.8-2.5
Jet Systs	0.2	0.2	0.2	0.2
Plie Up	-0.3	-0.2	-0.2	-0.3
Track Multiplicity	-0.5	-0.4	-0.3	-0.4
Smear η	1.6	1.4	1.6	1.1
Smear ϕ	2.4	2.5	2.1	1.4
Shared Hits	-0.8	-1.5	-2.2	-1.2
Smear d_0	1.6	1.4	1.1	1.3
Smear z_0	0.8	1.3	1.9	1.2
Fake Rate	0.4	-0.0	-0.6	-0.7
Total Syst	3.6	3.7	4.1	2.9
Stat Err	0.5	0.6	0.6	0.7

TABLE A.11: A breakdown of the contribution of the systematic uncertainties for each p_T (top) and η (bottom) bin using the JetFitterCharm tagger at loose% efficiency for b-jets. Values show the percentage error for each point.

	p_T GeV													
	20-30	30-40	40-50	50-60	60-75	75-90	90-110	110-140	140-200	200-300	300-500	500-800	800-1200	1200-2000
Jet Systs	0.5	1.4	2.9	2.1	0.3	1.2	1.0	0.5	0.9	1.7	0.6	1.2	10.1	15.3
Plie Up	-0.5	-0.5	-0.7	-0.3	-0.0	-0.4	0.1	0.3	-0.0	0.3	0.4	0.9	-0.0	-5.5
Track Multiplicity	-0.2	-0.1	-0.3	-0.4	-0.3	-0.4	-0.4	-0.1	-0.1	0.2	0.7	1.2	1.2	3.7
Smear η	-1.0	-1.9	-1.5	-0.2	0.8	0.1	0.7	-2.1	-2.3	-2.1	-1.1	-1.4	-10.9	43.9
Smear ϕ	-1.1	-1.6	-1.4	-1.4	0.4	1.3	0.3	-0.8	-4.1	-2.7	-1.5	0.5	-25.1	42.0
Shared Hits	-0.7	-1.4	-1.3	-0.6	-1.1	-1.7	-1.8	-2.8	-4.1	-4.3	-5.8	1.7	-5.8	-188.2
Smear d_0	0.1	-1.6	0.2	-0.3	1.3	2.7	1.5	1.3	-1.7	4.0	0.5	1.5	-25.8	-20.5
Smear z_0	-0.1	-1.0	0.7	0.3	1.1	1.5	2.9	0.8	0.3	0.3	-0.6	0.5	-11.8	-55.0
Fake Rate	-3.6	-4.0	-3.0	-2.7	-1.9	-2.4	-1.8	-2.8	-2.6	-2.2	-3.0	-1.1	-16.0	-2.1
Total Syst	4.0	5.4	5.0	3.8	3.0	4.7	4.3	4.9	7.0	7.4	6.9	3.5	44.1	207.0
Stat Err	2.2	1.9	1.9	1.9	1.6	1.9	2.0	2.4	2.9	3.2	1.5	2.4	12.0	81.6

	η			
	0-0.6	0.6-1.2	1.2-1.8	1.8-2.5
Jet Systs	0.2	0.1	0.2	0.3
Plie Up	-0.2	0.0	-0.1	-0.8
Track Multiplicity	-0.5	-0.1	0.3	-0.2
Smear η	-1.1	-1.3	-2.0	0.3
Smear ϕ	-0.7	-1.9	-1.8	0.2
Shared Hits	-1.0	-2.8	-3.6	-0.4
Smear d_0	1.0	0.4	-0.9	0.3
Smear z_0	0.6	1.1	-0.8	0.7
Fake Rate	-1.8	-2.5	-4.5	-3.4
Total Syst	2.8	4.6	6.5	3.7
Stat Err	1.1	1.3	1.5	1.9

TABLE A.12: A breakdown of the contribution of the systematic uncertainties for each p_T (top) and η (bottom) bin using the JetFitterCharm tagger at medium% efficiency for b-jets. Values show the percentage error for each point.

Appendix B

Nusiance Parameters

This appendix contains a list of the NP used in the combined fit.

Signal Specific			
Nusiance Parameter	Region Applied	Value	Count
Ratio to SM cross section	Signal	Float	1
Branching Ratio	Signal	3.3%	1
Scale Uncertainty $qqVH$	Signal	1%	1
Scale Uncertainty $ggZH$	Signal	50%	1
NLO EW Correction	Signal	Shape only	1
Inclusive Acceptance	Signal	1.5-3.4%	2
Scale	Signal	-1.9% - 4.1%	2
PDF	Signal	2.1% - 5.0%	2
QCD Scale	Signal	Shape only	2
PDF Sets $qqVH$	Signal	2.4%	1
PDF Sets $ggZH$	Signal	17%	1
Total	14 with Priors, 1 floating		

TABLE B.1: Signal specific NPs.

Z+jets Specific			
Nusiance Parameter	Region Applied	Value	Count
Zl normalisation	All	5%	1
Zl 3/2 jet ratio	3 jet	5%	1
Zcl normalisation	All	Float	1
Zcl 3/2 jet ratio	3 jet	26%	1
Zbb normalisation	All	Float	1
Zbb 3/2 jet ratio	3 jet	20%	1
Zbl/Zbb ratio	2 and 3 jet	12%	2
Zbc/Zbb ratio	All	12%	1
Zcc/Zbc ratio	All	12%	1
Z + jets $\Delta\Phi$ shape	$Z+b/c$, Zl, 2 and 3 jets	Shape only	4
Z + jets p_T^V shape	$Z+b/c$, Zl in all regions	Shape only	2
Z + jets $m_b b$ shape	$Z+b/c$, Zl in all regions	Shape only	2
Total	16 with Priors, 2 floating		

TABLE B.2: Z+jets Specific NPs.

W+jets Specific			
Nusiance Parameter	Region Applied	Value	Count
Wl normalisation	All	10%	1
Wl 3/2 jet ratio	3 jet	10%	1
Wcl normalisation	All	Float	1
Wcl 3/2 jet ratio	3 jet	10%	1
Wbb normalisation	All	Float	1
Wbb 3/2 jet ratio	3 jet	10%	1
Wbl/Wbb ratio	$p_T^V = [0-90], [90-120], [120+]$	35%	3
Wbc/Wbb ratio	All	12%	1
Wcc/Wbc ratio	All	12%	1
W + jets $\Delta\Phi$ shape	$W+bb$, $W+cl$, Wl, 2 and 3 jets	Shape only	6
W + jets p_T^V shape	Wbb/cc, $p_T^V = [0-90], [90-120], [120+]$	Shape only	3
W + jets p_T^V shape	$Wbc/bl, Wcl, Wl$ in all regions	Shape only	3
W + jets $m_b b$ shape	$W+bb$ 2 and 3 jet	Shape only	2
Total	23 with Priors, 2 floating		

TABLE B.3: W+jets Specific NPs.

$t\bar{t}$ Specific			
Nusiance Parameter	Region Applied	Value	Count
$t\bar{t}$ normalisation	0,1 and 2 lepton	Float	3
high/low p_T^V	$p_T^V > 120$ GeV	7.5%	1
3/2-jet ratio	3-jet in 2 and 0+1 lepton	20%	2
Top p_T	All	Shape only	1
$m_b b$ shape	All	Shape only	1
E_T^{miss} shape	All 1 lepton	1	
Total	6 with Priors, 3 floating		

TABLE B.4: $t\bar{t}$ Specific NPs.

Single t Specific			
Nusiance Parameter	Region Applied	Value	Count
s-channel			
Cross section	All	4%	1
AcerMC vs Pythis+Powheg	All	13 - 40%	1
Shower uncertainty	All	4 - 8%	1
t-channel			
Cross section	All	4%	1
aMCatNLO vs AcerMC	All	-18 - 52%	1
Wt-channel			
Cross section	All	7%	1
AcerMC vs Pythis+Powheg	All	-15 - 1%	1
Shower uncertainty	All	-3 - 5 %	1
Total	8 with Priors, 0 floating		

TABLE B.5: Single top specific NPs.

Diboson Specific			
Nusiance Parameter	Region Applied	Value	Count
Scale	All	Shape only	2
PDF	All	2 - 4%	1
$m_b b$ shape	All	Shape only	3
Total	6 with Priors, 0 floating		

TABLE B.6: Diboson Specific NPs.

Single t Specific			
Nusiance Parameter	Region Applied	Value	Count
0-lepton			
Normalisation	2 and 3-jet 1/2 tag $>$ / $<$ 120 GeV	100%	6
1-lepton			
Normalisation	2-jet 1/2L/2M/2T and 3-jet 1/2 tag	11 - 60 %	12
Template iso_track cut	2/3 jet, 1/2 tag	Shape only	10
Reweight	2-jet 2-tag	Shape only	2
2-lepton			
Normalisation	top $e-\mu$ decorrelated	100%	1
Total	31 with Priors, 0 floating		

TABLE B.7: Multijet specific NPs.

Experimental	
Nusiance Parameter	Count
Luminosity	
Total integrated luminosity	1
Error on profile	1
Leptons	
Electron, trigger, reconstuction and ID efficiencies	1
Electron energy scale	1
Electron energy resolution	1
Muon trigger, reconstruction and ID efficiencies	1
Muon energy resolution from inner detector	1
Muon energy resolution from muon system	1
Isolation scale factors	1
Lepton veto efficiency (0-lep)	1
E_T^{miss} Trigger	
W vs Z efficieny curve	1
Stat uncertainty of efficiency fit curve	1
Jet Energy Scale	
Eigenvector decomposition of in-situ calibration	6
η inter-calibration model	1
η inter-calibration model stat	1
Calibration non closure	1
Pileup	3
NPV correction	1
b-jet energy scale	1
b-jet scale for μ and ν energy	1
Light quark vs gluon fraction	4
Light quark vs gluon response	4
Jet Energy Resolution	
All jets	1
b-jet specific	1
Jet Quality	
JVF	1
E_T^{miss}	
Resolution of soft componant	1
Sacle of soft componant	1
Flavour Tagging	
b-jet	10
c-jet	15
light-jet	10
ΔR(cc) bias from truth tagging	1
Generator dependent heavy flavour tagging efficiency	4
Total	80 with Priors, 0 floating

TABLE B.8: Experimental NPs.

Bibliography

[1] D. J. Griffiths, *Introduction to Elementary Particles*. TextBook Physics. Wiley, New York, NY, 1987.

[2] F. Halzen and A. D. Martin, *Quarks and leptons: an introductory course in modern particle physics*. Wiley, New York, NY, 1984.

[3] Y. Fukuda et al., *Measurements of the Solar Neutrino Flux from Super-Kamiokande's First 300 Days*, Phys. Rev. Lett. **81** (1998) 1158–1162. http://link.aps.org/doi/10.1103/PhysRevLett.81.1158.

[4] Particle Data Group Collaboration, *Review of Particle Physics*, Phys. Rev. D **86** (2012) 010001. http://link.aps.org/doi/10.1103/PhysRevD.86.010001.

[5] B. Lee, C. Quigg, and H. Thacker, *Strength of Weak Interactions at Very High Energies and the Higgs Boson Mass*, Phys. Rev. Lett. **38** (1977) 883–885. http://link.aps.org/doi/10.1103/PhysRevLett.38.883.

[6] S. L. Glashow, *Partial-symmetries of weak interactions*, Nuclear Physics **22** no. 4, (1961) 579 – 588. http://www.sciencedirect.com/science/article/pii/0029558261904692.

[7] A. Salam and J. Ward, *Electromagnetic and weak interactions*, Physics Letters **13** no. 2, (1964) 168 – 171. http://www.sciencedirect.com/science/article/pii/0031916364907115.

[8] G. Arnison et al., *Experimental observation of isolated large transverse energy electrons with associated missing energy at $s = 540$ GeV*, Physics Letters B **122** no. 1, (1983) 103 – 116. http://www.sciencedirect.com/science/article/pii/0370269383911772.

[9] J. Goldstone, *Field theories with Superconductor solutions*, Il Nuovo Cimento **19** no. 1, (1961) 154–164. http://dx.doi.org/10.1007/BF02812722.

[10] F. Englert and R. Brout, *Broken Symmetry and the Mass of Gauge Vector Mesons*, Phys. Rev. Lett. **13** (1964) 321–323. http://link.aps.org/doi/10.1103/PhysRevLett.13.321.

[11] P. W. Higgs, *Spontaneous Symmetry Breakdown without Massless Bosons*, Phys. Rev. **145** (1966) 1156–1163. http://link.aps.org/doi/10.1103/PhysRev.145.1156.

[12] P. Higgs, *Broken symmetries, massless particles and gauge fields*, Physics Letters **12** no. 2, (1964) 132 – 133. http://www.sciencedirect.com/science/article/pii/0031916364911369.

[13] G. S. Guralnik, C. R. Hagen, and T. W. B. Kibble, *Global Conservation Laws and Massless Particles*, Phys. Rev. Lett. **13** (1964) 585–587. http://link.aps.org/doi/10.1103/PhysRevLett.13.585.

[14] J. Price and J. Vossebeld, *Search for a Higgs boson in the $H \to ZZ$ and $ZH \to ll + invisible$ channels with the ATLAS detector*. PhD thesis, Liverpool U., Apr, 2013. Presented 29 Jun 2013.

[15] C. Maxwell, "The standard model." Notes from RAL summer school 2012, 2011.

[16] ATLAS, CMS Collaboration, *Combined Measurement of the Higgs Boson Mass in pp Collisions at $\sqrt{s} = 7$ and 8 TeV with the ATLAS and CMS Experiments*, Phys. Rev. Lett. **114** (2015) 191803, arXiv:1503.07589 [hep-ex].

[17] B. A. W. D. Kohler and J. A. Becker, *Experimental search for a low-mass scalar boson*, PRL **33** (1974) 1628–1631.

[18] R. Barbieri and T. E. O. Ericson, *Evidence against the existence of a low mass scalar boson from neutron-nucleus scattering*, Phys. Lett. B **57** (1975) 270–272.

[19] Electro weak working group. http:$\/\/$lepewwg.web.cern.ch$\/$LEPEWWG$\/$plots$\/$summer2005$\/$.

[20] CDF and D0, *Combined CDF and D0 Upper Limits on Standard Model Higgs Boson Production with up to 8.6 fb-1 of Data*, FERMILAB-CONF-11-354-E (2011). Comments: Sumitted to the EPS 2011 Conference.

[21] Tevatron New Physics Higgs Working Group, CDF Collaboration, D0 Collaboration Collaboration, *Updated Combination of CDF and D0 Searches for Standard Model Higgs Boson Production with up to 10.0 fb^{-1} of Data*, arXiv:1207.0449 [hep-ex].

[22] CERN. https://twiki.cern.ch/twiki/bin/view/LHCPhysics/LHCHXSWG.

[23] ATLAS Collaboration, G. Aad et al., *Observation of a new particle in the search for the Standard Model Higgs boson with the ATLAS detector at the LHC*, Phys.Lett. **B716** (2012) 1–29, arXiv:1207.7214 [hep-ex].

[24] CMS Collaboration Collaboration, S. Chatrchyan et al., *Observation of a new boson at a mass of 125 GeV with the CMS experiment at the LHC*, Phys.Lett. **B716** (2012) 30–61, arXiv:1207.7235 [hep-ex].

[25] ATLAS Collaboration, *Measurements of the properties of the Higgs-like boson in the two photon decay channel with the ATLAS detector using 25* fb^{-1} *of proton-proton collision data*, ATLAS-CONF-2013-012 (2013).

[26] ATLAS Collaboration, *Measurements of the properties of the Higgs-like boson in the four lepton decay channel with the ATLAS detector using 25 fb1 of proton-proton collision data*, ATLAS-CONF-2013-013 (2013).

[27] ATLAS Collaboration, *Measurements of the properties of the Higgs-like boson in the* $WW^{(*)} \to \ell\nu\ell\nu$ *decay channel with the ATLAS detector using 25* fb^{-1} *of proton-proton collision data*, ATLAS-CONF-2013-030 (2013).

[28] L. Evans and P. Bryant, *The LHC Machine*, PoS EPS-HEP2009 (2009) 004.

[29] Lefevre, C., *The CERN Accelerator Complex*, https://cds.cern.ch/record/1260465 (2008).

[30] ATLAS public images http://cds.cern.ch/record/40525.

[31] A. Martin, W. Stirling, R. Thorne, and G. Watt, *Parton distributions for the LHC*, Eur. Phys. J. **C63** (2009) 189–285. http://arxiv.org/abs/0901.0002.

[32] Bruning, Oliver Sim and Collier, Paul and Lebrun, P and Myers, Stephen and Ostojic, Ranko and Poole, John and Proudlock, Paul, *LHC Design Report*. CERN, Geneva, 2004.

[33] ATLAS Collaboration, *The ATLAS Experiment at the CERN Large Hadron Collider*, J. Instrum. **3** (2008) S08003. 437 p.

[34] Goodson, J. http://www.jetgoodson.com/images/thesisImages/magnetSystems.png.

[35] F. Meloni, A. Milov, S. Pagan-Griso, K. Prokofiev and A. Wildauer, *Vertexing Performance Data vs MC comparison for LPCC*, ATL-COM-PHYS-2011-1312 (2011).

[36] ATLAS Collaboration, *ATLAS detector and physics performance: Technical Design Report, 1.* Technical Design Report ATLAS. CERN, Geneva, 1999. Electronic version not available.

[37] ATLAS Collaboration, *ATLAS level-1 trigger: Technical Design Report.* Technical Design Report ATLAS. CERN, Geneva, 1998.

[38] ATLAS Collaboration, *The ATLAS Simulation Infrastructure*, The European Physical Journal C **70** no. 3, (2010) 823–874. http://dx.doi.org/10.1140/epjc/s10052-010-1429-9.

[39] GEANT4 Collaboration, S. Agostinelii et al., *GEANT4: A simulation toolkit*, Nucl. Instrum. Meth. **A506** (2003) 250–303.

[40] C. ATLAS, M. Beckingham, M. Duehrssen, E. Schmidt, M. Shapiro, M. Venturi, J. Virzi, I. Vivarelli, M. Werner, S. Yamamoto, and T. Yamanaka, *The simulation principle and performance of the ATLAS fast calorimeter simulation FastCaloSim*, ATL-PHYS-PUB-2010-013 (2010).

[41] *Electron efficiency measurements with the ATLAS detector using the 2012 LHC proton-proton collision data*, ATLAS-CONF-2014-032 (2014).

[42] ATLAS Collaboration, G. Aad et al., *Measurement of the muon reconstruction performance of the ATLAS detector using 2011 and 2012 LHC proton-proton collision data*, arXiv:1407.3935 [hep-ex].

[43] Sieber, G. and others, *Determination of the proton structure and the strong coupling from inclusive jet cross sections at the LHC*, CERN-THESIS-2013-034, IEKP-KA/2013-10 (2013).

[44] W. Lampl, S. Laplace, D. Lelas, P. Loch, H. Ma, S. Menke, S. Rajagopalan, D. Rousseau, S. Snyder, and G. Unal, *Calorimeter Clustering Algorithms: Description and Performance*, ATL-LARG-PUB-2008-002. ATL-COM-LARG-2008-003 (2008).

[45] M. Cacciari, G. P. Salam, and G. Soyez, *The Anti-k(t) jet clustering algorithm*, JHEP **0804** (2008) 063, arXiv:0802.1189 [hep-ph].

[46] ATLAS Collaboration, G. Aad et al., *Jet energy measurement with the ATLAS detector in proton-proton collisions at* $\sqrt{s} = 7$ *TeV*, Eur.Phys.J. **C73** (2013) 2304, arXiv:1112.6426 [hep-ex].

[47] ATLAS Collaboration, G. Aad et al., *Jet energy measurement and its systematic uncertainty in proton-proton collisions at* $\sqrt{s} = 7$ *TeV with the ATLAS detector*, arXiv:1406.0076 [hep-ex].

[48] M. Cacciari and G. P. Salam, *Pileup subtraction using jet areas*, Phys.Lett. **B659** (2008) 119–126, arXiv:0707.1378 [hep-ph].

[49] ATLAS Collaboration, *b-Jet Tagging Efficiency Calibration using the System8 Method*, ATLAS-CONF-2011-143 (2011).

[50] ATLAS Collaboration, *Calibration of b-tagging using dileptonic top pair events in a combinatorial likelihood approach with the ATLAS experiment*, ATLAS-CONF-2014-004 (2014).

[51] ATLAS Collaboration, *b-jet tagging calibration on c-jets containing D^{*+} mesons*, ATLAS-CONF-2012-039 (2012).

[52] ATLAS Collaboration, *Measurement of the b-tag Efficiency in a Sample of Jets Containing Muons with 5 fb1 of Data from the ATLAS Detector*, ATLAS-CONF-2012-043 (2012).

[53] ATLAS Collaboration, *Performance of Missing Transverse Momentum Reconstruction in ATLAS studied in Proton-Proton Collisions recorded in 2012 at 8 TeV*, ATLAS-CONF-2013-082 (2013).

[54] T. Sjostrand, S. Mrenna and P. Z. Skands, *PYTHIA 6.4 Physics and Manual*, JHEP **0605** (2006) 026.

[55] *ATLAS tunes of PYTHIA 6 and Pythia 8 for MC11*, ATL-PHYS-PUB-2011-009 (2011).

[56] *New ATLAS event generator tunes to 2010 data*, ATL-PHYS-PUB-2011-008 (2011).

[57] ATLAS Collaboration, *Performance of the ATLAS Secondary Vertex b-tagging Algorithm in 7 TeV Collision Data*, ATLAS-CONF-2010-042 (2010).

[58] ATLAS Collaboration, *Commissioning of the ATLAS high-performance b-tagging Algorithms in 7 TeV Collision Data*, ATLAS-CONF-2011-102 (2011).

[59] C. W. G. Piacquadio, *A new inclusive secondary vertex algorithm for b-jet tagging in ATLAS*, J.Phys.Conf.Ser. (2008).

[60] F. Filthaut and C. Weiser, *Performance of b-Jet Identification in the ATLAS Experiment*, ATL-COM-PHYS-2012-824 (2012).

[61] *Charged-particle multiplicities in ppinteractions measured with the ATLAS detector at the LHC*, New Journal of Physics **13** no. 5, (2011) 053033. http://stacks.iop.org/1367-2630/13/i=5/a=053033.

[62] ATLAS Collaboration, *Jet energy scale and its systematic uncertainty in proton-proton collisions at 7 TeV in ATLAS 2010 data*, ATLAS-CONF-2011-089 (2011).

[63] OPAL Collaboration, G. Abbiendi et al. Eur.Phys.J. **C29** (2003) 463.

[64] SLD Collaboration, *Measurement of the b-quark fragmentation function in Z0 decays*, Phys. Rev. D **65** (2002) 092006. http://link.aps.org/doi/10.1103/PhysRevD.65.092006.

[65] ALEPH Collaboration, *Study of the fragmentation of b quarks into B mesons at the Z peak*, Phys.Lett. **B512** (2001) 30–48, arXiv:hep-ex/0106051 [hep-ex].

[66] DELPHI Collaboration, *A study of the b-quark fragmentation function with the DELPHI detector at LEP I and an averaged distribution obtained at the Z Pole*, Eur. Phys. J. **C29** (2011). http://arxiv.org/abs/1102.4748.

[67] ATLAS Collaboration, *Calibration of b-tagging using dileptonic top pair events in a combinatorial likelihood approach with the ATLAS experiment*, ATLAS-CONF-2014-004 (2014).

[68] ATLAS Collaboration, *A search for resonant Higgs-pair production in the $b\bar{b}b\bar{b}$ final state in pp collisions at $\sqrt{s} = 8$ TeV*, ATLAS-CONF-2014-005 (2014).

[69] ATLAS Collaboration, G. Aad et al., *Measurement of the Higgs boson mass from the $H \to \gamma\gamma$ and $H \to ZZ^* \to 4\ell$ channels with the ATLAS detector using 25 fb^{-1} of pp collision data*, Phys.Rev. **D90** (2014) 052004, arXiv:1406.3827 [hep-ex].

[70] LHC Higgs Cross Section Working Group Collaboration, S. Dittmaier et al., *Handbook of LHC Higgs Cross Sections: 1. Inclusive Observables*, arXiv:1101.0593 [hep-ph].

[71] ATLAS Collaboration, *Search for the Standard Model Higgs boson in associated production with a vector boson and decaying to bottom quarks with the ATLAS detector*, ATL-COM-PHYS-2013-465 (2013).

[72] ATLAS Collaboration, *Search for the Standard Model Higgs boson in produced in association with a vector boson and decaying to bottom quarks with the ATLAS detector*, ATLAS-CONF-2012-161 (2012).

[73] ATLAS Collaboration, *Search for the Standard Model Higgs boson produced in association with a vector boson and decaying to a b-quark pair with the {ATLAS} detector*, Physics Letters B **718** no. 2, (2012) 369 – 390. http://www.sciencedirect.com/science/article/pii/S0370269312011276.

[74] ATLAS Collaboration, G. Aad et al., *Search for the $b\bar{b}$ decay of the Standard Model Higgs boson in associated $(W/Z)H$ production with the ATLAS detector*, arXiv:1409.6212 [hep-ex].

[75] C. Englert, M. McCullough, and M. Spannowsky, *Gluon-initiated associated production boosts Higgs physics*, Phys. Rev. D **89** (2014) 013013. http://link.aps.org/doi/10.1103/PhysRevD.89.013013.

[76] T. Sjostrand, S. Mrenna, and P. Z. Skands, *A Brief Introduction to PYTHIA 8.1*, Comput.Phys.Commun. **178** (2008) 852–867, arXiv:0710.3820 [hep-ph].

[77] J. Pumplin, D. Stump, J. Huston, H. Lai, P. M. Nadolsky, et al., *New generation of parton distributions with uncertainties from global QCD analysis*, JHEP **0207** (2002) 012, arXiv:hep-ph/0201195 [hep-ph].

[78] *ATLAS tunes of PYTHIA 6 and Pythia 8 for MC11*, ATL-PHYS-PUB-2011-009 (2011).

[79] *New ATLAS event generator tunes to 2010 data*, ATL-PHYS-PUB-2011-008 (2011).

[80] P. Nason, *A New method for combining NLO QCD with shower Monte Carlo algorithms*, JHEP **0411** (2004) 040, arXiv:hep-ph/0409146 [hep-ph].

[81] S. Frixione, P. Nason, and C. Oleari, *Matching NLO QCD computations with Parton Shower simulations: the POWHEG method*, JHEP **0711** (2007) 070, arXiv:0709.2092 [hep-ph].

[82] S. Alioli, P. Nason, C. Oleari, and E. Re, *A general framework for implementing NLO calculations in shower Monte Carlo programs: the POWHEG BOX*, JHEP **1006** (2010) 043, arXiv:1002.2581 [hep-ph].

[83] H.-L. Lai, M. Guzzi, J. Huston, Z. Li, P. M. Nadolsky, et al., *New parton distributions for collider physics*, Phys.Rev. **D82** (2010) 074024, arXiv:1007.2241 [hep-ph].

[84] ATLAS Collaboration, *Search for the Production of a Standard Model Higgs boson produced in association with a Vector boson and decaying to a pair of b-quarks*, ATL-COM-PHYS-2014-051 (2014).

[85] A. Hoecker, P. Speckmayer, J. Stelzer, J. Therhaag, E. von Toerne, and H. Voss, *TMVA: Toolkit for Multivariate Data Analysis*, PoS **ACAT** (2007) 040, arXiv:physics/0703039.

[86] ATLAS Collaboration, D. Damazio, T. Kono, F. Monticelli, and G. Pasztor, *Performance of the ATLAS Electron and Photon Triggers in p-p Collisions at* $\sqrt{s} = 8$ *TeV in 2012*, ATL-COM-DAQ-2013-121 (2013).

[87] ATLAS Collaboration, Aad, Georges and others, *Performance of the ATLAS muon trigger in pp collisions at* $\sqrt{s} = 8$ *TeV*, arXiv:1408.3179 [hep-ex].

[88] ATLAS Collaboration, J.-B. Blanchard, J.-B. de Vivie, and P. Mastrandrea, *In situ scales and smearings from Z and* J/Ψ *events*, ATL-COM-PHYS-2013-1653 (2013).

[89] *Preliminary results on the muon reconstruction efficiency, momentum resolution, and momentum scale in ATLAS 2012 pp collision data*, ATLAS-CONF-2013-088 (2013).

[90] ATLAS Collaboration, *Jet energy scale and its systematic uncertainty in proton-proton collisions at sqrt(s)=7 TeV with ATLAS 2011 data*, ATLAS-CONF-2013-004 (2013).

[91] ATLAS Collaboration, G. Aad et al., *Jet energy measurement with the ATLAS detector in proton-proton collisions at* $\sqrt{s} = 7$ *TeV*, Eur.Phys.J. **C73** (2013) 2304, arXiv:1112.6426 [hep-ex].

[92] ATLAS Collaboration, *ATLAS Calorimeter Response to Single Isolated Hadrons and Estimation of the Calorimeter Jet Scale Uncertainty*, ATLAS-CONF-2011-028 (2011).

[93] ATLAS Collaboration, G. Aad et al., *Jet energy resolution in proton-proton collisions at* $\sqrt{s} = 7$ *TeV recorded in 2010 with the ATLAS detector*, Eur.Phys.J. **C73** (2013) 2306, arXiv:1210.6210 [hep-ex].

[94] *Invariant Mass Studies for the* $H \to b\bar{b}$ *Measurements for HCP*, ATL-COM-2012-1451 (2012).

[95] *Performance of Missing Transverse Momentum Reconstruction in ATLAS studied in Proton-Proton Collisions recorded in 2012 at 8 TeV*, ATLAS-CONF-2013-082 (2013).

[96] Berta, P. and Filthaut, F. and Dao, V. and Le Menedeu, E. and Parodi, F., and Piacquadio, G. and Scanlon, T. and Ughetto, M., *Continuous b-tagging for the ATLAS Experiment*, ATL-COM-2014-035 (2014).

[97] ATLAS Collaboration, G. Aad et al., *Measurements of normalized differential cross sections for* $t\bar{t}$ *production in pp collisions at* $\sqrt{s} = 7$*TeV using the ATLAS detector*, Phys.Rev. **D90** no. 7, (2014) 072004, arXiv:1407.0371 [hep-ex].

[98] A. Djouadi, J. Kalinowski, and M. Spira, *HDECAY: A Program for Higgs boson decays in the standard model and its supersymmetric extension*, Comput.Phys.Commun. **108** (1998) 56–74, arXiv:hep-ph/9704448 [hep-ph].

[99] LHC Higgs Cross Section Working Group Collaboration, S. Dittmaier et al., *Handbook of LHC Higgs Cross Sections: 1. Inclusive Observables*, arXiv:1101.0593 [hep-ph].

[100] I. W. Stewart and F. J. Tackmann, *Theory uncertainties for Higgs mass and other searches using jet bins*, Phys. Rev. D **85** (2012) 034011. http://link.aps.org/doi/10.1103/PhysRevD.85.034011.

[101] A. Denner, S. Dittmaier, S. Kallweit, and A. Muck, *EW corrections to Higgs strahlung at the Tevatron and the LHC with HAWK*, PoS **EPS-HEP2011** (2011) 235, arXiv:1112.5258 [hep-ph].

[102] LHC Higgs Cross Section Working Group Collaboration, *Handbook of LHC Higgs Cross Sections: 2. Differential Distributions*, arXiv:1201.3084. CERN-2012-002 (2012). Comments: 275 pages, 136 figures, to be submitted to CERN Report. Working Group web page: https://twiki.cern.ch/twiki/bin/view/LHCPhysics/CrossSections.

[103] Yang, L L and Li, C S and Liu, J J and Jin, L G, *Production of Scalar Higgs Bosons Associated with Z^0 Boson at the CERN LHC in the MSSM*, hep-ph/0312179 (2003).

[104] I. W. Stewart and F. J. Tackmann, *Theory uncertainties for Higgs mass and other searches using jet bins*, Phys. Rev. D **85** (2012) 034011. http://link.aps.org/doi/10.1103/PhysRevD.85.034011.

[105] M. Botje, J. Butterworth, A. Cooper-Sarkar, A. de Roeck, J. Feltesse, et al., *The PDF4LHC Working Group Interim Recommendations*, arXiv:1101.0538 [hep-ph].

[106] A. L. Read, *Presentation of search results: the CL s technique*, Journal of Physics G: Nuclear and Particle Physics **28** no. 10, (2002) 2693. http://stacks.iop.org/0954-3899/28/i=10/a=313.

[107] G. Cowan, K. Cranmer, E. Gross, and O. Vitells, *Asymptotic formulae for likelihood-based tests of new physics*, Eur.Phys.J. **C71** (2011) 1554, arXiv:1007.1727 [physics.data-an].

[108] N. Chanon, *Statistical Tools in Collider Experiments, Multivariate Analysis in High Energy Physics: Lecture 5*,. https://people.phys.ethz.ch/~pheno/Lectures2012_StatisticalTools/slide%s/.

[109] L. Moneta, K. Belasco, K. S. Cranmer, S. Kreiss, A. Lazzaro, et al., *The RooStats Project*, PoS **ACAT2010** (2010) 057, arXiv:1009.1003 [physics.data-an].

[110] W. Verkerke and D. P. Kirkby, *The RooFit toolkit for data modeling*, eConf **C0303241** (2003) MOLT007, arXiv:physics/0306116 [physics].